

DISS. ETH No. 24440

# LEVITATED OPTOMECHANICS AT THE PHOTON RECOIL LIMIT

A thesis submitted to attain the degree of  
DOCTOR OF SCIENCES OF ETH ZURICH  
(Dr. sc. ETH Zurich)

presented by

VIJAY JAIN

A.B., Harvard University

M.A., University of Rochester

born on 10.11.1989

citizen of the United States of America

accepted on the recommendation of  
Prof. Dr. Lukas Novotny, examiner  
Prof. Dr. Markus Aspelmeyer, co-examiner  
Prof. Dr. Tilmann Esslinger, co-examiner

2017

The work described in this thesis is part of the research program of the Quantum Mesoscopic Systems Program which is financially supported by the European Research Council and was partially supported by a Graduate Research Fellowship of the US National Science Foundation.

This work was carried out at the

*Photonics Laboratory*

*D-ITET, ETH Zürich*

*Hönggerberggring 64, CH-8093 Zürich*

where a limited number of copies of this dissertation are available.

*Gring abe u seckle!*  
– Anita Weyermann

Dedicated to Shri Santosh Chand Kocheta.

---

## Abstract

Optomechanics explores the coupling between light and the mechanical motion of nanoscopic matter. Optical levitation offers a promising avenue in the investigation of macroscopic quantum behavior by using glass nanoparticles that are physically detached from the environment.

Our goal in this thesis is to bring a levitated nanoparticle to the quantum ground state of its center-of-mass motion using phase-sensitive feedback that is conditioned on high precision interferometric measurements of the particle's position. We cool the harmonic motion of the nanoparticle from ambient to microkelvin temperatures and measure its reheating rate under the influence of the radiation field. The limit reached corresponds to that of photon recoil heating, which will set bounds to the coherence times of future quantum states and protocols in our system. We quantitatively characterize the role of laser intensity noise for demanding applications in ultrasensitive force detection and find that the system is in the regime of strong measurement backaction. Finally, protocols to interrogate the classical to quantum transition are proposed.

---

## Zusammenfassung

Die Optomechanik befasst sich mit der Kopplung zwischen Licht und der mechanischen Bewegung von nanoskopischer Materie. Im Speziellen sind durch ein Laserfeld am Schweben gehaltene Nanopartikel, welche sehr gut von ihrer Umgebung isoliert sind, vielversprechend um in die Welt der makroskopischen Quantenmechanik einzutreten und diese zu erforschen.

Ziel dieser Arbeit ist es ein schwebendes Nanopartikel in den quantenmechanischen Grundzustand seiner Schwerpunktsbewegung zu kühlen. Dazu nutzen wir eine phasensensitive Regelschleife, welche auf der hoch präzisen interferometrischen Messung der Partikelposition basiert. Wir kühlen die harmonische Oszillation des Nanopartikels von Raumtemperatur bis auf wenige mikro-Kelvin. Zusätzlich messen wir die Heizrate des optische Strahlungsfelds, das das Partikel am Schweben hält. Die kleinste gemessene Temperatur wird durch Rückstossheizen von Photonen bestimmt, welches die Kohärenzzeit zukünftiger Quantenzustandes unseres Systems limitieren wird. Zusätzlich charakterisieren wir die Rolle von Intensitätsrauschen des Laserlichts im Zusammenhang mit ultra-sensitiven Kräftermessungen und zeigen, dass sich unser System im Regime der starken Rückwirkung durch Messung befindet. Schliesslich schlagen wir Protokolle zum Testen des Übergangs von klassischen Mechanik zur Quantenbereich vor.

---

## Acknowledgments

My time in the Photonics Laboratory, the research I have conducted, and the writing of this thesis were incredibly rewarding experiences during which I had the opportunity to grow as a scientist, learn to be independent, and ask critical questions. There are many people without whom this journey would not have been possible and I would like to take a few lines to acknowledge their contributions.

First, and foremost, I must thank my advisor, Lukas Novotny. Like the skilled sailor that you are, you have captained this ship through many stormy seas and, inconceivably, onward to glittering waters. I will be forever indebted to you for your guidance, never-ending insistence on being systematic, clarity, and precision. Thank you for giving me the chance to take risks in the lab, patiently letting me fail over and over again, asking challenging questions, and bringing me along on this exciting journey!

Thank you to my co-examiners Profs. Esslinger and Aspelmeyer, for agreeing to be part of my thesis committee and coming together and reviewing with great haste!

My fellow particle trapping colleagues have each had an immense influence on this work. Thank you to Jan, for always being available for countless hours of scientific discussion, being a fine mentor, and a great friend; Martin and Rene, for always pushing me to question my assumptions – an invaluable asset along the entirety of this scientific endeavor; Felix, for your curiosity and many questions, patience while I wrote, and enthusiasm, which have built

---

a healthy and collaborative atmosphere; Erik, Rozenn, Loic, Dominic, Brad, Pau, Francesco, Irene, and Nadine for being great teammates and tremendous resources for technical know-how and hackery; Christoph Dellago for incredibly valuable discussions and insights on statistical mechanics; and, Romain for being a constant, positive source of encouragement and always making me feel welcome at ICFO.

The Nano-Optics Group and (now) Photonics Laboratory were formative environments; I have learned a lot about science and life from my colleagues. Thanks to Palash and Vasudha who always served as great fonts of advice and guidance over the years; without your encouragement, I would not have joined this group; Sarah, for being a priceless resource for clarity, scientific discussion, and a great friend; Nikolaus for being my in-house guru, teaching me everything I know about solid-state physics and bicycles; Markus and Sebastian for keeping the endorphins high by continuing the nano-running experiment; Barbara, for being a great source of support right from the very start, making sure no resource was out of reach; and, in general, the whole group, for being top-notch colleagues with whom I moved across an ocean, built a lab from scratch, learned all sorts of valuable insights and techniques in science, and for always lending an ear to all my scientific curiosities.

Among my ETH colleagues, thanks to Chitra for first introducing me to the fluctuation-dissipation theorem and always being available to discuss harmonic oscillators, noise, and my often esoteric theoretical questions; to Sandro, for teaching me everything I know about vacuum systems; to Mr. Vogt, Olli, and the mechanical workshop, for machining precision parts and making our experiments possible.

My earlier scientist mentors – Karim, Miriam, Melissa, and Vinny – for first inspiring my interests in the basic sciences and encouraging me to be positively curious.

The Giele – Dänu, Ädu, Flo, and Jäsu – for being wonderful friends; introducing me to the real Switzerland, its wonderful people and places; and, patiently teaching me the wonders of Bernese dialect; Edgar and Marianne, for making Bern my home away from home, by enthusiastically inviting me to Christmas every year and making me feel like part of the family; Giacomo, Michiel, Alice, Guillaume, Caroline, Fabian, Sam, Emily, Luke, Mary, and



---

Damian, for being incredible and supportive friends; Sushil and Neeta, for acting as sources of guidance and peppering me with ideas about science and society; and all my boatmates from PRC, including Max, Kristin, Yvonne, Simon, Paul, Christian, Patrick, Max, and Michael, for patiently teaching me technique and racing starts right at the crack of dawn, helping me clear my mind and start my day fresh with perspective.

My family has always encouraged me to pursue my academic curiosities, even if it meant moving halfway around the world. To my parents, Ajey and Renu, thank you for everything you have instilled within us – diligence, honesty, passion, and curiosity – and for continuing to selflessly pour your love and support into us; you two are the only reason I could make it this far. To Rahul and Ravina, for being my sources of guidance and inspiration; keeping me grounded; and, without a doubt, always looking out for the best for me.

And, to Melanie, for motivating me every step of the way with your infectious smile and enthusiasm; I don't know how I could be so lucky!



---

# Contents

<b>Abstract</b>	<b>i</b>
<b>Zusammenfassung</b>	<b>ii</b>
<b>Acknowledgments</b>	<b>iii</b>
<b>1 Introduction</b>	<b>1</b>
1.1 Quantum Technologies: The State of the Art	1
1.1.1 Quantum Measurements	2
1.1.2 Cavity Opto-Mechanics	3
1.1.3 The Dissipation Challenge	4
1.2 Optical Levitation	5
1.3 Motivation	6
1.4 Outline	7
<b>2 Optical Tweezers and Particle Tracking</b>	<b>9</b>
2.1 Introduction	9
2.2 Optical Tweezers	10
2.2.1 Gradient Force	13
2.2.2 Scattering Force	15
2.2.3 Optical Potential and Escape Rates	16
2.3 Particle Displacement Measurement	18
2.3.1 Scattered field from a nanoparticle	18

2.4	Overview of the Optical Setup	20
2.4.1	Differential detection	21
2.4.2	Balanced homodyne detection	25
2.4.3	Balanced Heterodyne Detection	27
2.5	Feedback Control	28
2.5.1	Phase-locked loops	29
2.5.2	Controlled feedback switching	31
2.6	Laser noise eater	31
2.7	Particle Loading for UHV	32
2.7.1	Ultra-high vacuum techniques	33
2.8	Future Experimental Designs	35
2.9	Conclusion	36
<b>3</b>	<b>Phase Feedback Control</b>	<b>37</b>
3.1	Introduction	37
3.2	Theory of Phase-based Control	39
3.2.1	A Coupled-Oscillator Model	42
3.2.2	Fokker-Planck Equation	44
3.2.3	Amplitude and Energy Distribution	45
3.2.4	Phase Error and Measurement Imprecision	46
3.3	Experimental Results	48
3.3.1	Pressure dependence	50
3.3.2	Energy Distribution under Feedback	53
3.4	Measurement Imprecision in a Parametric Feedback Loop	54
3.5	Conclusion	56
<b>4</b>	<b>Photon Recoil Heating</b>	<b>59</b>
4.1	Introduction	59
4.2	Photon Recoil Heating	61
4.2.1	Force Autocorrelation	64
4.2.2	Optical Temperature	66
4.2.3	Mean Energy Rate of Change	66
4.2.4	Recoil Heating Rate	68
4.3	Experimental Results	70

4.4	Additional Laser Heating Mechanisms	73
4.4.1	Classical intensity noise	74
4.4.2	Trap Center Fluctuations	74
4.4.3	Discussion	75
4.5	Standard Quantum Limit	75
4.5.1	Measurement Imprecision	76
4.5.2	Measurement Backaction	76
4.6	Conclusion	78
<b>5</b>	<b>Noise in the Trap</b>	<b>81</b>
5.1	Introduction	81
5.2	Theory of Parametric Noise	83
5.2.1	Fokker-Planck Equation for Intensity Noise	87
5.2.2	Stationary Amplitude Distribution	88
5.2.3	Trapping Stability Condition	89
5.3	Experimental Results	90
5.3.1	Characterizing Intensity Noise	91
5.3.2	Injecting and Removing Intensity Noise from the Trap	93
5.3.3	Discussion	96
5.4	Frequency Stability	97
5.4.1	Characterizing frequency fluctuations	98
5.4.2	Correlation to Intensity Noise	99
5.4.3	Opto-mechanical Limit	100
5.5	Conclusion	102
<b>6</b>	<b>Resolving the Classical to Quantum Transition</b>	<b>103</b>
6.1	Introduction	103
6.2	The micro-Kelvin regime	104
6.2.1	Reducing Measurement Imprecision	104
6.3	Sideband Thermometry	106
6.3.1	Heterodyne Interferometry	108
6.3.2	Scattering Asymmetry	111
6.3.3	Experimental Implementation	112
6.3.4	Asymmetry-Generating Noise	113

## Contents

---

6.3.5 Proposed Design Changes	119
6.4 Outlook	121
<b>A Mathematical Conventions</b>	<b>123</b>
<b>B Stochastic Averaging under Parametric Modulation</b>	<b>126</b>
<b>C Calculation of the Kramers-Moyal Coefficients</b>	<b>141</b>
<b>D Laser Intensity Stabilization Detector</b>	<b>143</b>
<b>References</b>	<b>145</b>
<b>List of Publications</b>	<b>155</b>
<b>Curriculum Vitae</b>	<b>157</b>

---

## List of Figures

2.1	Focal fields with trapped nanoparticle	11
2.2	The Optical Potential	17
2.3	Particle focal coordinates	19
2.4	Schematic of experimental setup	22
2.5	Detector interferograms	24
2.6	Balanced Homodyne Detection	25
2.7	Homodyne locking with stretched fiber	28
2.8	Phase-locked Loop Control Diagram	31
2.9	Laser Noise Suppression	32
2.10	Intensity stabilized response	33
3.1	Parametric feedback loop	49
3.2	Feedback cooling performance in $y$	51
3.3	Temperature as a function of gain and pressure	52
3.4	Energy distribution under phase feedback.	54
3.5	Measurement imprecision in a PLL	55
4.1	Illustration of photon recoil heating	62
4.2	Photon trail	64
4.3	Power spectral densities under feedback cooling	69
4.4	Steady-state under feedback cooling	71
4.5	Reheating time-traces	72

## LIST OF FIGURES

---

4.6	Standard quantum limit	78
5.1	Laser Relative Intensity Noise	92
5.2	Schematic of intensity stabilization and feedback switching.	93
5.3	Reheating under Laser Intensity Control	94
5.4	Laser RIN Levels	96
5.5	Frequency fluctuations over 1 minute	98
5.6	Correlating frequency and intensity fluctuations	99
6.1	Microkelvin Cooling	105
6.2	Micro-Kelvin Standard Quantum Limit	106
6.3	Heterodyne Interferometry in Backscattering	109
6.4	Scattering Asymmetry Illustration	111
6.5	Amplitude-Phase Correlations.	112
6.6	Heterodyne Spectra in $y$	114
6.7	Local Oscillator Mode Shaping	120
6.8	Hybrid Optical Tweezer and Cavity	121
B.1	PLL Schematic	129
D.1	Laser Intensity Detector	144
D.2	Laser Fluctuations Measurement; PI Control	144



# 1

---

## Introduction

### 1.1 Quantum Technologies: The State of the Art

**W**e are on the brink of a technological revolution – an era in which quantum technologies will finally come to the fore [2]. Developments in quantum computing, sensing, communications, and information processing herald the advent of technologies that harness the curious effects predicted by quantum physics [3]. The revolutionary theory discovered in the 20th century, quantum mechanics, will change the way we access and process our environment. Why then, are quantum technologies arriving now, a century later? A recent article in The Economist highlights that "it has taken so long mainly because the components that make them up had to be developed first: ever-better-lasers, semiconductors, control electronics and techniques to achieve the low temperatures at which many quantum systems perform best." [4]

The unusual characteristics of quantum mechanics provide tantalizing prospects for the development of a whole host of devices, among them extremely precise sensors. In contrast to nano-scale material sensors used in measurements of minute masses, trace analytes, and gases [5], quantum sensors will exploit everything from electronics and optics to acoustics and atomics [3]. Light

will be used to measure, control, and manipulate mechanical objects in the quantum regime, bringing about a paradigm shift in the way we perceive our surroundings [6].

### 1.1.1 Quantum Measurements

The first frontier that brought quantum technologies to the fore was the invention of the laser in the 1960s [7, 8]. Monochromatic sources of light, lasers are the backbone to telecommunications, coherent information processing, and metrology. They offer a vehicle for supreme sensitivity, precision, and accuracy in the measurement of weak signals, feeble forces, and fields.

The laser was an enabling technology in the search for gravitational waves, or the faint ripples of space-time that result from the motion of black holes and permeate the universe [9]. The laser made the gravitational wave search a reality through the technique known as interferometry, in which laser light, split by a beamsplitter, travels back and forth down two separate paths with mirrors precisely positioned at their ends. Kilometer-sized facilities, like the Laser Interferometer Gravitational Wave Observatory (LIGO), were built just for this search. Gravitational waves passing through the interferometer would result in faint contractions or expansions in the trajectory of light and change the intensity of light detected when the laser beams recombine.

Gravitational waves are very weak and detecting them required better lasers, control electronics, and measurement techniques [10]. Better, however, is a relative term whose limits Braginsky sought to elucidate using the fundamental laws of quantum mechanics [11]. At the core of this theory is Heisenberg's Uncertainty Principle, which puts bounds on the precision with which one can simultaneously determine an object's position and momentum, or  $\Delta x \Delta p \geq \hbar/2$  [12].

Braginsky determined that tiny vibrations in the environment would limit the sensitivity with which one could measure fractional changes in the propagation of light in an interferometer. The limit to the detectable force exerted is given by [11]

$$F \geq \sqrt{2mk_B T_0 \gamma / \tau_F} \quad (1.1)$$

which corresponds to the thermal noise background in a force sensor. Here,  $\tau_F$

is the time over which a force acts and imparts momentum to the interferometer,  $m$  is the mirror's effective mass,  $\gamma$  is its intrinsic friction,  $k_B$  is Boltzmann's constant, and  $T_0$  the environmental temperature. Building experiments that could reach this level of sensitivity would have a profound impact on our understanding of fundamental physics [13], leading LIGO to achieve a level of sensitivity one-billionth the size of an atom [14].

One of the unintuitive concepts of quantum theory is that of measurement backaction, by which measuring the state of a system disturbs the system itself. By increasing the amount of light in an interferometer, one can reduce uncertainty in the mirror's position, or  $\Delta x$ . Caves, however, showed that it comes at a cost; more light allows you to better resolve a mirror's position, but the added momentum from the light causes the mirror to shake around more, increasing the uncertainty in its momentum, or  $\Delta p$  [15]. With a proper measurement record of the mirror's motion, one could always counter the influence of measurement backaction using feedback cooling. The effect, however, is so weak that it was not until recent years where measurement backaction was observed in an interferometer [16].

### 1.1.2 Cavity Opto-Mechanics

The second frontier that emerged in the journey to quantum technologies was the advent of high precision manufacturing of nano-scale structures. Combining electrical control with mechanical vibrations, NEMS devices availed a whole new domain of sensing for trace analytes, including everything from mass, pressure, and gases to magnetic fields [5]. When these advanced manufacturing techniques were applied to silicon and glass, microfabrication brought forth a new class of components – opto-mechanical devices, including low loss silica toroids [17], silicon photonic crystals [18], silicon nitride membranes [19], diamond cantilevers [20], that, by design, are high quality Fabry-Pérot cavities. Coupling light into these hybrid optical cavities and mechanical resonators formed a cavity opto-mechanical system, in which light could be used to achieve quantum control over a massive mechanical object [21].

Cavity-optomechanical systems hold promise as a means to both observe and control the quantum states of macroscopic objects and to measure feeble

forces and fields with a sensitivity, precision, and accuracy approaching the quantum limit [6]. With geometries mere microns in size, cavity opto-mechanics seeks to bring the sensitivity of the kilometer-sized LIGO to integrated, chip-scale architectures.

Narrowband mechanical vibrations are coupled with the electromagnetic field, an interaction that is enhanced in the presence of a cavity. The radiation pressure of light is used to control their vibrations and suppress them to the limit imposed by quantum mechanics, which tells us that the vibrations never really stop. The minimum vibration limit occurs in the quantum ground state. Suppressing vibrations is a great technical challenge, which requires pure materials and pristine experimental geometries. However, once a mechanical object is in the quantum ground state, it can be exploited for a whole host of previously inconceivable metrology applications.

Remarkable progress has been made in recent years toward engineering the strong interactions of light and matter at the single-photon level needed to control and communicate with mechanical devices. Among these include the demonstration of strong coupling between an atom and a monolithic silica microtoroid [22]. At the outset of this doctoral work, superconducting microwave circuits [23], silicon nanobeams [24] and silica microtoroids [25] were cooled to the ground state of their mechanical motion using resolved sideband cooling, a familiar technique of the trapped ion community [26]. The sophistication of these mechanical devices enabled the first observations of measurement backaction with silicon nitride membranes [16] and its suppression with measurement feedback at cryogenic temperatures [27]. More recently, quantum correlated light sources were generated from the conversion of mechanical phonons into photons [28], opening up the possibility of mechanical resonators as information transducers in advanced quantum communication protocols [29, 30].

### 1.1.3 The Dissipation Challenge

The challenge in realizing quantum technologies is the same reason so much effort has been invested in nano-scale fabrication and optical metrology: dissipation. When a mechanical resonator is coupled to a bath, like the thermal fluctuations of the environment, the bath has both fluctuations and dissipation,

which act in conjunction to bring a mechanical resonator to a state of thermal equilibrium [31]. In the current state of engineering, quantum systems are still connected to the thermal bath in a non-negligible way. This means that they are forgetful and may lose information that they sense or process. Noise from the environment tickles these quantum sensors the same way that it causes nano-structures to vibrate or makes lasers noisy – via dissipation, which causes a device to lose energy and forget any information it may have stored in it. Reduce dissipation and you can build a quantum computer, sense faint gravitational waves from the universe, detect weak forces, and much more.

Decoherence resulting from dissipation is a challenge because it limits the time over which you can measure a signal in the quantum realm [32]. Micro-structures have come a long way toward reducing dissipation-induced decoherence, but material losses that result from clamping to the environment still limit their performance [33]. One can never truly get rid of dissipation, but we can design ways to reduce its influence.

## 1.2 Optical Levitation

Instead of designing mechanical resonators from the top-down, we levitate small nanoparticles with laser beams. The laser beam and the particle interact via the optical dipole force, which acts to always restore a particle to the center of a focused laser field [34]. Due to the absence of mechanical contact in this system, the dissipation at room temperature can be negligible and the oscillation frequency fully tunable [35], making quantum technologies at room temperature a viable reality.

Optical levitation is a technique first invented by Arthur Ashkin in the 1970s that can be used for precision manipulation and control, spanning from the micron-scale all the way down to the atomic scale [36, 37]. It has formed the basis for cooling experiments involving atoms and ions, enabling the cooling of ions to their motional ground state [38, 39]. Because of optical manipulation, trapped ions are being used to build the very first quantum computing platforms using quantum coherent control of mechanical motion.

Levitating nanoparticles has distinct value in the grand challenges of quantum technologies, namely in precision measurement and control. Foremost,

their mass is very small, which allows for minute force sensitivity (c.f. Eq. 1.1). In ultra-high vacuum, the dissipation they experience is expected to be so little that their achievable Q-factor would be in excess of  $10^{10}$  [40]; a system with such little dissipation would experience very little thermal decoherence, allowing for several oscillations in its ground state of motion. Though their mass is small, it is much greater than that of individual atoms, suggesting that the recoil momentum  $\hbar k^2/2m$  would be negligible; if true, this would allow the scattering of many photons to track the particle's position without affecting its motional state [41]. With very little decoherence and the possibility of many photons interacting with the particle, the prospects for cooling a levitated nanoparticle into its quantum ground state and designing levitated quantum technologies are high.

### 1.3 Motivation

The motivation for this thesis is to cool a levitated nanoparticle into the quantum ground state. Moving toward that goal, we test the assumptions of negligible dissipation in UHV. We are concerned with four key areas that rely on low dissipation promised by levitated optomechanics, including

- **Precision Measurements** How can one use advanced interferometric techniques to probe the particle's motion and conduct high-precision measurements of its position?
- **Nanoscale Manipulation** Can one utilize the momentum of light to achieve a new level of nanoscale control, for the manipulation of nanoscale objects, and the potential of ultra-precise manufacturing?
- **Force Sensing** Would the minute mass and negligible dissipation that a levitated nanoparticle experiences open up a new realm of force sensing that was previously inaccessible?
- **Quantum Opto-mechanics** Will we be able to build quantum states of matter on the nano-scale and use levitated objects as transducers of quantum information?

## 1.4 Outline

This doctoral thesis works toward answering a little bit of each of these questions. It is structured into the following chapters

**Optical Tweezers and Particle Tracking** Designing stable levitation setups requires pristine vacuum environments and advanced, low noise electronics. This chapter presents the experimental methods and conceptual framework needed for optical levitation in UHV.

**Phase Feedback Control** Here, we describe a new feedback cooling protocol and present a toy model for characterizing its operation. We then present experimental results to corroborate our toy model and its enhanced performance over prior techniques. Included is a discussion on the limits of this technique.

**Photon Recoil Heating** This chapter tests the assumption of negligible dissipation in UHV by studying the effects of measurement-induced backaction via photon recoil heating on the levitated nanoparticle.

**Noise in the Trap** To corroborate the limits to dissipation in UHV, we focus in this section on the role of laser noise in reheating and frequency stability. Included is a discussion on the limits to force sensitivity in a levitated nanoparticle trap.

**Resolving the Classical to Quantum Transition** Evidence of a levitated nanoparticle in the micro-Kelvin regime is presented along with a protocol for resolving the transition from the classical to quantum regime using asymmetric sideband thermometry.





# 2

---

## Optical Tweezers and Particle Tracking

The goal of this chapter is to report on the theory of optical tweezers and obtain the relevant opto-mechanical parameters. Then, we describe the experimental construction of a vacuum-compatible optical tweezer and the electro-optics needed to bring a trapped nanoparticle into ultra-high vacuum (UHV). Optical tweezers measurement and calibration methods are presented.

### **2.1 Introduction**

At the heart of this work is the optical tweezer, the indispensable and ubiquitous tool of many physicists and biologists. First invented in the 1970s by Arthur Ashkin [36, 42], optical tweezers use the momentum of light to manipulate nano- and micro-scale objects. Ashkin initially investigated optical tweezers using microparticles in air [43] and in water [44], which are glass spheres a few tens of microns in diameter. When introduced into a focused optical beam, these microspheres experience a restoring force owing to the refraction of light at the glass-air or glass-water interface [42]; the momentum transfer resulting from the radiation pressure of light restores their position to the trap center. Ashkin demonstrated that sub-wavelength particles could be trapped by the

optical gradient force, which results from a particle always trying to maximize its induced dipole moment by seeking out regions of highest intensity.

Ashkin's work laid the foundation for the field of optical manipulation. Optical tweezers were introduced into the atomic community during pioneering experiments on single atom spectroscopy [45], trapped ion control [26], and the formation of exotic states of matter, including Bose-Einstein condensation [46]. Tweezers formed the core of many biophysical mechanistic breakthroughs, including precision force measurements of DNA kinetics [47]. Additional avenues of research demonstrated their use in chemical spectroscopy, lithography, colloid formation, and force microscopy, among the many transformative studies conducted with tweezers underlying them [48]. The ubiquity of optical tweezers is a testament to their versatility.

The experiments in this thesis harness the utility of optical tweezers for the manipulation of nano-scale matter – glass nanoparticles consisting of several ten million of atoms – and the desire to bring these routinely classical objects into a domain where their behavior would be described using quantum theory. In the following sections, we derive the optical trapping forces and express them in a form that is accessible to opto-mechanical experimentalists. Thereafter, we elaborate on the intricate experimental methodology required for accurately tracking and controlling the center of mass motion.

## 2.2 Optical Tweezers

The experiments in this thesis all use nanospheres whose radii are much smaller than the wavelength of light, or  $R \ll \lambda/2\pi$ , which is called the Rayleigh scattering limit. In this limit the nanosphere can be described as point dipole [49].

The electric field  $\mathbf{E}(\mathbf{r}, t)$  illuminating the particle polarizes its internal charges and induces a radiating dipole  $\mathbf{p}$  [50]. The interplay of the dipole moment  $\mathbf{p}$  and the electric field generates a force on the particle and is given by [51]

$$\mathbf{F} = (\mathbf{p} \cdot \nabla)\mathbf{E} + \mathbf{p} \times (\nabla \times \mathbf{E}) + \frac{d}{dt}(\mathbf{p} \times \mathbf{B}) \quad (2.1)$$

where the monochromatic electric field is  $\mathbf{E}(\mathbf{r}, t) = \text{Re}\{\underline{\mathbf{E}}(\mathbf{r})e^{-i\omega t}\}$ , the

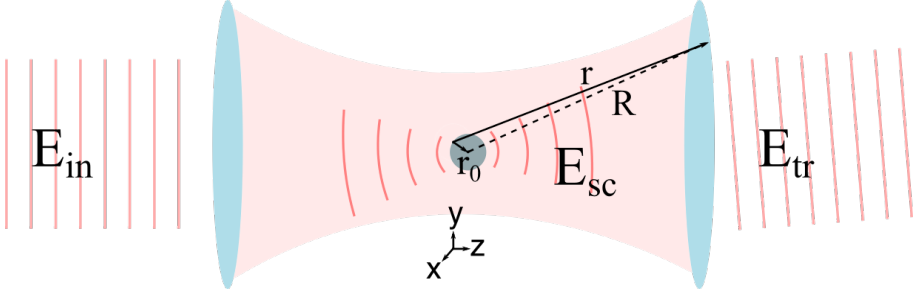


**Figure 2.1: Focal fields with a trapped nanoparticle** An illustration of the focal fields and coordinate geometry for a nanoparticle displaced from the focus. The incident electric field  $\mathbf{E}_{\text{in}}$  is focused with a lens. In the focus is a nanoparticle trapped by the focused laser field but displaced by  $\mathbf{r}_0$ . Its scattered field  $\mathbf{E}_{\text{sc}}$  propagates toward the collection lens in forward scattering to a reference point  $\mathbf{r}$  on the reference sphere of the lens. The difference between the particle position and the imaging point on the lens is  $\mathbf{R} = \mathbf{r} - \mathbf{r}_0$ . The transmitted field  $\mathbf{E}_{\text{tr}}$  experiences a tilt when the particle has a transverse displacement.

magnetic field is  $\mathbf{B}(\mathbf{r}, t) = \text{Re} \{ \underline{\mathbf{B}}(\mathbf{r}) e^{-i\omega t} \}$ , and the dipolar field is  $\mathbf{p}(t) = \text{Re} \{ \underline{\mathbf{p}} e^{-i\omega t} \}$ . Here, bold indicates that these are vector fields and the underline signifies the field's stationary amplitude. The dipolar field amplitude is determined by the polarizability  $\alpha(\omega)$  according to  $\underline{\mathbf{p}} = \alpha \underline{\mathbf{E}}(\mathbf{r})$ . As the fields oscillate on a time-scale much faster than the particle's dynamics, we carry out a time-average over one electric field oscillation cycle,  $2\pi/\omega$ , and find that the average force is given by

$$\langle \mathbf{F} \rangle = \frac{1}{2} \text{Re} \{ (\underline{\mathbf{p}}^* \cdot \nabla) \underline{\mathbf{E}} - i\omega (\underline{\mathbf{p}}^* \times \underline{\mathbf{B}}) \} \quad (2.2)$$

where \* indicates the complex conjugate. The two terms are combined to obtain

$$\langle \mathbf{F} \rangle = \frac{\alpha'}{2} \sum_i \text{Re} \{ \underline{E}_i^* \Delta \underline{E}_i \} + \frac{\alpha''}{2} \sum_i \text{Im} \{ \underline{E}_i^* \Delta \underline{E}_i \} \quad (2.3)$$

when the complex polarizability is split into its real and imaginary components as  $\alpha = \alpha' + i\alpha''$ . The two terms on the right hand side of Eq. 2.3 are called the gradient and scattering forces, respectively. The electric field can be

approximated in terms of its amplitude and phase as  $\underline{\mathbf{E}}(\mathbf{r}) = E_0(\mathbf{r})e^{i\phi(\mathbf{r})}\hat{n}_E$ , such that the time-averaged force is then given by

$$\langle \mathbf{F} \rangle = \frac{\alpha'}{4} \nabla E_0^2 + \frac{\alpha''}{2} E_0^2 \nabla \phi \quad (2.4)$$

The gradient force is a conservative force that results from inhomogeneities of the field's intensity and is proportional to the real (or dispersive) part of the complex polarizability,  $\alpha'$ . The scattering force is a non-conservative force that results from inhomogeneities in the field's phase and is the result of momentum transfer from the laser field to the particle; it is the source of the radiation pressure of light and is proportional to the imaginary (or dissipative) part of the polarizability,  $\alpha''$ . It is through gradients in phase that the particle's motion is driven out of thermal equilibrium. Polarization may also influence the dynamics, but at second order [1]. To stably trap a particle, the gradient force must overcome the scattering force or else the particle is ejected out of the focus.

The polarizability of a dielectric sphere is  $\alpha_0 = 3V\varepsilon_0(\varepsilon_p - \varepsilon_m)/(\varepsilon_p + 2\varepsilon_m)$ , where  $V = (4/3)\pi R^3$  is the volume,  $\varepsilon_p$  is the dielectric constant of the particle, and  $\varepsilon_m$  is the dielectric constant of the medium. The Optical Theorem of light scattering requires energy conservation whenever light is scattered from the particle [49, 50]. To satisfy it, we redefine the sphere's polarizability with an effective form given by [52]

$$\alpha = \alpha_0 \left( 1 - i \frac{k^3}{6\pi\varepsilon_0} \alpha_0 \right)^{-1} \quad (2.5)$$

Accordingly, even when  $\alpha'' = 0$ , the particle's effective polarizability is still complex. This is due to radiation reaction, which results from the particle scattering the incident field as it is accelerated about the focus; when the scattered field carries momentum away, the particle is pushed back in order to conserve total momentum by the radiation reaction force.

The particle is trapped using a zero order Gaussian optical mode focused with a microscope objective with a given numerical aperture, or NA. We restrict the following discussion to the paraxial approximation, which is a small-angle limit in which  $\text{NA} = n \sin \theta \simeq n\theta$ ; we comment later in the text on the

differences arising from this approximation and the full angular description. In this limit, a Gaussian mode can be described in terms of its amplitude and phase forms as

$$E_0(\mathbf{r}) = \underline{E}_0 \frac{w_0}{w(z)} \exp \left[ -\frac{x^2 + y^2}{w^2(z)} \right] \quad (2.6a)$$

$$\phi(\mathbf{r}) = kz - \eta(z) + k(x^2 + y^2)/2R(z) \quad (2.6b)$$

where the waist  $w(z)$ , radius of curvature  $R(z)$ , and Gouy phase shift  $\eta(z)$  are defined as [51]

$$w(z) = w_0(1 + z^2/z_0^2)^{1/2} \quad (2.7a)$$

$$R(z) = z(1 + z_0^2/z^2) \quad (2.7b)$$

$$\eta(z) = \arctan(z/z_0) \quad (2.7c)$$

The beam waist corresponds to the point of minimum divergence; the radius of curvature describes the shape of the focused wavefronts which, by inspection, are planar in the focus; and the Gouy phase shift describes an acquired  $\pi$  phase shift of the focused field from  $z = -\infty$  to  $z = \infty$ . In this paraxial limit, we can approximate the beam waist as  $w_0 = \lambda/\pi\text{NA}$  and the Rayleigh range as  $z_R = \lambda/\pi\text{NA}^2$ , which is the region around the focus where the electric field wavefronts are mostly planar.

### 2.2.1 Gradient Force

Evaluating the forces using Gaussian fields and expanding the force form to the first three orders in  $x$ ,  $y$ , and  $z$ , we calculate the gradient force is equal to

$$\mathbf{F}_{\text{grad}} = \alpha' \underline{E}_0^2 \begin{bmatrix} -\frac{1}{w_0^2} \left(1 - \frac{2}{z_0^2} z^2 - \frac{2}{w_0^2} y^2 - \frac{2}{w_0^2} x^2 + \dots \right) x \\ -\frac{1}{w_0^2} \left(1 - \frac{2}{z_0^2} z^2 - \frac{2}{w_0^2} y^2 - \frac{2}{w_0^2} x^2 + \dots \right) y \\ -\frac{2}{z_0^2} \left(1 - \frac{2}{w_0^2} y^2 - \frac{2}{w_0^2} x^2 - \frac{2}{z_0^2} z^2 + \dots \right) z \end{bmatrix} \quad (2.8)$$

We see here that the forces are linear in first order of position and form, in effect, a restoring force as its form is  $F_{\text{grad}}^i = -k^{(i)} x_i$ . The higher order non-linear terms act to weaken the trap by reducing the trap stiffness,  $k^{(i)}$ ,

proportional to the amplitude of oscillation. The electric field amplitude is not an experimentally accessible measured variable; rather, we can measure intensity,  $I_0$ , or just optical power,  $P_0$ . The field intensity is  $I_0 = \varepsilon_0 c \underline{E}_0^2 / 2 = 2P_0 / \pi w_0^2$ , which results in the spring constants equaling

$$k^{(x,y)} = \frac{4\alpha' P_0}{\pi \varepsilon_0 c w_0^4} = \frac{4\alpha'}{\pi \varepsilon_0 c} \left( \frac{\pi \text{NA}}{\lambda} \right)^4 P_0 \quad (2.9a)$$

$$k^{(z)} = \frac{8\alpha' P_0}{\pi \varepsilon_0 c z_0^2 w_0^2} = \frac{8\alpha'}{\pi \varepsilon_0 c} \left( \frac{\pi \text{NA}}{\lambda} \right)^4 \text{NA}^2 P_0 \quad (2.9b)$$

Here, we see that the spring constant is proportional to optical power, which is in contrast to conventional mechanical oscillators with fixed spring constants given solely by material parameters. For the same optical power, however, reducing the wavelength steeply increases the trap stiffness, proportional to  $\lambda^{-4}$ . Shorter wavelengths can be focused to tighter spots when using the same NA lens, which means the intensity gradient will be sharper. The trap stiffness is also linearly proportional to volume as  $\alpha' \propto V$ . Considering that  $\text{NA} \leq 1.0$  in air, the trap stiffness in the transverse axes ( $x, y$ ) is higher than in the longitudinal direction ( $z$ ).

The gradient force is a conservative force because it is written as the gradient of a potential  $\alpha' \underline{E}_0^2 / 4$  (c.f. Eq. 2.4). Integrating the force in just one dimension in the first order, we calculate the potential is  $U(x_i) = \frac{1}{2} k x_i^2$ , which is the potential energy of an harmonic oscillator. It has a characteristic frequency  $\Omega_i^2 = k^{(i)} / m$ . Despite the sphere's complex polarizability, when its radius is much smaller than the wavelength the oscillation frequencies are equal to

$$\Omega_{x,y}^2 = \frac{12}{\pi c \rho} \left( \frac{\varepsilon - 1}{\varepsilon + 2} \right) \left( \frac{\pi \text{NA}}{\lambda} \right)^4 P_0 \quad (2.10a)$$

$$\Omega_z^2 = \frac{24}{\pi c \rho} \left( \frac{\varepsilon - 1}{\varepsilon + 2} \right) \left( \frac{\pi \text{NA}}{\lambda} \right)^4 \text{NA}^2 P_0 \quad (2.10b)$$

These are the center-of-mass frequencies at which the particle oscillates about the focus. The frequency is independent of the particle's mass; however, changes in the particle's density  $\rho$  will shift its frequency. The frequency changes with the square root of optical power, or  $\Omega_0 \propto \sqrt{P_0}$ .

For a fused silica nanoparticle with density  $\rho = 2200 \text{ kg/m}^3$ , dielectric constant  $\varepsilon = (1.45)^2$ , and trapped with  $P_0 = 70 \text{ mW}$  of power using an NA = 0.80 objective, one would expect oscillation frequencies of  $\Omega_{x,y} = 2\pi 293.0 \text{ kHz}$  and  $\Omega_z = 2\pi 331.5 \text{ kHz}$ . However, at such high numerical apertures, the paraxial approximation is no longer valid and diffractive effects distort the focal intensity. Using the numerical solutions of strongly-focused fields, it was shown that the beam waist is a factor 1.5 times larger in the transverse directions and the Rayleigh range is a factor 2.6 times larger [53]. Accounting for this difference gives trapping frequencies  $\Omega'_{x,y} = 2\pi 114.5 \text{ kHz}$  and  $\Omega'_z = 2\pi 49.0 \text{ kHz}$ , which agree with experiment.

### 2.2.2 Scattering Force

The scattering force is given by

$$\mathbf{F}_{\text{scat}} = \frac{1}{2} \alpha'' \underline{E}_0^2 k \begin{bmatrix} \frac{1}{z_0^2} z x + \dots \\ \frac{1}{z_0^2} z y + \dots \\ \kappa_0 + \kappa_y y^2 + \kappa_x x^2 + \kappa_z z^2 + \dots \end{bmatrix} \quad (2.11)$$

where the  $z$ -component prefactors are given by

$$\kappa_0 = \left(1 - \frac{1}{z_0 k}\right) \quad (2.12a)$$

$$\kappa_{x,y} = \left(-\frac{2}{w_0^2} + \frac{1}{2z_0^2} + \frac{1}{w_0^2 z_0 k}\right) \quad (2.12b)$$

$$\kappa_z = \left(\frac{2}{z_0^3 k} - \frac{1}{z_0^2}\right) \quad (2.12c)$$

The combination of the gradient and scattering force in  $z$  leads to a shift in the trap center that is no longer the center of the focus but is equal to

$$z_c = \frac{1}{4} \frac{\alpha''}{\alpha'} k z_0^2 \kappa_0 \quad (2.13)$$

The shift depends on the particle size and the NA but has no dependence on optical power. It is a result of the momentum transfer from light to the particle in the specific focal geometry.

### 2.2.3 Optical Potential and Escape Rates

The potential is approximated as harmonic; however, the next order components do affect the particle's dynamics. When we reintroduce the cubic nonlinearity of the force in the transverse axes, an integral of the force is equal to

$$U(x) = -\frac{2\alpha'I_0}{\epsilon_0cw_0^2} \left( \frac{1}{2}x^2 - \frac{1}{2w_0^2}x^4 \right) \quad (2.14)$$

This potential experiences a turning point at  $x_{\text{tp}} = w_0/\sqrt{2}$ , which determines the barrier height  $\Delta E = U(x_{\text{tp}}) - U(x = 0) = \alpha'I_0/(4\epsilon_0c)$ , as illustrated in Fig. 2.2. The trapped particle is driven by thermal fluctuations of the environment with average energy  $k_B T_0$  and occasionally samples the quadratic regions of the potential. A well-thermalized quadratic system will have a position probability distribution function given by [54]

$$\rho(x) = \sqrt{\frac{k}{\pi k_B T_0}} \exp \left[ -\frac{1}{4} kx^2 / k_B T_0 \right] \quad (2.15)$$

which gives the probability of achieving the barrier energy and likely escaping from the trap. For a  $R = 68$  nm particle made of fused silica ( $n = 1.45$ ) trapped with a  $\text{NA} = 0.80$  objective at  $\lambda = 1064$  nm using  $P_0 = 70$  mW, the barrier height is  $\Delta E \sim 53 k_B T_0$ , which means the particle is unlikely to be driven out of the trap.

However, there may be interest in using either smaller nanoparticles or reducing the optical power in the trap to scatter fewer photons. When the power is reduced to 16 mW, or by a factor of 4, the oscillation frequency would drop by half and the trap depth drops to  $12 k_B T_0$ . This means particles have a much higher likelihood of escape. Ashkin established trap depths need to be in excess of  $10 k_B T_0$  for stable trapping. If the focal power were kept constant at 70 mW but the particle size were reduced to  $R = 50$  nm, the trap depth would drop to  $\Delta E \sim 21 k_B T_0$ . Reducing focal power or trapping smaller sized particles reduces the trap depth and makes it difficult to stably trap.

Intuitively, this makes sense. For a trapped particle to escape, it has to be driven out by the air molecules that bombard it from all different directions. The



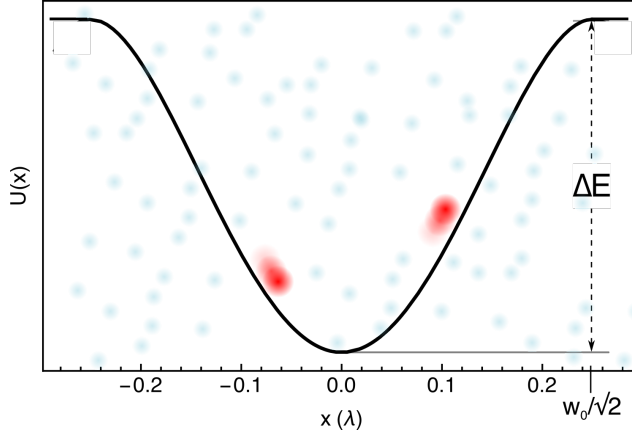


**Figure 2.2: The Optical Potential.** An illustration of the optical potential that the particle moves through, including the non-linearities. The particle (in red) is kicked around by air molecules (in blue) with an average energy of  $k_B T_0$  and thus is driven around the potential. The energy barrier  $\Delta E$  is indicated at the position  $x_{tp} = w_0/\sqrt{2}$ .

momentum transfer needed to kick out a small particle is much less than that for a large particle. Similarly, lower optical power reduces the trap depth and thus requires fewer kicks from the surrounding gas to overcome the potential barrier.

From reaction rates theory [54], we identify Kramer's rate of escape as being the rate at which a particle localized about  $x = 0$  escapes from a potential with barrier turnover at  $x_{tp} = w_0/\sqrt{2}$ , which is given by

$$r = \frac{D}{2\pi k_B T_0} [|U''(x=0)| |U''(x=x_{tp})|]^{1/2} \exp[-\Delta E/k_B T_0] \quad (2.16)$$

where  $D = k_B T_0/m\gamma$  is the diffusion coefficient. For  $U''(x) = -(\alpha E_0^2/w_0^2)(1 - 6x^2/w_0^2)$ , the escape rate equals

$$r = \frac{\sqrt{2}}{\pi\gamma m} \frac{\alpha' I_0}{\epsilon_0 c w_0^2} \exp[-\Delta E/k_B T_0] \quad (2.17)$$

This formula for the escape rate  $r$  is very informative. First, when the focal power is decreased, the barrier height  $\Delta E$  is reduced and thus the rate of escape

increases. Then, when a smaller particle is trapped, the mass  $m$  is lower and the rate of escape increases. The pre-factor  $\sqrt{2}/\pi\gamma m$  is called the attempt rate; by reducing pressure the attempt rate increases, which means the particle is more often attempt to cross the barrier. We return to escape from the potential in Ch. 5.

Loss of trapped particles continues to be an experimental challenge that has thus far only been overcome by shifting the trap to longer wavelengths or by using feedback cooling. I began my work using a laser with wavelength  $\lambda = 532$  nm. When the focal power remains constant, the barrier height is increased and the potential is steeper. Unintuitive as it may seem, this increases the rate of escape. In comparison, using a longer wavelength of  $\lambda = 1550$  nm makes the potential shallower but also broader, which reduces the rate of escape from the trap, a function of the gradient of the potential.

## 2.3 Particle Displacement Measurement

With the formation of a stable trap, one must also be able to track the particle's position. In the following, we calculate the field scattered by the particle and explain optical techniques for tracking.

### 2.3.1 Scattered field from a nanoparticle

The mode illuminating the trapped particle,  $\mathbf{E}$ , and its scattered field,  $\mathbf{E}_{sc}$ , are related through the system's Green's function,  $\vec{\mathbf{G}}(\mathbf{r}, \mathbf{r}_0)$ , according to [51]

$$\mathbf{E}_{sc}(\vec{r}) = \omega^2 \mu \mu_0 \vec{\mathbf{G}}(\mathbf{r}, \mathbf{r}_0) \mathbf{p} \quad (2.18)$$

where the dipole moment is  $\mathbf{p} = \alpha \mathbf{E}$  and the far-field Green's function is

$$\vec{\mathbf{G}}_{\text{FF}} = \frac{\exp[ikR]}{4\pi R} (\vec{\mathbf{I}} - \mathbf{R}\mathbf{R}/R^2) \quad (2.19)$$

for  $\mathbf{R} = \mathbf{r} - \mathbf{r}_0$ ,  $\mathbf{r}$  the distance from the focus to the collection lens, and  $\mathbf{r}_0$  the position of the scattering nanoparticle. The particle is illuminated by a Gaussian mode of the form in Eq. 2.6, which is a field linearly polarized in  $x$ . The field

scattered by the particle is given by

$$\mathbf{E}_{sc} = \omega^2 \mu \mu_0 \frac{\exp[ikR]}{4\pi R^3} \begin{bmatrix} R^2 - R_x R_x & -R_x R_y & -R_x R_z \end{bmatrix}^T \quad (2.20)$$

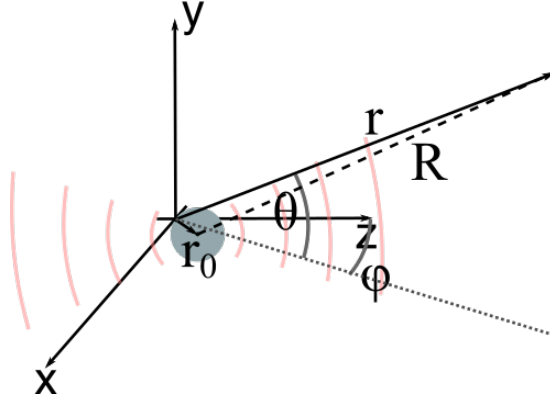


**Figure 2.3:** An illustration of the particle's position  $\mathbf{r}_0$  with respect to the focus and the coordinates of the reference sphere of the lens, or  $(r, \theta, \phi)$ .

The  $y$  and  $z$  components of the scattered field are weakly contributing at the collimation lens. The particle's scattered field at the collimation lens is

$$\mathbf{E}_{sc}^{(x)} = \omega^2 \mu \mu_0 \frac{\exp[ikf]}{4\pi f} \alpha E(\mathbf{r}_0) \exp[-ik(\mathbf{r}_0 \cdot \mathbf{r})/f] \quad (2.21)$$

Its location is  $\mathbf{r}_0 = (x_0, y_0, z_0)$  and the lens is placed far enough that  $f \gg z_R$ . The position on the reference sphere of the lens is  $\mathbf{r} = f(\sin \theta \cos \phi, \sin \theta \sin \phi, \cos \theta)$ . Here, we approximate  $|\mathbf{R}| = |\mathbf{r} - \mathbf{r}_0| = \sqrt{r^2 - 2\mathbf{r} \cdot \mathbf{r}_0}$  at  $r = f$ . The field wavefronts can be spatially mapped at  $r$  with the inclination angle  $\theta$  and rotation angle  $\phi$  of collection, as illustrated in Fig. 2.3. The total intensity after the two fields interfere is  $I = |\mathbf{E} + \mathbf{E}_{sc}|^2$ , given by

$$I(t) = |\mathbf{E}|^2 + |\mathbf{E}_{sc}|^2 + 2\alpha E_0 E(\mathbf{r}_0) \frac{\omega^2 \mu \mu_0 z_R}{4\pi f^2} \exp\left[-\frac{\rho^2}{w_0^2(f^2/z_R^2)}\right] \times \sin(k(x_0 \sin \theta \cos \phi + y_0 \sin \theta \sin \phi + z_0 \cos \theta)) \quad (2.22)$$

The resulting interference signal for small displacements ( $kr_0 \ll 1$ ) is

$$\begin{aligned} \delta I[r_0; \theta, \phi] &= 2\alpha E_0 E(\mathbf{r}_0) \frac{\omega^2 \mu \mu_0 z_R}{4\pi f^2} \exp \left[ -\frac{\rho^2}{w_0^2 (f^2/z_R^2)} \right] \\ &\times k(x_0 \sin \theta \cos \phi + y_0 \sin \theta \sin \phi + z_0 \cos \theta) \end{aligned} \quad (2.23)$$

We see from Eq. 2.21 that a shift in position results in a change in the scattered field's phase. The scattered field interferes with the trapping field to project a phase change into an intensity change. Importantly, the trapping field and scattered field are offset in phase by  $\pi/2$  at the collection lens because of the Gouy phase shift. Accordingly, this automatically projects the phase quadrature of the optical field rather than its amplitude.

The scattered power is obtained by integrating the time-averaged radiated energy  $\langle \mathbf{S} \rangle = \langle \mathbf{E}_{\text{sc}} \times \mathbf{B}_{\text{sc}}^* \rangle$  on the surface of a sphere  $a$ , or

$$\begin{aligned} P_{\text{sc}} &= \oint_a \langle \mathbf{S} \rangle \cdot d\mathbf{a} = 2 \left( \frac{k^3 |\alpha|}{6\pi \epsilon_0} \right)^2 \eta_{\text{fs}} P_0 \\ &= 2[\alpha''/\alpha_0]^2 \eta_{\text{fs}} P_0 \end{aligned} \quad (2.24)$$

where  $\eta_{\text{fs}} = 6/(k^2 w_0^2)$  is the single particle cooperativity in free space [55] and  $\text{Im}\{\alpha\} = \alpha'' \simeq k^3 \alpha_0^2 / (6\pi \epsilon_0)$  is the imaginary component of the polarizability in Eq. 2.5 satisfying the Optical Theorem. The free-space cooperativity is independent of the polarizability and is a geometric quantity equal to the ratio of emission into the zero order Gaussian mode that illuminates the particle (both forward and back) and the total free space emission into a solid angle of  $4\pi$ . In the paraxial approximation, we find that  $\eta_{\text{fs}} = \frac{3}{2} \text{NA}^2$ , which tells us that increasing the numerical aperture of the illumination (and collection) optics would increase the fraction of the scattered field that is collected from the trap.

## 2.4 Overview of the Optical Setup

The experimental methods presented here were mostly developed or implemented over the course of this thesis work. The optical setup was designed for stable trapping of a dielectric nanoparticle with a single microscope objective

oriented in the horizontal configuration [42]. In this section, we discuss different interferometric measurement techniques for tracking the particle's motion [56].

### 2.4.1 Differential detection

The transmitted laser field is split three ways and then focused onto a photodetector. The scattered field is collected at angles  $\theta \in (0, \theta_{\max}]$  (for  $\theta_{\max} = \arcsin(\text{NA})$ ) and  $\phi \in (0, 2\pi]$ . Assuming the particle's displacement is small,  $\mathbf{k} \cdot \mathbf{r}_0 \ll 1$ , the output photocurrent is given by

$$\begin{aligned} i_z(t) &= \int_0^{2\pi} d\phi \int_0^{\theta_{\max}} d\theta \sin \theta \delta I[r_0; \theta, \phi] \\ &= \beta k \pi \text{NA}^2 z_0 \lim_{\text{NA} \rightarrow 1} \beta \pi k z_0 \end{aligned} \quad (2.25)$$

where  $\beta = \alpha E_0 E(\mathbf{r}_0) (\omega^2 \mu \mu_0 z_R / (4\pi f^2)) \exp[-\rho^2 / (\omega_0^2 f^2 / z_R^2)]$ . A separate, unmodulated field is sent to the other port of the balanced detector to subtract away the DC photocurrent and remove the common-mode fluctuations in laser intensity [57].

Next, the left and right halves of the field are split using a knife-edge mirror; each half is redirected to separate ports in a balanced photodetector. The field in the left half subtends  $\phi_L \in (-\pi/2, \pi/2]$  and in the right half subtends  $\phi_R \in (\pi/2, 3\pi/2]$ . The output photocurrent is given by

$$\begin{aligned} i_x(t) &= \int_0^{\theta_{\max}} d\theta \sin \theta \left( \int_{-\pi/2}^{\pi/2} d\phi \delta I[r_0; \theta, \phi] - \int_{\pi/2}^{3\pi/2} d\phi \delta I[r_0; \theta, \phi] \right) \\ &= 2\beta k \pi x_0 (-\text{NA} \sqrt{1 - \text{NA}^2} + \arcsin(\text{NA})) \lim_{\text{NA} \rightarrow 1} \beta \pi k x_0 \end{aligned} \quad (2.26)$$

Finally, the top and bottom halves of the field are split such that the top half subtends  $\phi_T \in (0, \pi]$  and the bottom half subtends  $\phi_B \in (-\pi, 0]$ . The output

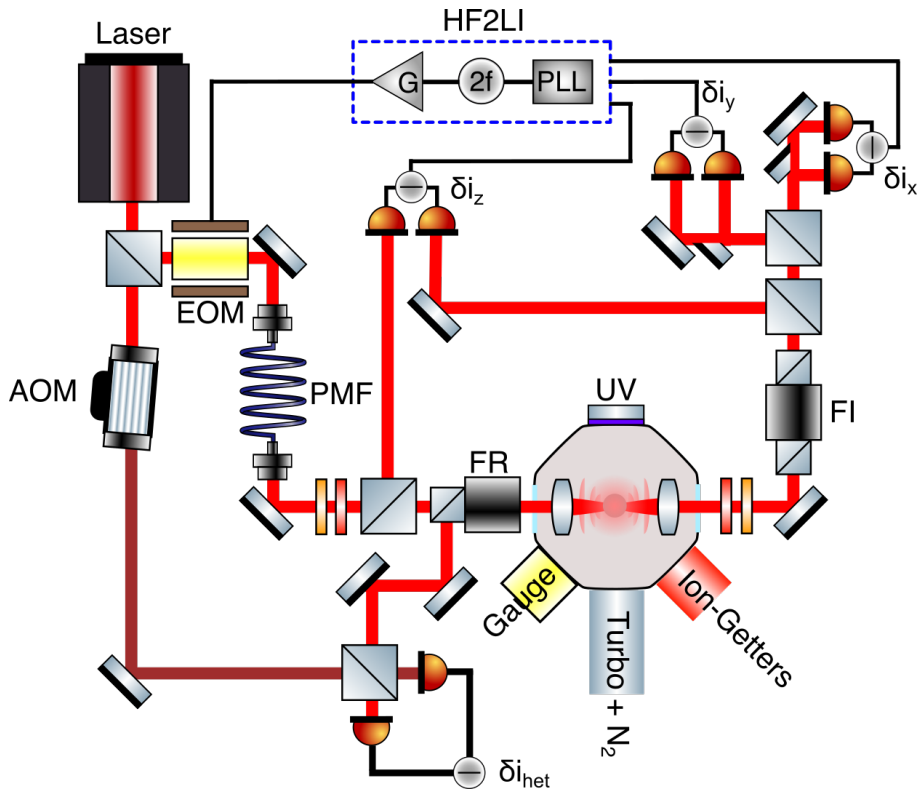


**Figure 2.4:** A schematic of the experimental setup. Laser light is coupled through an EOM and a single-mode polarization maintaining fiber (PMF) and then directed into the vacuum chamber. At the input to the vacuum chamber is a Faraday rotator (FR) to separate illuminating and back-scattering light. In the forward propagating direction is a Faraday isolator (FI) to suppress back-reflections into the trap and thereafter a set of three balanced photodetectors. The output of the photodetectors are connected to digital PLLs, frequency doubled, and then connected to the EOM with a fixed gain,  $G$ . Around the vacuum chamber are a UV lamp for use during pumpdown; a combination Pirani and Ion gauge for tracking vacuum pressure; a line to the turbopump; and an ion-getters pump. The laser beam enters and exits through anti-reflection coated, vacuum-compatible windows.

photocurrent is then given by

$$\begin{aligned}
 i_y(t) &= \int_0^{\theta_{\max}} d\theta \sin \theta \left( \int_0^{\pi} d\phi \delta I[r_0; \theta, \phi] - \int_{-\pi}^0 d\phi \delta I[r_0; \theta, \phi] \right) \quad (2.27) \\
 &= 2\beta k\pi y_0 (-\text{NA} \sqrt{1 - \text{NA}^2} + \arcsin(\text{NA})) \lim_{\text{NA} \rightarrow 1} \beta\pi k y_0
 \end{aligned}$$

When the particle moves in the transverse directions, its scattered field shifts with respect to the focus, which causes either a vertical (for  $y$  motion) or horizontal (for  $x$  motion) deflection of the transmitted fields. Motion in  $z$  amounts to a slight focusing or defocusing of the scattered field with respect to the stationary trap.

The intensity change at the plane of the photodetector is seen in Fig. 2.5. Shown are calculated contour plots of the intensity change when the particle is displaced in just one direction, either in  $z$ ,  $y$ , or  $x$ , respectively, by a distance  $\pm\lambda/20$ . The yellow coloring indicates an increase in intensity and the blue coloring indicates a decrease in intensity. When the particle moves in  $z$ , the interference of its scattered field with the transmitted laser field results in a symmetric interferogram whose total intensity changes. A displacement in the  $y$  axis results in the intensity of the top half increasing and the bottom half decreasing when the particle moves up and the reverse when it moves down. Thus the intensity change is asymmetric about the top and bottom halves. Similarly, a displacement in the  $x$  axis results in an intensity change in the left and right halves of the detected interference. Using split mirrors selects either the top and bottom or left and right halves for tracking just the corresponding axis of motion.

### 2.4.1.1 Homebuilt Photodetectors

The measurements presented in this thesis were taken using a variety of photodetectors. In Chs. 3 and 4, free-space balanced detectors from Newport (Model 2117-FS-M) were used for feedback cooling and reheating measurements. Later, in Chs. 5 and 6, homebuilt detectors based on Excelitas C30642GH and JDSU ETX500/1000 photodiodes were used. Designs for the photodetectors are presented in the Appendix. They were built in three configurations

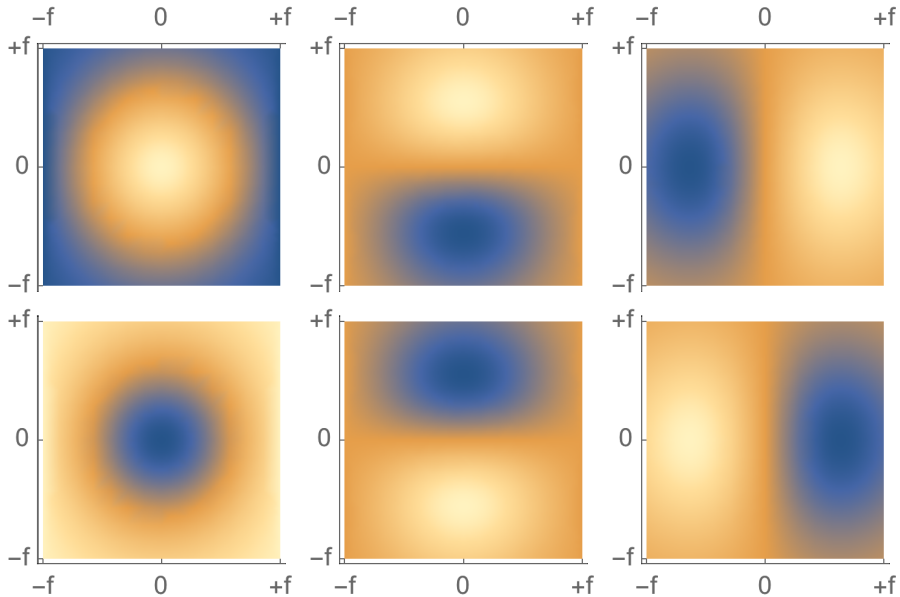


**Figure 2.5: Detector interferograms.** Density plots of the intensity at the detector plane from the interference of the scattered and transmitted fields. Shown are the interferograms in z, y, and x (from left to right) when the particle is displaced along just the corresponding axis by either  $+\lambda/20$  (top) or  $-\lambda/20$  (bottom). Yellow indicates an increase in intensity and blue indicates a decrease. A particle moving in the focus will generate a time-varying intensity at the photodetector.

1. C30642GH : Using an OPA656 operational amplifier to achieve a 10 MHz bandwidth with up to 100 mW of optical power.
2. ETX1000 : Using an OPA656 operational amplifier to achieve a 10 MHz bandwidth for a maximum of 20 mW in detection.
3. ETX500 : Using an OPA846 operational amplifier to achieve a 40 MHz bandwidth with up to 20 mW of optical power in balanced detection.

Extreme care was taken in developing a very low noise design such that shot noise is the dominant noise process for more than 1 mW of optical power.



### 2.4.2 Balanced homodyne detection

The split, or differential, detection method is the conventional detection technique for motion in an optical tweezer trap. It is an interferometric technique that relies on the common path of propagation for both the trapping and scattered fields and their matching wavefronts and phase profiles. In addition to forward scattering, the particle equally scatters the laser field into the backwards direction. Collecting this back-scattered light can enable one to independently modulate the reference field from the scatter. Guiding the back-scatter onto a beamsplitter, we separately introduce a reference field  $E_{lo}$ .

The inputs to the beam splitter are the scatter from the particle  $E_{sig}$  and an independent reference  $E_{lo}$ , where

$$\begin{aligned} E_{sig} &= E_1 \exp[i\phi_1] \\ E_{lo} &= E_2 \exp[i\phi_0] \end{aligned} \quad (2.28)$$

and the outputs are given by

$$\begin{aligned} E_+ &= r e^{i\phi_{rf}} E_{sig} + t e^{i\phi_t} E_{lo} \\ E_- &= t e^{i\phi_t} E_{sig} + r e^{i\phi_{rb}} E_{lo} \end{aligned}$$

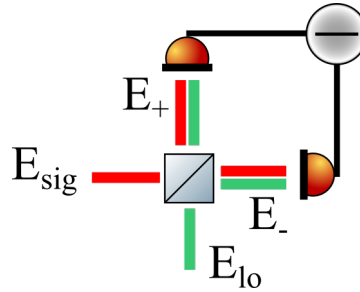


**Figure 2.6: Balanced Homodyne Detection.** Two fields are input to a beam splitter,  $E_{sig}$  and  $E_{lo}$ . The outputs are  $E_+$  and  $E_-$  whose difference is taken by the balanced photodetector.

where (+) and (-) are sketched in Fig. 2.6. The resulting intensities are

$$\begin{aligned} |E_+|^2 &= |r|^2 |E_{sig}|^2 + |t|^2 |E_{lo}|^2 + 2rtE_1E_2 \cos(\phi_1 - \phi_0) \\ |E_-|^2 &= |t|^2 |E_{sig}|^2 + |r|^2 |E_{lo}|^2 - 2rtE_1E_2 \cos(\phi_1 - \phi_0) \end{aligned} \quad (2.29)$$

where  $\phi_t = 0$ ,  $\phi_{r_f} = 0$ , and  $\phi_{r_b} = \pi$ . Here, we adopt the convention that the beamsplitter is asymmetric as is experimentally the case [58]. When  $r = t = 1/\sqrt{2}$ , the detector output signal is

$$I = 2E_1E_2 \cos(kx(t) - k\delta x) \quad (2.30)$$

when  $\phi_1 = kx(t)$  and  $\phi_0 = k\delta x$ , where  $\delta x$  corresponds to the local oscillator's tunable path length and  $x$  is an arbitrary coordinate. The detector output will change as a function of  $\delta x$ , which means the signal will drift in and out of interference. If  $k\delta x$  is adjusted to the phase quadratures, then the detected signal varies between the cosine and sine of the phase, or

$$\begin{aligned} k\delta x = n\pi & : I = 2E_1E_2 \cos(kx(t)) \\ k\delta x = (2n+1)\pi/2 & : I = 2E_1E_2 \sin(kx(t)) \end{aligned} \quad (2.31)$$

To calibrate our spectra, we can introduce a path length modulation such that the local oscillator field is

$$E_{lo} = E_2 \exp[i\phi_0] = E_2 \exp[ik\delta x + ikx_1 \sin(\Omega_1 t)] \quad (2.32)$$

When  $\delta x = \pi/(2k)$ , the detector output signal is

$$I \simeq 2E_1E_2 \sin\{k(x(t) - x_1 \sin(\Omega_1 t))\} \quad (2.33)$$

The two-time auto-correlation function of this detected signal is

$$\begin{aligned} R_I &= E[I(t)I(t+\tau)] \\ &= (2E_1E_2k)^2 \{E[x(t)x(t+\tau)] + \frac{1}{2}x_1^2 \cos(\Omega_1\tau)\} \end{aligned} \quad (2.34)$$

Thus, the variance, which is the on-time autocorrelation of the detector signal,

is given by

$$R_I(0) = (2E_1 E_2 k)^2 \{ \langle x^2 \rangle + \frac{1}{2} x_1^2 \} \quad (2.35)$$

We calibrate the particle displacement spectrum using such a calibration tone at  $\Omega_1$ . First, we set a known modulation depth by determining the voltage needed for one wavelength of path length change at  $\Omega_1$ . Then, locking the DC path length, we apply a weak single-tone modulation at  $\Omega_1$  and compare its noise power to that of the particle oscillation. Experimentally, this was tested in  $z$  at  $P_{\text{gas}} = 15$  mbar. The measured mean squared displacement from particle oscillation was  $\langle x^2 \rangle_{\text{meas}} = (120.7 \text{ nm})^2$ , which corresponds to that for a particle with radius  $R = 68$  nm in a bath at  $T_0 = 300$  K (or  $\langle x^2 \rangle_{\text{th}} = (120.3 \text{ nm})^2$ ).

#### 2.4.2.1 Piezo-based fiber stretcher

A phase-modulating fiber stretcher was constructed to lock the local oscillator's path length and apply phase modulations [59]. This was constructed using a single mode, polarization maintaining fiber (ThorLabs) wound around a split plastic disk (self-designed and 3D printed) with a piezo plate (Noliac NAC2123) at the center. The piezo was modulated using a high-voltage amplifier (Falco), which resulted in a modulation of the path length traversed by the guided field, as sketched in Fig. 2.7.

The output voltage detected in the balanced homodyne interferometer was used as an error signal to stabilize the path-length to a given setpoint, which corresponds to a given phase angle, as illustrated in Fig. 2.7.

#### 2.4.3 Balanced Heterodyne Detection

Converting the local oscillator to a frequency-shifted reference with an acousto-optic modulator (AOM), the reference field becomes  $E_2 \exp[i(\omega + \delta\omega)t]$ . The detected signal in a balanced configuration is given by

$$\begin{aligned} I(t) &= 2E_{\text{sc}} E_{\text{ref}} \cos(kx(t) + \delta\omega t) \\ &\simeq 2E_{\text{sc}} E_{\text{ref}} (\cos(\delta\omega t) - kx_0 \cos((\Omega_0 - \delta\omega)t) + kx_0 \cos((\Omega_0 + \delta\omega)t)) \end{aligned} \quad (2.36)$$

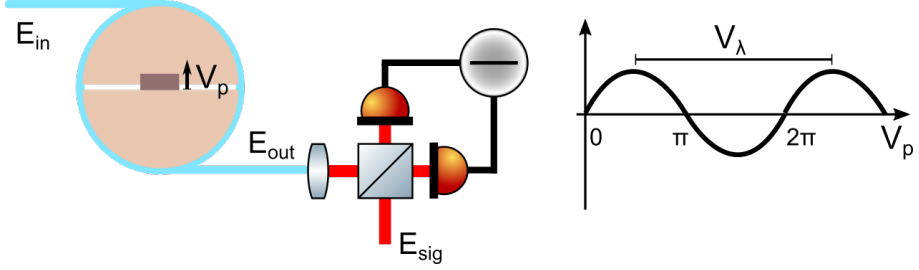


**Figure 2.7: Homodyne locking with stretched fiber.** A schematic of a homodyne interferometry locking scheme. The scattered field, here denoted  $\mathbf{E}_{\text{sig}}$  is interfered at the beamsplitter with a reference field  $\mathbf{E}_{\text{out}}$ . The reference field  $\mathbf{E}_{\text{out}}$  is the output of a fiber that is stretched using a piezo plate. The output signal from the balanced detector is modulated based on the path length difference and can be used as an error signal for controlling the piezo stretch.

which was simplified by assuming  $kx_0 \ll 1$ . The single-sided Fourier transform of this signal is

$$\hat{I}(\omega) = 2E_{\text{sc}}E_{\text{ref}}(\delta(\omega - \delta\omega) + kx_0\delta(\Omega_0 + \delta\omega - \omega) + kx_0\delta(\Omega_0 + \delta\omega - \omega)) \quad (2.37)$$

which shows us that there is a carrier at  $\omega = \delta\omega$  and sidebands at  $\omega = \Omega_0 + \delta\omega$  and  $\omega = \delta\omega - \Omega_0$ . The amplitudes of the spectral peaks are related to the carrier by  $kx_0$ .

## 2.5 Feedback Control

The essential element in the experiments covered in this thesis is the feedback controller. In contrast to previous work on parametric modulation [60, 61] the feedback control signal was generated by a phase-locked loop (PLL). A PLL is an oscillator that synchronizes its phase to that of a reference [62]. PLLs have been used for several decades now for low-noise, phase-locked frequency division and multiplication [63] because they are the optimal phase tracking topology [64].

### 2.5.1 Phase-locked loops

Using the split detection scheme of Section 2.4.1, each detector output was fed into the signal port of a Zurich Instruments (ZI) Lock-In Amplifier (Model: HF2LI). With each detector signal, a PLL was tuned to track the particle's oscillation frequency and phase. The tuning parameters included: center frequency ( $f_0$ ), locking range ( $f_R$ ), phase offset ( $\phi_{pll}$ ), phase detector time constant ( $\tau_{pd}$ ), proportional gain, integrator time constant, gain ( $\eta$ ), phase delay ( $\phi_d$ ), and harmonic ( $n$ ).

**Table 2.1:** Tuning parameters of the PLLs for tracking in all three axes.

Axis	$f_0$	$\tau_{pd}$	P Gain	$\tau_i$
Z	45 kHz	10 $\mu$ sec	292	10 m
X	120 kHz	10 $\mu$ sec	2910	12 m
Y	150 kHz	10 $\mu$ sec	723	29 m

The tuned parameters are listed in Table 2.1. These parameters ensured that phase fluctuations in the particle's oscillation in a bandwidth of 1 kHz about the center frequency were tracked in each axis. Additionally, the locking range was held to  $f_R = 7$  kHz, the phase offset from the detected signal was  $\phi_{pll} = 90^\circ$ , and the second harmonic ( $n = 2$ ) of the PLL signal was used. All three signals were summed together and connected to the input of the EOM's high-voltage amplifier. Typical modulation depths used were  $\sim 1\%$ .

#### 2.5.1.1 Theory of Phase-Locked Loops

The phase-locked loop (or PLL) has been used as a coherent detector of communications signals for several decades [62, 65]. It continuously corrects its local oscillator frequency according to a measurement of the phase error.

The signal at the detector corresponds to the particle's position corrupted by some shot noise from the measurement, or  $v_i(t) = x(t) + \xi(t)$ . The particle's motion generates a signal at the detector that is approximately  $x(t) = A \sin[\Omega_0 t + \theta_1(t)]$ . The shot noise is taken to be white noise around the oscillation frequency. We can approximate its contribution as  $\xi(t) = \xi_1(t) \sin(\Omega_0 t) + \xi_2(t) \cos(\Omega_0 t)$ , where  $\xi_1, \xi_2$  represent two independent, uncorrelated, and

randomly varying quadratures of the noise.

It is first mixed with the output of a voltage-controlled oscillator whose signal is  $v_o(t) = B \cos[\Omega_0 t + \theta_2(t)]$  and then passes through a filter with the transfer function  $F(s)$ . The output voltage is fed to a voltage-controlled oscillator (VCO), which acts as an integrator and adjusts its output phase proportional to the input error voltage.

The loop error signal is then [65]

$$e(t) = F(s)(v_i(t) \cdot v_o(t)) \quad (2.38)$$

$$= A \sin[\theta_1(t) - \theta_2(t)] + n_1(t) \cos[\theta_2(t)] + n_2(t) \sin[\theta_2(t)] \quad (2.39)$$

The VCO is an integrator whose output is governed by

$$\frac{d\theta_2}{dt} = K_v e(t) \quad (2.40)$$

Redefining the instantaneous phase error as  $\phi(t) = \theta_1(t) - \theta_2(t)$ , the phase evolution is given by

$$\begin{aligned} \dot{\phi}(t) &= \dot{\theta}_1 - \frac{1}{2} K_v B (A \sin \varphi - \xi_1 \sin \theta_2 + \xi_2 \cos \theta_2) \\ &= -K [A \sin \phi(t) + n'] \end{aligned} \quad (2.41)$$

when  $\dot{\theta}_1 = \omega - \omega_0 = 0$  and  $K = 4B_L/A$ , for loop bandwidth  $B_L$  and  $n' = -\xi_1 \sin \theta_2 + \xi_2 \cos \theta_2$ . This is the equation of motion for the steady state phase error when the oscillator measurement is corrupted by noise. The equation is exactly that for the motion of a pendulum driven by additive random noise [66].

The behavior of a PLL is best understood in the steady state, in which the VCO is synchronized with the oscillation phase and the steady-state phase error  $\phi(t)$  is small. Thereby, we approximate  $\sin(\phi(t)) \sim \phi(t)$  and assume that the measurement noise is weak enough that the PLL does not lose its lock; we will return to the role of measurement noise in Sec. 3.4. The phase dynamics are then most easily solved using Laplace transforms, whereby Eq. 2.41 becomes

$$\Phi[s] = \frac{K N_0}{s + KA} \quad (2.42)$$

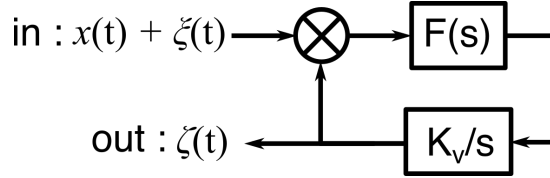


**Figure 2.8:** A phase locked-loop consists of a phase-detector (the mixer), a loop filter ( $F(s)$ ), and a voltage-controlled oscillator ( $K_v/s$ ). The output of the VCO is updated according its phase difference with the detected particle oscillation.

where  $\Phi[s]$  is the transform of  $\phi(t)$  and  $N_0$  is the power spectral density of the noise. Steady-state phase error, or  $\phi_e = \lim_{s \rightarrow 0} s \Phi[s] = 0$ . Using a second order filter and recognizing that a change in phase is a change in frequency, or  $\frac{d\phi}{dt} = \Omega$ , shifts in the center frequency can also be compensated.

In the steady-state of phase tracking with an appreciably large input signal to noise ratio, the PLL's phase is synchronized with the particle's oscillation phase. The measurement noise is an additive noise process and is equally amplified as the particle's oscillation signal is by the mixer.

### 2.5.2 Controlled feedback switching

For experiments on the reheating of the particle's motion, Proportional, Integral, and Derivative (PID) Controllers also on the ZI were used to toggle the feedback control on and off. When a TTL pulse with amplitude  $V_{TTL} = 0.5$  V enters the PID, the controller (with P gain = 1 V/V and  $\tau_I = 10$  msec) reacts immediately and saturates the output to zero; when the TTL pulse settles again, the output returns to the original feedback gain  $\zeta_0$ . The rise time is much shorter than the particle oscillation, which allows us to controllably switch the feedback in our reheating experiments. Feedback control can be synchronously triggered on and off in each axis along with the data acquisition.

## 2.6 Laser noise eater

Tests of noise contributions in the trap necessitated the development of a laser noise eater. The device is capable of measuring up to 100 mW of optical power

and actuates the EOM for reduced laser amplitude noise.

As seen in Fig. 2.9, a single photodiode is used for detecting the laser intensity fluctuations. In the photodetector circuit, a very low noise DC current source exists to subtract the DC photocurrent; the output can then be used as an error signal for intensity noise reduction and as a DC-level stabilization reference. This was used in studies of laser noise heating in Ch. 5.

The device contains an on-board PID controller, which reduces noise in a 500 kHz bandwidth. The designs and components are included in the Appendix.

Shown in Fig. 2.10 is a sample time trace of the laser's intensity fluctuations with (in red) and without (in blue) the noise suppression. The trace is taken for  $P_0 = 6.7$  mW of detected optical power. Noise is suppressed by a factor of 15.

## 2.7 Particle Loading for UHV

Perhaps the most essential component to the experiment is the nanoparticle itself. Fused silica nanoparticles used in these experiments were obtained from Microparticles GmbH, MSP NanoSilica, and Bangs' Laboratories. The bulk of the measurements were with diameter  $d = 136$  and  $177$  nm from Microparticles GmbH and with  $d = 100$  nm from MSP NanoSilica.

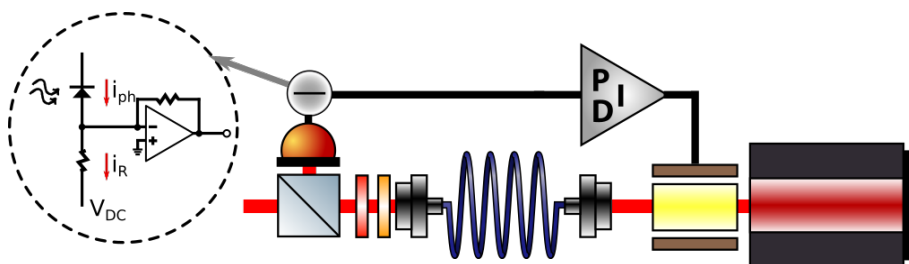


**Figure 2.9: Laser noise suppression.** The output of the laser passes through an EOM and then through a polarization maintaining single mode fiber. A small fraction of the fiber output is deflected onto a photodetector with a built in PID controller; the device is positioned just before the input to the chamber. The error signal from the PID controller is then fed into the EOM to suppress intensity noise. The laser beam output from the beam splitter is then fed directly into the trapping objective in the vacuum chamber.



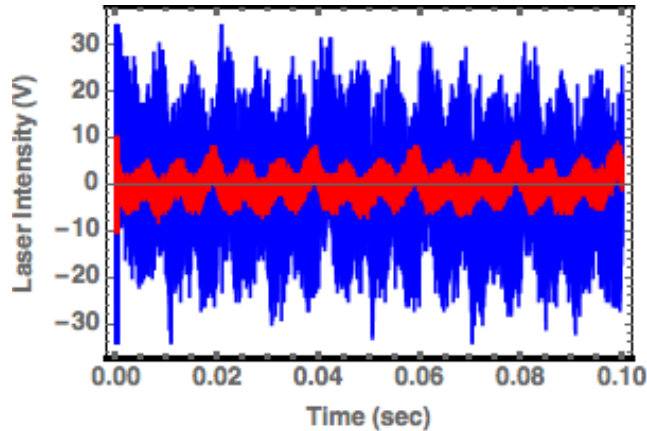


**Figure 2.10: Intensity stabilized response.** A sample time trace of the laser intensity fluctuations on the detector in blue and under control with the noise eater in red.

Two milliliters of a nano-Molar solution of the nanoparticles was used in an Omron nebulizer (Model MicroAIR U22) to inject the particles in the focus. Each particle was encapsulated in a drop of isopropanol and as it traversed the focus was captured by the optical gradient force. The isopropanol evaporates away quickly when the particle is trapped and the nanoparticle remains.

### 2.7.1 Ultra-high vacuum techniques

An important component of the experimental apparatus is the vacuum pump in order to bring the nanoparticle into ultra-high vacuum. A scroll pump (Agilent Model S110) was used to back a turbopump (Agilent Model TwisTorr 304 FS) for evacuating the system. The challenge in achieving UHV is the outgassing of water vapor from the chamber walls. Two strategies enabled pressures lower than  $10^{-8}$  mbar, including dry-nitrogen backfilling and ultra-violet light illumination. A combination Pirani and ion gauge (InstruTech Hornet and IGM402 Module) was used to track vacuum pressure.

The conventional strategy for reaching UHV is to bakeout the entire vacuum system for an extended period of time. Outgassing rates from adsorbates to the chamber walls increase when the walls are heated, as the long-time outdiffusion

rate  $q$  of vapor from a solid is given by [67]

$$q = \frac{2DC_0}{d} \exp \left[ -\frac{\pi^2 Dt}{4d^2} \right] \quad (2.43)$$

which indicates that the outgassing rate by diffusion decreases as  $\exp[-aDt]$  at long times  $t$ . For practical purposes in the experiment, we seek to reduce the outgassing time in order to more rapidly bring a nanoparticle into UHV. Increasing the chamber's temperature during pumpdown for an extended period of time increases the gas' diffusion constant  $D = D_0 \exp[-E_D/k_B T_0]$ . Several attempts at controlled bakeout with a trapped particle in the focus under feedback were unsuccessful. During bakeout, the optical components expanded and the signal to the detectors drifted. Without aligned detectors to track the particle's motion and then feedback cool it, it is not possible to maintain the particle trapped into UHV.

An alternate approach was developed using dry nitrogen. After an overnight bakeout of the vacuum chamber at 100-120°C, the chamber reached a pressure of  $10^{-8}$  mbar. Then, the chamber was backfilled to atmosphere with dry nitrogen ( $< 3$  ppm  $H_2O$ ); a particle was trapped in the open chamber in under 5 min; and then the entire system was closed off and pumped down. After one day of pumping, pressures of  $3 \times 10^{-8}$  mbar were typically achieved.

The ability to return to UHV pressures despite limited exposure to ambient conditions is the result of backfilling with dry nitrogen, which after a bakeout becomes the primary surface adsorbate. The outgassing rate of dry nitrogen is two orders of magnitude lower than that of air, which means for the same pumping speed, one can reach two orders of magnitude lower in pressure [68].

Additionally, an ultra-violet lamp was used to accelerate desorption of water molecules. A vacuum-compatible ultra-violet lamp from RBD Instruments (Model MiniZ UVC) was installed and illuminated during pumpdown after the dry nitrogen purge. With prolonged UV illumination, pressures below  $10^{-8}$  mbar were achieved.

Exposure of the chamber walls to UV results in absorption of UV light by the water molecules. This increases the molecular vibration energy and results in their ejection from the chamber walls [69].

Additional reduction in the vacuum pressure was possible with an ion-getters pump (SAES Model NEX Torr). The conduction path of the gas molecules to the ion pump was reduced by connecting the ion pump directly to one of the chamber flanges, such that when it was enabled, pressures of  $3 \times 10^{-9}$  mbar were achieved.

## 2.8 Future Experimental Designs

There are several experimental areas that can see improvement in the future. First, the experimenter would benefit from controlled delivery of nanoparticles into the trap. Controlled delivery would include not just automated, vacuum-enclosed particle injection, but also delivery into a trap maintained in UHV. One approach to doing so is by a load-lock arrangement, where a particle is first trapped in a vacuum chamber with pressures ranging from medium-vacuum to atmosphere; then the particle is transferred into a secondary chamber that is always maintained in UHV [70]. An example of this was achieved recently with hollow-core photonic crystal fibers, where a particle is trapped at one end, translated along the fiber, and controllably delivered into an optical cavity on the other end [71].

Second, the experimenter would benefit from improved collection optics. Increasing the collection efficiency of the light scattered from the particle with a higher numerical aperture would increase displacement sensitivity; increasing the Strehl ratio of the optic [72] would reduce the diffraction of the scattered field, thereby enhancing the interferometric contrast; and increasing the measurement precision.

Using a Kalman filter for optimal state estimation would make available custom feedback protocols based on position and velocity [73]. A Kalman filter estimates the state of a system  $X = (x, \dot{x})^T$  based on measurements of its motion. By determining the amplitude of the state vector, or  $E = x^2 + \dot{x}^2$ , one could apply a modulation of the form  $\eta(t) = x\dot{x}/E$ , such that the modulation depth scales inversely with oscillation amplitude. This may help overcome the challenges of weak feedback gain in previous methods using non-linear parametric feedback.

## **2.9 Conclusion**

We have demonstrated that optical levitation of nanoparticles in ultra-high vacuum has necessitated the development of new cooling and tracking technologies along with advanced protocols for pristine vacuum operation.

# 3

---

## Phase Feedback Control

The goal of this chapter is to demonstrate the use of phase-based parametric feedback to overcome broadband detection noise. Phase-sensitive control is used to compress the particle's center of mass temperature from 300 K to sub milli-Kelvins.

### 3.1 Introduction

The work in this thesis is motivated by the push to bring the motion of micro- and nano-scale resonators toward the regime in which their vibrational motion should be quantized. Methods for cooling a mechanical resonator into its quantum ground state have been achieved by cryogenic refrigeration [74] or introducing a damping force into the resonator's dynamics either by cold damping techniques [75–77] or through passive backaction effects [24, 25, 78, 79]. Passive backaction effects occur when the mechanical oscillator forms one end of an optical cavity resonator, as with silica toroids, or is in its circulating mode, as with silicon nitride membranes; tuning the cavity off-resonance by exactly the oscillation frequency ( $\Delta = \Omega_0$ ) results in a retarding back-action on

the mechanical system that automatically modifies its dynamics. Cold damping occurs when a measurement of the oscillator's position is used for real-time correction of the dynamics [77].

Genes, et al., demonstrated that passive back-action effects are optimal when the mechanical resonator is coupled to a very narrow linewidth cavity ( $\kappa < \gamma$ ); however, cold damping is more appropriate in the opposite limit, when using a broadband cavity or free-space optical system [77]. Indeed, feedback cooling has been used in both cavity- and cavity-free opto-mechanical systems [27, 80–84]. First implemented in reducing Brownian fluctuations in vacuum-based electrometers [85], feedback cooling has been used to bring cryogenic micro-mechanical resonators down to the single-phonon regime [86] and has been proposed to enhance sensitivity in nonstationary position measurements [87].

Optical levitation, the subject of this thesis, is a promising platform for quantizing a room-temperature mechanical system. Overcoming dissipation in materials-based devices by physically detaching the resonator from the environment, great strides in optical levitation have been achieved using both cold damping techniques [61, 88] and passive back-action effects in optical cavities [79, 89]. Cavity techniques are limited to cooling the nanoparticle along just one of its motional degrees of freedom; cooling the other axes would require introducing an additional mechanism by which the electro-magnetic field and the mechanical resonator could interact [90].

In the case of optical tweezers, several feedback control methods exist for stabilizing a particle's random, Brownian motion. After Arthur Ashkin first levitated micro-particles in the 1970s [36], he built a vacuum-compatible tweezer [43]. By tracking the levitated particle's motion, Ashkin modulated the intensity with a signal  $v(t) = g\dot{x}$ , proportional to the particle's velocity, which resulted in a time-varying radiation pressure on the particle. A force that is proportional to the velocity is a damping force which slows down the particle. With this system, he brought a levitated microparticle into medium vacuum.

Li, et al, trapped fused silica microparticles in an optical tweezer composed of two counter-propagating laser beams [88]. By overlaying two counter-propagating beams in all three directions - a total of six laser beams - they applied a viscous drag force also of the form  $g\dot{x}$  to cool down the particle into the milli-Kelvin regime.

Reducing experimental complexity by using a high numerical aperture microscope objective with a single laser beam, Gieseler, et al, used parametric feedback to cool a trapped nanoparticle into the sub-Kelvin regime [61]. Parametric feedback uses a time-varying parameter of the system to modify the resonator’s dynamics. Villanueva, et al, first developed the parametric feedback topology for micro-scale devices by weakly modulating the spring constant at twice the resonance frequency to amplify the resonator’s motion [60]. Gieseler, et al, instead applied a non-linear modulation of the form  $x\dot{x}$  to the laser intensity, resulting in a time-varying spring constant, or  $k(t) = k_0(1 + \eta x\dot{x})$ , and creating a non-linear force  $\eta k x^2 \dot{x}$  that damps the particle’s motion with a gain that scales with the square of its oscillation amplitude [91]. At large displacements, the particle is strongly damped but at small displacements it is weakly damped.

With the goal of bringing the trapped nanoparticle to the quantum ground state, the displacement-proportional gain isn’t sufficient because feedback gain shouldn’t weaken as the particle is cooled. Instead, we propose a constant parametric modulation for further cooling of the particle’s motion. To achieve constant modulation and reduce the contribution of measurement noise, we use a phase-locked loop (PLL) to synchronize the feedback phase with the particle’s oscillation [65].

In the next sections, we analyze the particle’s stochastic motion under a phase-locked parametric modulation by following Stratonovich [92]. Thereafter, we outline the experimental implementation and present experimental results to characterize the device’s performance. We compare these results with simulation and use the simulation to understand how noise corrupts the feedback loop.

## 3.2 Theory of Phase-based Control

A PLL consisting of a phase detector, filter, and voltage controlled oscillator is used to track the particle’s oscillation phase, as illustrated in the experimental setup in Fig. 3.1. The VCO output is frequency doubled and amplified before it is used to modulate the laser’s intensity. In contrast to previous modulation techniques [60, 61], the parametric modulation has a constant amplitude. Adjusting

the phase delay between the modulation and the particle oscillation allows us to switch between driving and anti-driving (or damping) of the particle's motion. In this section we analyze parametric modulation in the Langevin formalism and compute the steady-state energy distribution, phase error, and measurement imprecision. We direct the reader to Appendix B for the extended derivation and here just present the main results. We follow a direct protocol for analyzing stochastic processes by Stratonovich [92].

The equation of motion for an underdamped, harmonic oscillator under parametric feedback and the influence of a random thermal force is given by

$$\ddot{x} + \Omega_0^2 x = -\gamma \dot{x} - \Omega_0^2 \zeta(t)x + F_{\text{th}}(t)/m \quad (3.1)$$

where  $\zeta(t) = \zeta_0 \cos(\Omega_m t)$ . Here,  $\zeta_0$  is the fixed amplitude of the drive,  $\Omega_0$  is the center of mass oscillation frequency,  $m$  is the particle's mass, and  $F_{\text{th}}$  is the thermal Langevin force with autocorrelation  $\langle F_{\text{th}}(t)F_{\text{th}}(t') \rangle = 2m\gamma k_B T_0 \delta(t - t')$ . The drive is assumed to be a very weak modulation such that  $\zeta_0 \ll 1$  and its phase has a fixed relationship to the particle oscillation, which is achieved using a phase-locked loop. The modulation phase is  $\Omega_m t = 2\Omega_0 t + 2\theta_m(t) + \theta_0$ , where  $\theta_m(t)$  is the phase of the PLL and  $\theta_0$  is a constant phase offset.

With a weak modulation, the oscillation dynamics are assumed to have minimal change over one oscillation cycle. The particle's motion can be approximated as

$$x(t) = A(t) \cos(\Omega_0 t + \varphi(t)) \quad (3.2)$$

where the amplitude  $A$  and phase  $\varphi$  contain components that are large but slowly varying. Given that the amplitude and the phase vary on timescales that are very slow compared to the oscillation time ( $T_0 = 2\pi/\Omega_0$ ), we approximate the position and velocity using  $\phi(t) = \Omega_0 t + \varphi(t)$  as

$$x = A \cos \phi \quad (3.3a)$$

$$\dot{x} = -A\Omega_0 \sin \phi \quad (3.3b)$$

The phase  $\phi$  varies nearly at a constant rate on timescales comparable to the oscillation such that  $\dot{\phi} \sim \Omega_0$ . Using these values for  $x$  and  $\dot{x}$ , we find that the



amplitude and phase are given by

$$A = \sqrt{x^2 + (\dot{x}/\Omega_0)^2} \quad (3.4a)$$

$$\varphi = -\arctan(\dot{x}/\Omega_0 x) - \Omega_0 t \quad (3.4b)$$

We define the phase error  $\nu = \varphi - \theta_m$ . From Viterbi [65] we have that the phase error varies as

$$\dot{\nu}(t) = \dot{\varphi}(t) - 4B_l \sin(\nu(t)) - \frac{4B_l}{A} n'(t) \quad (3.5)$$

where  $n'(t)$  is the noise due to measurement imprecision. Accordingly, the amplitude  $A$  and phase error  $\nu$  vary as

$$\dot{A} = \underbrace{-\frac{\sin \phi}{\Omega_0} (\gamma A \Omega_0 \sin \phi - A \Omega_0^2 \zeta_0 \cos(\Omega_m t) \cos \phi)}_{h_1} - \underbrace{\frac{\sin \phi}{m \Omega_0} F_{\text{th}}}_{h_2} \quad (3.6a)$$

$$\dot{\nu} = \underbrace{-\cos \phi (\gamma \sin \phi - \Omega_0 \zeta_0 \cos(\Omega_m t) \cos \phi)}_{h_3} - \underbrace{4B_l \sin \nu}_{h_4} - \underbrace{\frac{\cos \phi}{m \Omega_0 A} F_{\text{th}}}_{h_5} - \underbrace{\frac{4B_l}{A} n'}_{h_5} \quad (3.6b)$$

These equations contain deterministic oscillatory terms ( $h_1, h_3$ ) and stochastic terms ( $h_2, h_4, h_5$ ). The noise sources  $F_{\text{th}}$  and  $n'$  are multiplied by  $A$ ,  $\phi$ , or  $\nu$ , which makes them fundamentally different because the amplitude and phase are also randomly varying in time. Using the techniques of stochastic averaging from Stratonovich, we calculate the cycle-averaged amplitude  $\bar{A}$  and phase error  $\bar{\nu}$  under feedback cooling. In doing so, we smoothen out rapid oscillations and can study the long-term, slowly-varying dynamics.

### 3.2.1 A Coupled-Oscillator Model

The cycle-averages evolve according to

$$\dot{\bar{A}} = - \left( \frac{1}{2}\gamma + \frac{1}{4}\zeta_0\Omega_0 \cos(2\bar{\nu}) \right) \bar{A} + \frac{k_B T_0 \gamma}{2m\Omega_0^2} \frac{1}{\bar{A}} + \xi'_F \quad (3.7a)$$

$$\dot{\bar{\nu}} = - \left( -\frac{1}{4}\zeta_0\Omega_0 \sin(2\bar{\nu}) + 4B_l \sin(\bar{\nu}) \right) + \frac{1}{\bar{A}} (\xi_{\text{imp}} + \xi''_F) \quad (3.7b)$$

where  $B_l$  is the PLL's bandwidth and  $\xi$  are random fluctuations that are zero-mean Gaussian noise processes resulting from the thermal force ( $\xi'_F, \xi''_F$ ) and measurement imprecision ( $\xi_{\text{imp}}$ ). It is important to specify that these are independent and uncorrelated noise processes with autocorrelations

$$\langle \xi'_F(t) \xi'_F(t + \tau) \rangle = \frac{\gamma k_B T_0}{m\Omega_0^2} \delta(\tau) = \langle \xi''_F(t) \xi''_F(t + \tau) \rangle \quad (3.8a)$$

$$\langle \xi'_F(t) \xi''_F(t + \tau) \rangle = 0 \quad (3.8b)$$

$$\langle \xi_{\text{imp}}(t) \xi_{\text{imp}}(t + \tau) \rangle = 8B_l^2 S_{\text{imp}} \delta(\tau) \quad (3.8c)$$

Similarly,  $\xi_{\text{imp}}$  is uncorrelated from  $\xi'_F$  and  $\xi''_F$ , or

$$\langle \xi_{\text{imp}}(t) \xi'_F(t + \tau) \rangle = 0 = \langle \xi_{\text{imp}}(t) \xi''_F(t + \tau) \rangle \quad (3.9)$$

What we have done here is reduce the equation of motion in  $x(t)$  that is driven by a zero-mean random force  $F_{\text{th}}$  into two coupled equations for  $\bar{A}$  and  $\bar{\nu}$  for the cycle-averaged, or smoothed out, form of amplitude and phase error. In doing so, we have written their dynamics in the form of Langevin equations that are driven by white noise.

With the stochastic equation in the Langevin form, we can try to find a stationary distribution of the system through which we could calculate a steady-state of the amplitude and phase. Before we proceed to calculate probability distributions, we will first analyze these coupled equations.

We refer to this model as a coupled oscillator system because we have connected the particle's harmonic oscillation ( $x(t)$ ) to the PLL's time-varying phase ( $\theta_m(t)$ ), which is described by the swing of a massless pendulum.

The amplitude equation consists of three sets of terms: proportional to  $\bar{A}$ , to

$1/\bar{A}$ , and random  $\xi'_F$ . If we take an average of this equation over noise histories, then we find when the phase error is small

$$\langle \dot{\bar{A}} \rangle = - \left( \frac{1}{2}\gamma + \frac{1}{4}\zeta_0\Omega_0 \right) \langle \bar{A} \rangle + \frac{k_B T_0 \gamma}{2m\Omega_0^2} \frac{1}{\langle \bar{A} \rangle} \quad (3.10)$$

The simplification of  $\langle 1/\bar{A} \rangle$  to  $1/\langle \bar{A} \rangle$  is valid in the limit of large amplitude  $\langle \bar{A} \rangle$  and small fluctuations about the mean\*.

The steady-state of this system would occur when  $\langle \dot{\bar{A}} \rangle = 0$ , whose solution is

$$\langle \bar{A} \rangle^2 = \frac{k_B T_0}{m\Omega_0^2} \frac{\frac{1}{2}\gamma}{\frac{1}{2}\gamma + \frac{1}{4}\zeta_0\Omega_0} \quad (3.11)$$

This expression is none other than the fluctuation-dissipation theorem. It tells us that dissipation from gas damping and feedback cause the amplitude to decay and fluctuations from the bath of air molecules cause it to rise. The balance of the two results in an effective temperature under feedback given by

$$T_{fb} = T_0 \frac{\gamma}{\gamma + \frac{1}{2}\zeta_0\Omega_0} \quad (3.12)$$

Next, we analyze the phase error variation. When the phase error is small and the oscillation amplitude is very large, the phase error decays as

$$\dot{\bar{\nu}} = - \left( -\frac{1}{2}\zeta_0\Omega_0 + 4B_l \right) \bar{\nu} \quad (3.13)$$

whose solution is

$$\bar{\nu} = \nu_o \exp \left[ - \left( -\frac{1}{2}\zeta_0\Omega_0 + 4B_l \right) t \right] \quad (3.14)$$

---

\*Explicitly seen with a Taylor expansion, or

$$\begin{aligned} \left\langle \frac{1}{\bar{A}} \right\rangle &= \frac{1}{\langle \bar{A} \rangle} - \frac{1}{\langle \bar{A} \rangle^2} \langle \bar{A} - \langle \bar{A} \rangle \rangle + \frac{1}{\langle \bar{A} \rangle^3} \langle (\bar{A} - \langle \bar{A} \rangle)^2 \rangle + \dots \\ &= \frac{1}{\langle \bar{A} \rangle} + \frac{\langle \bar{A}^2 \rangle - \langle \bar{A} \rangle^2}{\langle \bar{A} \rangle^3} + \dots \end{aligned}$$

This tells us that the phase error from the PLL tracking the particle's oscillation phase will decay exponentially and, in the limit of  $t \rightarrow \infty$ , decays to zero. There is, however, also an insight on the bandwidth needed to track the oscillation phase, namely

$$\zeta_0 < 8B_l/\Omega_0 \quad (3.15)$$

This limit tells us that the bandwidth needed to maintain lock should be increased with feedback gain. There is an intuitive explanation for this, namely that under feedback the linewidth is broadened; if it is broadened beyond the tracking bandwidth, the PLL will no longer accurately follow the particle's motion and lose lock.

The form of the phase error in Eq. 3.7b matches that of the motion of a massless string pendulum. Thermal fluctuations and measurement imprecision drive the pendulum into motion. When the oscillation amplitude is very small (limit of  $A \rightarrow 0$ ) these random forces would push the pendulum around by more than half a revolution, which is when the PLL loses lock. The average time for this to occur is related to the signal to noise ratio of the detected oscillation [65].

#### 3.2.2 Fokker-Planck Equation

Recognizing that Eqs. 3.7 are in the form of Langevin equations, we can derive the Fokker-Planck equation for the joint probability distribution of  $\bar{A}$  and  $\bar{\nu}$ , or  $P(\bar{A}, \bar{\nu}, t)$ . Following the prescription in Appendix C, we find the FP equation is given by [93]

$$\begin{aligned} \frac{\partial P}{\partial t} = & -\frac{\partial}{\partial \bar{A}} \{\alpha_1 P\} - \frac{\partial}{\partial \bar{\nu}} \{\alpha_2 P\} + \frac{\partial^2}{\partial \bar{A}^2} \{D_{11} B_{11} B_{11} P\} \\ & + \frac{\partial^2}{\partial \bar{\nu}^2} \{(D_{21} B_{21} B_{21} + D_{22} B_{22} B_{22}) P\} \end{aligned} \quad (3.16)$$

The coefficients are derived from the coupled Langevin equations and the characteristics of the noise. Those coefficients  $\alpha_i$  are the drift terms and  $B_{ij}$  are the diffusion terms with corresponding diffusion coefficients  $D_{ij}$ . Together they describe how the probability of a system attaining a specific configuration

evolves over time, and are given by

$$\alpha_1 = \left( -\frac{1}{2}\gamma - \frac{1}{4}\zeta_0\Omega_0 \cos(2\bar{\nu}) \right) \bar{A} + \frac{k_B T_0 \gamma}{2m\Omega_0^2} \frac{1}{\bar{A}} \quad (3.17a)$$

$$\alpha_2 = - \left( -\frac{1}{4}\zeta_0\Omega_0 \sin(2\bar{\nu}) + 4B_L \sin(\bar{\nu}) \right) \quad (3.17b)$$

$$B_{11} = 1 \quad (3.17c)$$

$$B_{21} = 1/\bar{A} = B_{22} \quad (3.17d)$$

$$D_{11} = k_B T_0 \gamma / m\Omega_0^2 = D_{21} \quad (3.17e)$$

$$D_{22} = 8S_{\text{imp}} B_L^2 \quad (3.17f)$$

Eq. 3.16 describes how the probability density evolves in time and is typically solved numerically with a given set of initial conditions  $(A_0, \nu_0)$ . As we are only interested in steady-state dynamics, we will study this equation analytically in limiting cases and later numerically for the configuration of our system.

### 3.2.3 Amplitude and Energy Distribution

Assume that the probability distribution reaches a steady-state. Then, it will have no time variation, or  $\lim_{t \rightarrow \infty} \frac{\partial P}{\partial t} = 0$ . Next, we will approach solving this equation in two different limits. First, we take the phase error to be negligible such that  $\sin(\bar{\nu}) \sim \bar{\nu} \sim 0$ . When the feedback gain and the measurement imprecision are small, the amplitude is large. Then, Eq. 3.16 simplifies to

$$\frac{\partial P}{\partial t} = -\frac{\partial}{\partial \bar{A}} \{ \alpha_1 P \} + \frac{\partial^2}{\partial \bar{A}^2} \{ D_{11} B_{11} B_{11} P \} \quad (3.18)$$

Accounting for the fact that the probability density is vanishing when the amplitude tends to infinity, we can write that the stationary probability density  $P(\bar{A})$  is a solution of

$$0 = \frac{d}{d\bar{A}} \left\{ \alpha_1 P - \frac{d}{d\bar{A}} (D_{11} B_{11} B_{11} P) \right\} \quad (3.19)$$

An analytical solution to this equation exists and is given by

$$P(\bar{A}) = \frac{\bar{A}}{Z_{\bar{A}}} \exp \left[ -\frac{m\Omega_0^2}{2k_B T_0} \left( 1 + \frac{1}{2} \frac{\zeta_0 \Omega_0}{\gamma} \right) \bar{A}^2 \right] \quad (3.20)$$

In the limit of  $\gamma \rightarrow 0$ , the argument of the exponential in Eq. 3.20 diverges to negative infinity, which means the probability distribution decays to 0. This tells us that the feedback perfectly damps the amplitude when there is no dissipation, which is what one expects for the damped classical harmonic oscillator. The constant  $Z_{\bar{A}}$  is a normalization constant given by

$$Z_{\bar{A}} = \frac{k_B T_0}{m\Omega_0^2} \frac{2\gamma}{2\gamma + \zeta_0 \Omega_0} \quad (3.21)$$

It ensures that the probability distribution integrates to 1, or  $\int_0^\infty d\bar{A} P(\bar{A}) = 1$ . Given that the energy  $E \sim \bar{A}^2$ , we determine the energy probability distribution using  $P(\bar{A})d\bar{A} = P(E)dE/2\bar{A}$ , which is

$$P(E) = \frac{1}{Z_E} \exp \left[ -\beta \left( 1 + \frac{\zeta_0 \Omega_0}{2\gamma} \right) E \right] \quad (3.22)$$

Here,  $\beta = 1/k_B T_0$  and the normalization constant  $Z_E$  is given by

$$Z_E = \frac{2\gamma}{2\gamma + \zeta_0 \Omega_0} k_B T_0 \quad (3.23)$$

The energy distribution given in Eq. 3.22 is in the form of a Maxwell-Boltzmann distribution, which is the characteristic signature of a system at thermal equilibrium. Thus, phase-sensitive feedback increases the effective friction that the particle experiences and reduces the center of mass fluctuations by coupling it to a bath with effective temperature  $Z_E$ . The modulation creates a driven system that resembles a thermal system.

#### 3.2.4 Phase Error and Measurement Imprecision

Next we study what happens in the phase domain. First, we select an arbitrary amplitude  $\bar{A} = A_0$  that is large and solve the phase Fokker-Planck equation for the conditional probability distribution  $P_{A_0}(\nu, t) = P(A_0, \nu, t)$ . When the

feedback gain is very weak, the amplitude varies on a longer timescale than the phase tracker because  $\gamma \ll 4B_L$ , which allows us to assume a nearly constant amplitude.  $P_{A_0}$  is given by

$$\frac{\partial P_{A_0}}{\partial t} = -\frac{\partial}{\partial \bar{\nu}} \{ \alpha_2 P_{A_0} \} + \frac{\partial^2}{\partial \bar{\nu}^2} \left\{ (D_{21} + D_{22}) \frac{1}{A_0^2} P_{A_0} \right\} \quad (3.24)$$

$P_{A_0}(\bar{\nu}, t)$  describes the conditional distribution for  $\bar{\nu}$ . It must be periodic in  $\bar{\nu}$  with boundary conditions  $P_{A_0}(\pi, t) = P_{A_0}(-\pi, t)$ . Assume a steady-state such that  $\lim_{t \rightarrow \infty} \frac{\partial P_{A_0}}{\partial t} = 0$ . Then, Eq. 3.24 reduces to

$$0 = \frac{d}{d\bar{\nu}} \left[ -\alpha_2 P_{A_0} + \frac{1}{A_0^2} \left( 8B_l^2 S_{\text{imp}} + \frac{\gamma k_B T_0}{m\Omega_0^2} \right) \frac{dP_{A_0}}{d\bar{\nu}} \right] \quad (3.25)$$

We assume that the phase error is small such that  $\sin 2\bar{\nu} \sim 2 \sin \bar{\nu}$ . Integrating with respect to  $\nu$ , we obtain a first-order linear differential equation which is solved as

$$P_{A_0}(\bar{\nu}) = \exp[\alpha_s \cos \bar{\nu}] / (2\pi I_0[\alpha_s]) \quad : \quad -\pi \leq \bar{\nu} \leq \pi \quad (3.26)$$

where  $\alpha_s$  is related to the signal to noise ratio on the detector, and, using  $\bar{n}_{\text{imp}} = S_{\text{imp}} B_l$  and  $\bar{n}_{\text{fb}} = (k_B T_0 / m\Omega_0^2) \gamma / (\gamma + \frac{1}{2} \zeta_0 \Omega_0)$ , is given by

$$\alpha_s = \frac{4B_l - \frac{1}{2} \zeta_0 \Omega_0}{8B_l (\bar{n}_{\text{imp}} / \bar{n}_{\text{fb}}) + (\gamma + \frac{1}{2} \zeta_0 \Omega_0)} \quad (3.27)$$

When the feedback is off and  $\gamma \ll B_l$ ,  $\alpha_s$  reduces to the detected signal to noise ratio, or

$$\alpha_s^{(0)} = \frac{\bar{n}_{\text{th}}}{2\bar{n}_{\text{imp}}} \quad (3.28)$$

for  $\bar{n}_{\text{th}} = k_B T_0 / \hbar \Omega_0$ .  $I_n(z)$  is the modified Bessel function of the first kind. We expand the probability distribution in a Fourier series as

$$P_{A_0}(\bar{\nu}) = \frac{1}{2\pi I_0[\alpha_s]} \left( I_0[\alpha_s] + 2 \sum_{n=1}^{\infty} I_n[\alpha_s] \cos(n\bar{\nu}) \right) \quad (3.29)$$

Next, we calculate the mean and the mean square of the steady-state phase error, which is given by [65]

$$\langle \bar{\nu} \rangle = \int_{-\pi}^{\pi} d\bar{\nu} \bar{\nu} P_{A_0}(\bar{\nu}) = 0 \quad (3.30a)$$

$$\langle \bar{\nu}^2 \rangle = \int_{-\pi}^{\pi} d\bar{\nu} \bar{\nu}^2 P_{A_0}(\bar{\nu}) = \frac{\pi^2}{3} + 4 \sum_{n=1}^{\infty} \frac{(-1)^n I_n[\alpha_s]}{n^2 I_0[\alpha_s]} \quad (3.30b)$$

From Eqs. 3.30, we see that the phase error is a zero-mean process whose variance  $\sigma_{\bar{\nu}}^2$  approaches  $\pi^2/3$  in the limit of  $\alpha_s$  goes to zero, which is the variance of a random variable that is uniformly distributed from  $-\pi$  to  $+\pi$ .

### 3.3 Experimental Results

In this section, we present experimental results for PLL-based feedback cooling: linear dependence of the temperature on pressure, equilibrium energy distribution, and cooling to milli-Kelvin temperatures.

Sketched in Fig. 3.1a is the experimental setup. A focused laser beam is used to trap a particle inside of a vacuum chamber. The particle's scattered light is collimated using an asphere and then redirected to three balanced photodetectors in a split configuration, illustrated as a quadrant photodetector. The output of each photodetector is connected to a PLL. The PLL is used to track the oscillation frequency and phase and its output is frequency doubled. Internally, one can set the amplitude gain of the feedback signal and sum together the feedback for all three axes. This signal is then connected to a high-voltage amplifier that modulates the EOM's output intensity and generates a parametric modulation of the trap.

To calibrate the conversion of detector voltage to displacement, first a series of oscillation traces of minimum length  $t_{\text{meas}} = 2\pi/\gamma$  are captured with no feedback cooling applied at  $P_{\text{gas}} = 13.6$  mbar. Seen in Fig. 3.1b is the characteristic harmonic oscillation. A histogram of the trace is computed, as in Fig. 3.1c, to verify that the system has reached a state of equilibrium in the duration of the measurement. Finally, a composite power spectral density is calculated. As shown in Fig. 3.1d, the calculated single-sided spectrum is



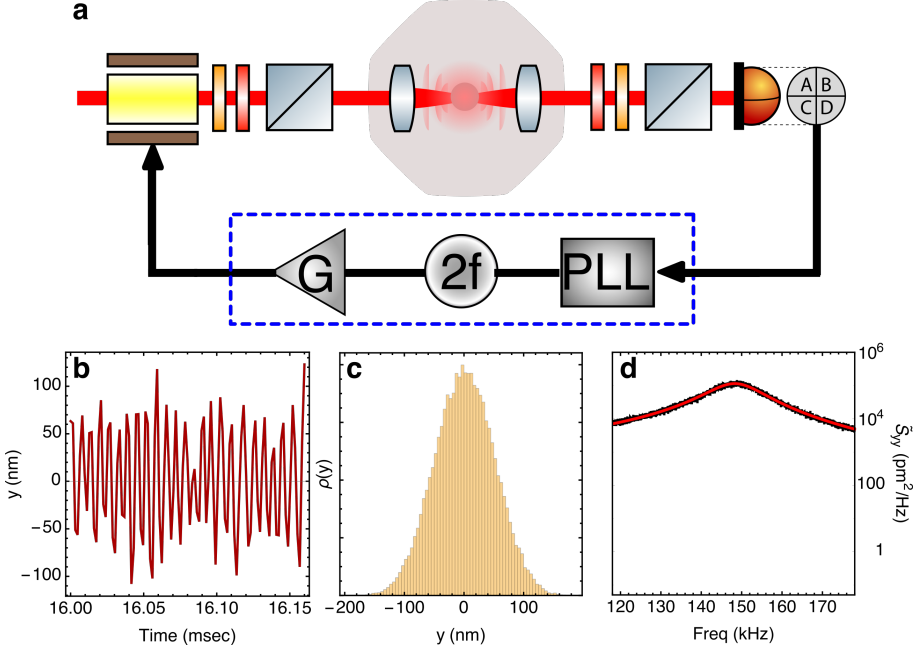


**Figure 3.1: Parametric feedback loop** (a) An illustration of the parametric feedback loop involving a phase-locked loop (PLL). The output of a laser is guided through an electro-optic modulator (EOM) and into a vacuum chamber. Inside this chamber a particle is trapped using a focused laser beam. The forward scattered light is captured on a split photodetector and connected to a PLL. The PLL tracks the oscillation phase, doubles the frequency, and outputs the oscillation with a fixed amplitude  $G$ . The oscillation is connected to the EOM to generate a small modulation of the trapping intensity. (b) A short time trace of the oscillation in  $y$  without feedback at  $P_{\text{gas}} = 13.6$  mbar showing the characteristic harmonic oscillation resulting from thermal fluctuations. (c) A histogram of the fluctuations in position over 100 msec at the same pressure. The Gaussian bell-shape indicates that the statistics of the trace represent a thermal distribution. (d) A power spectral density (in  $\text{pm}^2/\text{Hz}$ ) of the motion in  $y$  at the same pressure and overlaid a fit to a Lorentzian, as in Eq. 3.31.

plotted in black and overlaid is a fit to a Lorentzian of the form

$$\begin{aligned}
 S_y[\Omega] &= \frac{1}{2\pi} \int_{-\infty}^{\infty} \langle y(t)y(t-t') \rangle e^{-i\Omega t'} dt' & (3.31) \\
 &= \frac{k_B T_0}{\pi m} \frac{\gamma}{(\Omega_y^2 - \Omega)^2 + \gamma^2 \Omega^2} + S_{\text{imp}} & 49
 \end{aligned}$$

Extracted from the fit are the center frequency  $\Omega_y$ , the peak displacement  $S_y[\Omega_y]$ , and the linewidth  $\gamma$ . At a later time, the particle is ejected from the trap and the remaining detector noise floor is used to obtain the measurement imprecision  $S_{\text{imp}}$ .

### 3.3.1 Pressure dependence

The particle experiences a restoring force from the optical potential with stiffness  $k$  in the each axis of motion. As it is kicked around by air molecules, the particle displaces part of the residual gas, which creates a frictional force in the form of drag to a sphere, or  $F_{\text{drag}} = -m\gamma\dot{x}$ , where  $\gamma$  is

$$\gamma = \frac{6\pi\eta R}{m} \frac{0.619}{0.619 + \text{Kn}} (1 + c_K) \quad (3.32)$$

Here,  $c_K = 0.31\text{Kn}/(0.785 + 1.152\text{Kn} + \text{Kn}^2)$ ,  $\eta$  is the viscosity of air, and  $\text{Kn} = \bar{v}/a$  is the Knudsen number [88, 94]. We approximate this as  $\gamma = 15.8 R^2 P_{\text{gas}}/mv_{\text{gas}}$  where  $v_{\text{gas}} = \sqrt{3k_B T_0/m_{\text{gas}}}$  is the rms velocity of the gas molecules. The correction to the drag coefficient obtained by the Stokes' law is the result of the high surface area to volume aspect ratio for a nanosphere.

A particle measuring  $R = 50$  nm is trapped and then brought into medium vacuum using constant feedback gain. At two different vacuum pressures with fixed gain, we plot the power spectral densities for motion in  $y$  in Fig. 3.2a. Overlaid on the spectra are fits of a Lorentzian with negligible residual error from the Lorentzian model. The measurement imprecision is  $S_{\text{imp}} = 0.3 \text{ pm}^2/\text{Hz}$ .

Next, for fixed values of gain we track the center-of-mass temperature under feedback as a function of pressure in  $y$ . Plotted in Fig. 3.2b is the response at two specific gain settings. The temperature is obtained by integrating the spectra, which gives  $\langle y^2 \rangle = k_B T_0/m\Omega_0^2$ . The vacuum pressure is manually locked to a specific setting, several time traces are collected, and the center of mass temperature is computed. The temperature versus pressure graph is fit with a power law of the form  $T[P_{\text{gas}}] = a(P_{\text{gas}})^b$  in the range of  $5 \times 10^{-6}$  to  $5 \times 10^{-4}$  mbar and returns an exponent of  $b = 0.94 \pm 0.02$ . The exponent with a near unity value confirms that this feedback scheme is more efficient in cooling as a function of damping than previous schemes in which temperature

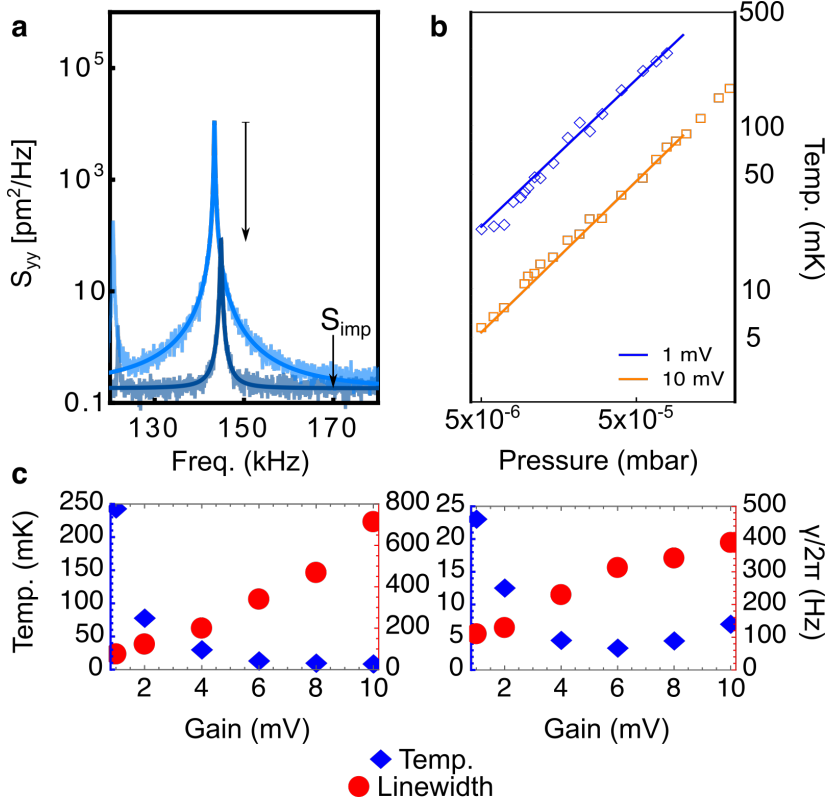


**Figure 3.2: Feedback cooling performance in  $y$ .** (a) Power spectral densities of the motion in  $y$  at  $P_{\text{gas}}^{(1)} = 6.6 \times 10^{-4}$  mbar and  $P_{\text{gas}}^{(2)} = 1.0 \times 10^{-5}$  mbar for the same feedback gain. The spectra are plotted with Lorentzian fits overlaid. (b) The center of mass temperature in  $y$  as a function of pressure at two gain settings of 1 mV and 10 mV. Lines of fit to illustrate the trend are overlaid. (c) Plots of temperature and linewidth versus gain at  $P_{\text{gas}} = 2 \times 10^{-6}$  mbar (left) and  $P_{\text{gas}} = 2 \times 10^{-7}$  mbar (right).

varied with the square root of pressure ( $T \propto \sqrt{\gamma}$ ) [61, 91].

Next, the gain is swept while holding vacuum pressure constant. In Fig. 3.2c, the temperature at  $P_{\text{gas}}^{(1)} = 2.0 \times 10^{-6}$  mbar decreases as the feedback gain is increased while the linewidth of the response increases. At a lower pressure of  $P_{\text{gas}}^{(2)} = 2.0 \times 10^{-7}$  mbar, the temperature first decreases with increasing gain and later, above  $G = 6$  mV, increases while the linewidth monotonically

increases.

Decreasing vacuum pressure reduces the heating from the residual gas and, as a result, cooler temperatures are achieved for a fixed feedback gain. At lower pressures, the feedback cools the detected motion closer to the noise, such that as pressure is reduced, the temperature-minimizing gain  $\zeta_{\min}$  is also lower. The oscillator's linewidth, however, is increased to  $\gamma_{\min}/2\pi = 282.3 \pm 78.0$  Hz when the temperature is minimized.

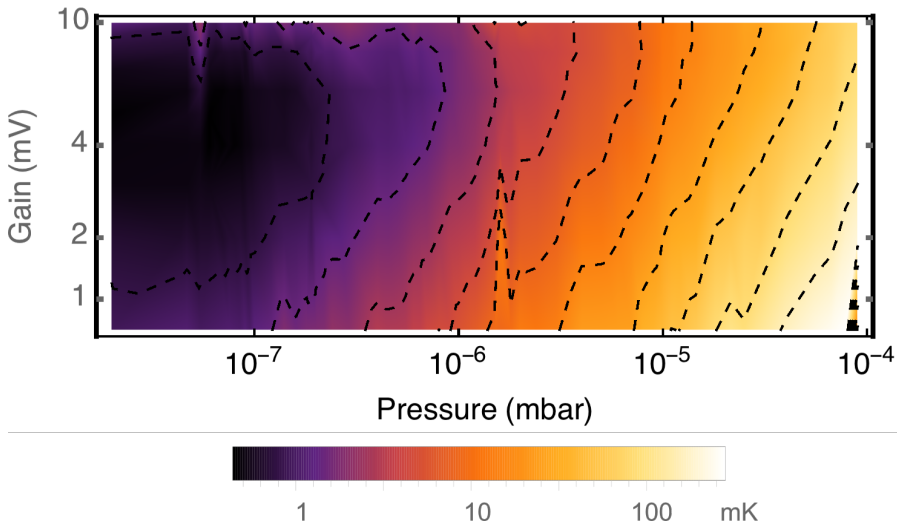


**Figure 3.3: Temperature as a function of gain and pressure.** A density plot of the center of mass temperature in  $y$  as a function of both the gain and pressure. The density plot is the result of over 400 combination of gains and pressures. In each configuration, the temperature is determined from twenty time traces measuring 100 msec in length. The temperature is scaled logarithmically and shown on the map are ten isotherms.

Combining the three variables of gain, pressure, and temperature, we plot a density map of the measured temperature in  $y$  in Fig. 3.3. In this map, we see isotherms, or lines of constant temperature, as dashed lines. A darker color corresponds to a colder temperature and a brighter color to a warmer temperature. Following one of the isotherms, the temperature at a pressure of

$3 \times 10^{-6}$  mbar under weak feedback gain corresponds to the same temperature at a pressure of  $2 \times 10^{-5}$  mbar under strong feedback gain. The measurement imprecision is constant at all points in the map. At pressures below  $10^{-6}$  mbar, increasing the feedback gain does not monotonically reduce the temperature, notably visible in the black region of the map. At lower pressures, the tuning range for cooling the motion is reduced.

#### 3.3.2 Energy Distribution under Feedback

Although we compute the center-of-mass temperature from the mean-squared displacement, we also want to see how, if at all, the energy distribution is modified by feedback control.

The energy distribution is calculated from time traces of the particle's motion. The variance of a few oscillation cycles is computed on a timescale smaller than the relaxation time, or  $t_E < 2\pi/\gamma$ . A histogram is computed from a set of energies based on several time traces, such that the variance of the total data set is minimized. The histogram is normalized to generate the energy probability distribution function,  $\rho(E)$ , which is defined as  $\int_0^\infty dE \rho(E) = 1$ . Here, the energy distribution is calculated for a fixed feedback gain at three different vacuum pressures. The energy distribution under feedback is shown in Fig. 3.4.

The energy is normalized to the energy at room temperature. Overlaid on the probability distribution is a fit to the Maxwell-Boltzmann distribution for a system at thermal equilibrium. Reducing the pressure confines the energy distribution to a narrower range of energies. Divergence from the trend at either energies greater than  $1.5 \times 10^{-4} k_B T_0$  is the result of rare events that are not sampled enough in the data acquisition. At energies below  $0.2 \times 10^{-4} k_B T_0$ , detection noise masks the particle motion, which makes it very unlikely that we would measure zero energy. From the distribution in Eq. 3.22, however, zero energy is the most likely.

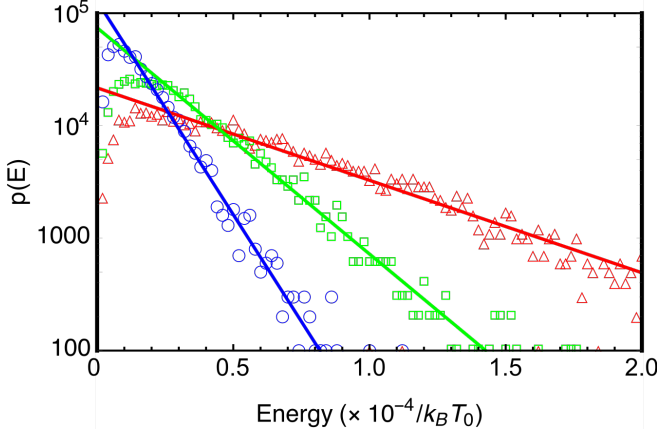


**Figure 3.4: Energy distribution under feedback.** The measured energy probability distribution function under feedback is plotted for three different pressures, at  $2 \times 10^{-7}$  (blue),  $2 \times 10^{-6}$  (green), and  $2 \times 10^{-4}$  (red) mbar. The energy is normalized by the mean energy obtained at  $P_{\text{gas}} = 13.6$  mbar with no feedback, corresponding to  $E = k_B T_0$ . Overlaid to the energy distributions are fits to the Maxwell-Boltzmann distribution to illustrate the trend.

### 3.4 Measurement Imprecision in a Parametric Feedback Loop

The rise in temperature for strong gains in Fig. 3.2c that is emphasized by the black region of Fig. 3.3 indicates that the feedback loop can still be optimized. The particle's center of mass temperature, which is in the sub-milli-Kelvin regime in the black area of Fig. 3.3, is still far from the ground state.

Since an analytical solution to the derived FP Equation is unknown, a numerical simulation of the coupled system in Eqs. 3.7 was carried out in Matlab *Simulink*. All noise sources were set as bandwidth-limited and were seeded with different random numbers. The initial position and velocity were randomly chosen from a distribution with mean temperature  $T = 1$  K. The stochastic equations (Eqs. 3.7) were solved for a  $R = 50$  nm particle with center frequency  $\Omega_y = 2\pi 150$  kHz; thermal Langevin force was derived from a room temperature bath at  $k_B T_0$ . The feedback gain  $\zeta_0$ , gas damping  $\gamma$ , and

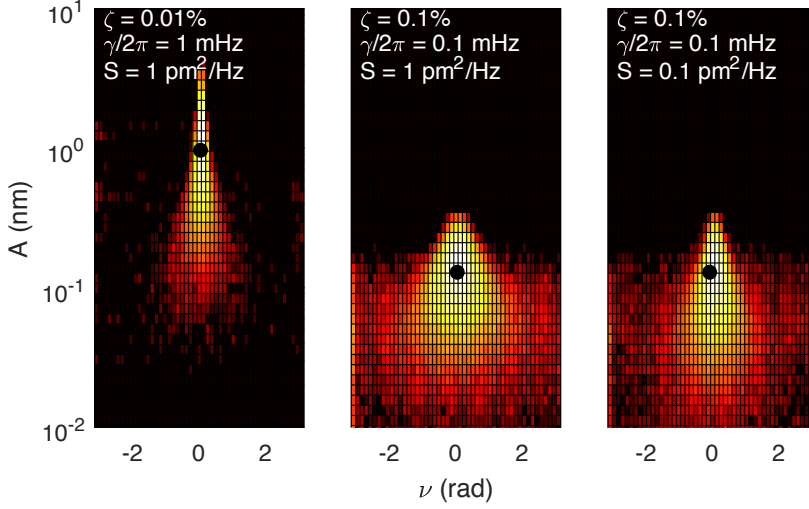


**Figure 3.5: Measurement imprecision in a PLL.** Numerical solutions to the coupled oscillator system of Eqs. 3.7 for three different experimental configurations. The solution was computed in Matlab *Simulink* using a fourth-order Runge-Kutta solver with a step size of  $10^{-4}$  sec and a simulation time of 10 sec. These are density plots of the amplitude and phase distribution; the black dot indicates the peak position.

measurement imprecision  $S_{\text{imp}}$  were separately changed. The results of each numerical integration are plotted in Fig. 3.5.

Both increasing the feedback gain and reducing the gas damping by an order of magnitude attenuated the amplitude fluctuations by an order of magnitude, as seen in the transition from Fig. 3.5a to 3.5b. The plots illustrate the logarithmic phase space density for amplitude and phase, with bright yellow corresponding to very likely and dark red as less likely. They are calculated from histograms of the numerical solutions obtained with *Simulink*. In Fig. 3.5b we see that the phase error distribution is broad and exceeds the bounds of  $\pm\pi/2$  one would require to cool the motion. Reducing the measurement imprecision in Fig. 3.5c, the phase distribution is narrower and largely confined to within  $\pm\pi/2$ .

As the imprecision is lowered, the center of mass temperature also reduces. In these simulations, the temperature dropped from  $800 \mu\text{K}$  (in b) to  $690 \mu\text{K}$  (in

c). Better sensitivity to the particle's oscillation reduces the phase tracking error in the PLL and results in more efficient feedback cooling. As the imprecision is reduced, the maximum feedback gain increases, allowing further cooling of the motion. When the feedback gain is too high, the phase uncertainty – the pendular phase rotation – kicks back on the amplitude and heats it up.

Comparing the parameters in Fig. 3.2c, at pressures of  $P_{\text{gas}} = 10^{-7}$  mbar, where  $\gamma/2\pi = 0.3$  mHz, and  $S_{\text{imp}} = 0.3$  pm<sup>2</sup>/Hz, we find the mean of  $P(A, \nu)$  occurs at  $A = 0.1$  nm, which corresponds to  $T_{fb} = 0.7$  mK. This is in quantitative agreement with experimentally measured values. According to the simulation, if we reduce the damping to  $\gamma/2\pi = 0.01$  mHz and the imprecision noise to  $S_{\text{imp}} = 0.1$  pm<sup>2</sup>/Hz, we can raise the feedback gain and reach temperatures in the range of 100  $\mu$ K.

Using this technique to cool the particle's motion further toward the ground state will require improvements in the imprecision noise  $\bar{n}_{\text{imp}}$  and a PLL with a slightly larger bandwidth  $B_L$ . Reducing the dissipation  $\gamma$  will bring the motion to colder temperatures under the same level of gain.

## 3.5 Conclusion

We have demonstrated a new parametric feedback control method that is based on the mechanical oscillator's time-varying phase. Using a phase-locked loop, we track the particle's oscillation phase and feed that information back onto the particle in order to cool it down. The PLL's phase estimates are based on the particle's time-varying position.

With this new method, we cool the particle's motion more efficiently and reduce its center of mass temperature by more than two orders of magnitude to the sub-milli-Kelvin regime, as compared with previous methods. Despite the center of mass temperature being dramatically different from the environment's, the oscillator appears to be in a state of thermal equilibrium.

Having developed a coupled-oscillator model of the particle's slowly varying amplitude and its phase, we conclude that the two variables to target are the intrinsic damping  $\gamma$  and the measurement imprecision  $S_{\text{imp}}$ . Reducing  $\gamma$  will reduce the reheating that the particle experiences, allowing the feedback to further suppress its motion. Improving the measurement precision will enable a



more precise phase estimate by the PLL with which stronger feedback gains can be applied. This will bring the center of mass motion further toward the ground state.



# 4

---

## Photon Recoil Heating

The goal of this chapter is to quantify the role of photon recoil heating and how it limits steady-state feedback cooling in ultra-high vacuum. The findings in this chapter were part of a paper published in *Physical Review Letters* (2016) [95].

### 4.1 Introduction

Our capacity for reducing the center of mass motion to the ground state is a compromise between the cooling rate from the feedback and the heating rate from various dissipation mechanisms. In the previous chapter, we showed that phase-based feedback cooling is more efficient than existing techniques because it cools at a rate linear in damping. Reducing vacuum pressure attenuates the reheating rate from collisions with the residual gas molecules.

In this chapter, we explore the ultra-high vacuum domain of pressure and the influence of optical effects on the levitated particle. We challenge the assumption that dissipation decreases with vacuum pressure as noise from the laser field may also drive the particle's motion.

In an optical position sensor, one irradiates an object with light and detects the scattered photons. As each photon carries momentum  $p = \hbar k$ , where  $k$

is the photon wave vector, we can increase the optical power to reduce the object's position uncertainty to  $\Delta x \geq 1/(2k\sqrt{N})$ , where  $N$  is the number of scattered photons. Increasing the optical power, however, increases the rate of momentum kicks from individual photons and results in a force due to radiation pressure shot noise (RPSN), which perturbs the inspected object. While increasing power reduces our measurement imprecision, RPSN places limits on the information gained from a system [15, 96].

Remarkable advances in micro-fabrication have resulted in high-Q cavity opto-mechanical resonators that are sensitive to RPSN in optical measurements. In addition to ground state cooling [24, 25], recent experiments in cryogenic chambers with silicon nitride membranes, cold-atomic clouds, and microwave devices have verified the influence of RPSN in continuous position and force measurements [16, 97, 98]. Increasing the circulating optical power in the cavity increases the back-action on the resonator, which is manifested as an increase in the oscillator's mean-square displacement. The motion of a cavity-coupled silicon nitride membrane was shown to thermalize with the shot-noise fluctuations of the laser field; cavity-optical cooling brought its motion to the limit imposed by quantum back-action from the field [99].

Parallel efforts with feedback-based control exist to achieve the quantum ground-state of motion in both cryogenic and room-temperature systems. Feedback cooling at or above the thermal decoherence rate was shown to bring the motion of a cryogenically-cooled silicon nitride string close to the ground-state [86]. In these experiments photo-thermal heating from absorption in the material limited cooling the mechanical object further. Here, we demonstrate that an optically levitated nanoparticle in ultra-high vacuum at room temperature is not affected by thermal effects but by measurement back action from the laser field. We use feedback cooling to counter it.

Optically levitated nanoparticles in vacuum have proven to be versatile platforms for studies of light-matter interactions [35, 36, 61, 79, 89, 100]. Free from mechanical vibrations of the environment, they have been used to investigate nonequilibrium fluctuation theorems [91] and ultras-small forces [100, 101]. In the context of cavity optomechanics, levitated nanoparticles have also been proposed for quantum ground state cooling [40, 79, 89, 102] and for gravitational wave detection [103, 104]. Central to all of these experiments is

the optical gradient force, which is needed to trap and control the scrutinized nanoparticle. However, due to the discrete nature of optical radiation, the trapping force is itself intrinsically noisy and RPSN may influence the motion of the trapped particle via photon recoil heating.

At first blush, one would expect that photon recoil heating is negligibly small for macroscopic objects, as the recoil energy  $E_R = \hbar^2 k^2 / (2m)$  scales inversely with the object's mass. For a levitated nanoparticle, the recoil energy is  $6.7 \times 10^{-38}$  J, or nearly nine orders of magnitude smaller than atomic recoil energies [105, 106]. To observe this weak effect, the system has to be sufficiently well isolated. In particular, the photon recoil rate has to be larger than the thermal dissipation rate.

Using active feedback to bring a nanoparticle into ultra high vacuum (UHV) ( $P_{\text{gas}} \sim 10^{-8}$  mbar), however, we significantly reduce the heating due to residual gas molecules and thereby ascertain for the first time a direct readout of the recoiling rate of photons from a macroscopic object at room temperature, thereby entering the regime of strong measurement backaction [98].

In the following sections, we will derive the force on a levitated particle due to photon scattering by a semi-classical approach. Then, we derive a Fokker-Planck equation for the steady-state energy distribution under recoil heating and the corresponding reheating rates. Thereafter, we provide experimental data both with and without feedback cooling and compare to theoretical estimates. Finally, we derive the standard quantum limit for a continuous measurement in an optical tweezer trap to identify where reheating can be further reduced.

## 4.2 Photon Recoil Heating

Here, we derive the force on a polarizable particle due to photon scattering based on a fluctuating classical force picture from Itano & Wineland [107]. This semi-classical approach agrees with a derivation by Rodenburg, et al., using the quantum master equation formalism [108].

We begin with a particle in a harmonic potential  $U(x) = \frac{1}{2}m\Omega_0^2 x^2$  driven by a fluctuating force,  $F(t)$ , arising from the fluctuating photon numbers in the trapping field. The interaction is illustrated in Fig. 4.1. The equation of motion

is

$$m\ddot{x}_i + m\Omega_i^2 x_i = F(t) \quad (4.1)$$

where  $F(t) = \sum_j \delta(t - t_j) \hbar[k - k_{sc,i}^j]$ . Each photon  $j$  arrives at time  $t_j$  with momentum  $\hbar k$  and is scattered with momentum  $\hbar k_{sc,i}^j$  in an infinitesimal window of time. Photons impinging on the particle result in a net momentum transfer  $\mathbf{k} - \mathbf{k}_{sc}$ . For the fluctuating force  $F(t)$ , we first find the time average of the force,  $\langle F \rangle$ , and then the fluctuations about the mean,  $F'(t)$ . The momentum vectors for the incident  $\mathbf{k}$  and scattered photons  $\mathbf{k}_{sc}$  (into angular direction  $\theta, \phi$ ) are

$$\mathbf{k} = (0, 0, k)^T \quad (4.2)$$

$$\mathbf{k}_{sc} = k_{sc}(\sin \theta \cos \phi, \sin \theta \sin \phi, \cos \theta)^T \quad (4.3)$$

The time-averaged force is just the difference in momentum before and after

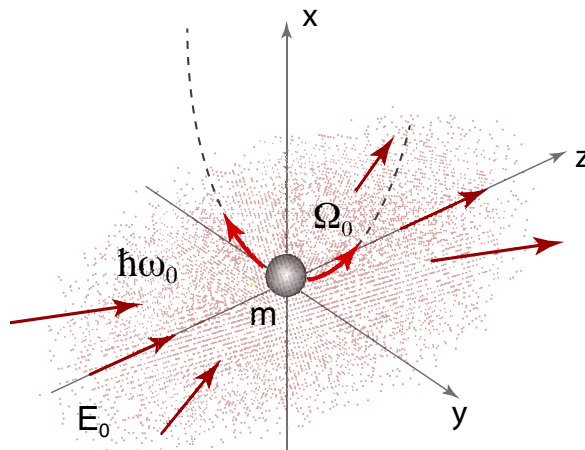


**Figure 4.1: Illustration of photon recoil heating.** A particle with mass  $m$  is trapped at the focus of a laser beam by means of the optical gradient force. The particle's center-of-mass temperature is cooled by parametric feedback and heated by individual photon momentum kicks.  $\Omega_0 / 2\pi$  is the mechanical oscillation frequency and  $\hbar\omega_0$  is the photon energy. The incident light is polarized along the  $x$  direction.

scattering, or  $\langle F \rangle = \hbar \langle r_s(\mathbf{k} - \mathbf{k}_{sc}) \rangle$ , where  $r_s = (I_0/\hbar\omega)\sigma(\omega) = P_{sc}/\hbar\omega_0$  is the average photon scattering rate,  $I_0$  is the focal intensity,  $\omega_0$  the field's frequency, and  $\sigma(\omega) = k^4\alpha^2/(6\pi\epsilon_0^2)$ , with  $k = \omega/c$  and polarizability  $\alpha = 4\pi\epsilon_0 R^3(\epsilon - 1)/(\epsilon + 2)$ .

Scattering from the oscillating particle results in a Doppler shift to the frequency of the scattered light as  $\omega = \gamma_D^{-1}\omega_0 + \beta\omega \cos\theta$  for  $\gamma_D = (1 - \beta^2)^{-1/2}$  and  $\beta = v/c$ . By expanding to lowest order in  $\beta$ , we recognize that  $\gamma_D^{-1} = 1 + \frac{1}{2}\beta^2 + \dots \sim 1$  since the particle's velocity is much lower than the speed of light. Recognize that  $\beta\omega \cos\theta = v \frac{\omega}{c} \cos\theta = \mathbf{k}_{sc} \cdot \mathbf{v}$ , such that the scattered photon's frequency is

$$\omega \simeq \omega_0 + \mathbf{k}_{sc} \cdot \mathbf{v} \quad (4.4)$$

The scattering cross-section is

$$\sigma(\omega) = \frac{\alpha^2\omega_0^4}{6\pi\epsilon_0^2c^4}(1 + \mathbf{k}_{sc} \cdot \mathbf{v}/\omega_0)^4 \simeq \sigma_0(1 + 4\mathbf{k}_{sc} \cdot \mathbf{v}/\omega_0) \quad (4.5)$$

Consequently, the scattering rate has a velocity dependence, or  $r_{sc} \simeq r_s^0(1 + 4\mathbf{k}_{sc} \cdot \mathbf{v}/\omega_0)$ . The average force on the particle, which is calculated over the dipolar scattering distribution  $P_s = \frac{3}{8\pi}(1 - \sin^2\theta \cos^2\phi)$ , is given by

$$\begin{aligned} \langle F \rangle &= r_s^0 \hbar \int_0^{2\pi} \int_0^\pi P_s[\theta](1 + 4\mathbf{k}_{sc} \cdot \mathbf{v}/\omega_0)(\mathbf{k} - \mathbf{k}_{sc}) \sin\theta \, d\theta d\phi \quad (4.6) \\ &= r_s^0 \hbar \mathbf{k} - 4(k_{sc}^2/\omega_0) \left( \frac{1}{5}v_x + \frac{2}{5}v_y + \frac{2}{5}v_z \right) \end{aligned}$$

The time-averaged force is thus the sum of a constant and a velocity-dependent term.

$$\langle F_i \rangle = r_s^0 \hbar k_i - m\gamma_{sc}^i \dot{x}_i \quad (4.7)$$

with damping  $\gamma_{sc}^i = 4\xi_i r_s^0 E_R / \frac{1}{2}\hbar\omega_0$ ,  $\xi_i = \{\frac{1}{5}, \frac{2}{5}, \frac{2}{5}\}$ , and recoil energy  $E_R = (\hbar k)^2/2m$ . The equation of motion is then

$$m\ddot{x}_i + m\gamma_{sc}^i \dot{x}_i + m\Omega_i^2 x_i = F'(t) + r_s^0 \hbar \vec{k} \quad (4.8)$$

If we shift our coordinate basis to  $X = x - r_s^0 \hbar k/m\Omega_x^2$ , we have a damped

harmonic oscillator driven by the fluctuations of the photon scattering force.

$$m\ddot{X} + m\gamma_{sc}\dot{X} + m\Omega_x^2 X = F'_x(t) \quad (4.9)$$

Such an oscillator has susceptibility  $\chi(\Omega) = [m(\Omega_x^2 - \Omega^2 + i\gamma_{sc}\Omega)]^{-1}$ .

Fluctuations of intensity engender a fluctuating force  $F'(t)$ , which imparts momentum to the particle. We calculate the energy change and the rate of momentum transfer by first computing a force autocorrelation,  $R(\tau) = \langle F'(t)F'(t + \tau) \rangle$ .

### 4.2.1 Force Autocorrelation

Assume we have an ensemble of  $K$  photons arriving in a time interval  $T$ . A photon  $j$  arrives at time  $t_j$  in the interval  $0 < t_j < T$ . We calculate the autocorrelation for a number of intervals  $M$  in the limit that  $M \rightarrow \infty$ . The photon trail is depicted in Fig. 4.2.

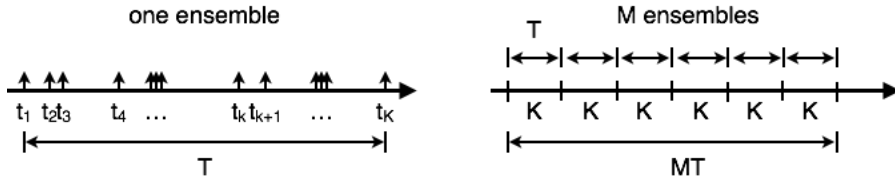


**Figure 4.2: Photon trail.** A depiction of the parameters in the autocorrelation calculation. On the left is an ensemble of  $K$  photons occurring at times  $t_j$  within a fixed time interval  $T$ . On the right are  $M$  ensembles of intervals of length  $T$  containing  $K$  photons.

The force from one ensemble of  $K$  photons is

$$F_K(t) = \sum_{j=1}^K \hbar(k - k_{sca}^j) \delta(t - t_j) \quad (4.10)$$

Multiplying by the force delayed by a time  $\tau$  and averaging over all values of the individual arrival times  $t_1, t_2, \dots, t_j, t_{j+1}, \dots, t_K$  in the limit  $M \rightarrow \infty$ , the



force autocorrelation is

$$\langle F_K(t)F_K(t + \tau) \rangle = \sum_{j=1}^K \sum_{m=1}^K \int_0^T \frac{dt_1}{T} \dots \int_0^T \frac{dt_K}{T} \quad (4.11)$$

$$\times \hbar^2 (k - k_{sca}^j)(k - k_{sca}^m) \delta(t - t_j) \delta(t + \tau - t_m) \quad (4.12)$$

Two distinct situations arise as either (i)  $j = m$  or (ii)  $j \neq m$ . With  $K^2$  terms altogether, there are  $K$  instances of  $j = m$  and  $K^2 - K$  instances of  $j \neq m$ . When  $j = m$ , the mean square fluctuation is

$$\int_0^T \frac{dt_j}{T} \hbar^2 (k - k_{sca}^j)^2 \delta(t - t_j) \delta(t + \tau - t_j) \quad (4.13)$$

and when  $j \neq m$

$$\int_0^T \frac{dt_j}{T} \hbar (k - k_{sca}^j) \delta(t - t_j) \int_0^T \frac{dt_m}{T} \hbar (k - k_{sca}^m) \delta(t + \tau - t_m) \quad (4.14)$$

The autocorrelation is then the sum of two terms

$$\langle F_K(t)F_K(t + \tau) \rangle = \frac{K}{T} \hbar^2 \langle (k - k_{sca})^2 \rangle \delta(\tau) + \frac{K(K-1)}{T^2} \hbar^2 \langle k - k_{sca} \rangle^2 \quad (4.15)$$

Now we average over all of the  $M$  intervals instead of only over those having  $K$  arrivals by applying a Poisson probability distribution  $p(K) = (r_s T)^K e^{-r_s T} / K!$ . The autocorrelation is then the sum of two terms, or

$$\langle F(t)F(t + \tau) \rangle = r_s \hbar^2 \langle (k - k_{sca})^2 \rangle \delta(\tau) + \langle F_x \rangle^2 \quad (4.16)$$

To compute the autocorrelation of the position-shifted oscillator, we subtract the square of the mean force, which gives us

$$R(\tau) = r_s \hbar^2 \langle (k - k_{sca})^2 \rangle \delta(\tau) \quad (4.17)$$

Applying the Wiener-Khinchin Theorem, we compute the force power spectral density  $S_{sc}^F(\Omega)$  by taking a Fourier transform of the force autocorrelation

function.

$$\begin{aligned}
 S_{\text{sc}}^F(\Omega) &= \frac{1}{2\pi} \int_{-\infty}^{\infty} d\tau R(\tau) e^{i\Omega\tau} \\
 &= \frac{1}{2\pi} \hbar^2 r_s^0 \int_0^{2\pi} \int_0^\pi P_S(\theta, \phi) k_{\text{sc}}^2 \begin{pmatrix} \sin^2 \theta \cos^2 \phi \\ \sin^2 \theta \sin^2 \phi \\ \cos^2 \theta \end{pmatrix} \sin \theta d\theta d\phi \\
 &= \lambda_i \frac{\hbar\omega_0}{2\pi c^2} P_{\text{sc}}
 \end{aligned} \tag{4.18}$$

where the constant  $\lambda_i = \{\frac{1}{5}, \frac{2}{5}, \frac{2}{5}\}$  in  $x$ ,  $y$ , and  $z$ . There is an additional contribution to the fluctuating force from the Doppler-shifted frequencies. Here, we have retained just the first-order contribution, which does not include the Doppler shift, solely in order to estimate the influence of the photon number fluctuations.

### 4.2.2 Optical Temperature

The optical field interacting with the particle gives rise to dissipation and a fluctuating force. If we invoke the Fluctuation Dissipation Theorem [31], the particle would reach an equilibrium temperature  $T_{ph}^y$  along the  $y$ -axis equal to

$$\begin{aligned}
 2m\gamma_{ph}k_B T_{ph}^y &= \hbar^2 k^2 r_s^0 \\
 k_B T_{ph}^y &= \frac{1}{8} \hbar\omega_0
 \end{aligned} \tag{4.19}$$

The center-of-mass temperature to which the particle equilibrates is independent of the scattered power and only depends on the photon's energy  $\hbar\omega_0$ . Raising the scattered power  $P_{\text{sc}}$  only increases the equilibration rate.

### 4.2.3 Mean Energy Rate of Change

The oscillator's composite damping rate can be written as  $\gamma = \gamma_{\text{th}} + \gamma_{\text{sc}} + \gamma_{\text{fb}}$ , where  $\gamma_{\text{th}}$  accounts for interactions with the background gas,  $\gamma_{\text{sc}}$  with the radiation field, and  $\gamma_{\text{fb}}$  is the damping introduced by feedback cooling. The different contributions will be discussed in detail.

The trapped particle's energy changes constantly due to interactions with its environment and the time evolution of its average energy  $\bar{E}$  is predicted by the Fokker-Planck equation to be [91]

$$\frac{d}{dt}\bar{E}(t) = -\gamma [\bar{E}(t) - E_\infty] \quad (4.20)$$

where  $E_\infty$  is the average energy in the steady state ( $t \rightarrow \infty$ ) and  $\gamma$  is the rate at which the steady state is reached. Writing the average energy of the particle in terms of discrete quanta,  $\bar{E} = n \hbar \Omega_0$ , we obtain

$$\dot{n} = -\gamma n + \Gamma \quad (4.21)$$

where  $n$  is the mean occupation number and

$$\Gamma = \frac{E_\infty}{\hbar \Omega_0} \gamma \quad (4.22)$$

is the heating rate. It defines the rate at which phonons are reintroduced into the mechanical system. The solution of Eq. (4.21) is

$$n(t) = n_\infty + [n_0 - n_\infty] e^{-\gamma t}, \quad (4.23)$$

where  $n_0$  is the mean occupation number at an initial time and

$$n_\infty = \frac{\Gamma}{\gamma} = \frac{\Gamma_{\text{th}} + \Gamma_{\text{recoil}}}{\gamma_{\text{th}} + \gamma_{\text{rad}} + \gamma_{\text{fb}}} \quad (4.24)$$

is the occupation number in the steady state. In (4.24) we have written  $\Gamma$  as the sum of a heating rate due to collisions with gas molecules ( $\Gamma_{\text{th}}$ ) and a heating rate due to photon recoil kicks ( $\Gamma_{\text{recoil}}$ ).

The surrounding gas at temperature  $T$  gives rise to damping  $\gamma_{\text{th}}$  and thermal decoherence  $\Gamma_{\text{th}} = \gamma_{\text{th}} k_B T / \hbar \Omega_0$ . For  $\gamma > \Omega_0$ , the particle's motion is overdamped and the dynamics are governed by a diffusion equation, as in the case of optical tweezers operated in liquids.

Left alone, the trapped particle will have  $n_{\text{th}} = k_B T / \hbar \Omega_0$  thermal quanta on average. However, by means of phase-sensitive parametric feedback we

reduce the oscillator's susceptibility by raising damping to  $\gamma_{\text{fb}}$ , which leaves the particle in a state with  $n_\infty \approx \Gamma_{\text{th}}/\gamma_{\text{fb}}$ . The feedback consists of a split detection scheme in combination with a phase-locked loop (PLL) for phase sensitive detection of the particle's motion and feedback control.

#### 4.2.4 Recoil Heating Rate

The power spectral density of the displacement along the  $y$  direction is

$$S_{yy}(\Omega) = |\chi(\Omega)|^2 S_{\text{sc}}^F, \quad (4.25)$$

The mean-square displacement is calculated as

$$\langle y^2 \rangle = \int_{-\infty}^{\infty} S_{yy}(\Omega) d\Omega = \frac{1}{5} \frac{\hbar\omega_0}{m\Omega_0^2} \frac{P_{\text{sc}}}{mc^2} \frac{1}{\gamma}. \quad (4.26)$$

Assuming that the particle attains a thermal steady state, we invoke the equipartition theorem  $\hbar\Omega_0 n_\infty = K_s \langle y^2 \rangle$ , with trap stiffness  $K_s = m\Omega_0^2$ . Inserting this expression into (4.22) we finally find the recoil heating rate to be

$$\Gamma_{\text{recoil}} = \frac{1}{5} \frac{P_{\text{sc}}}{mc^2} \frac{\omega_0}{\Omega_0}, \quad (4.27)$$

in agreement with theory [40, 107, 108]. The recoil rate scales with the number of scattered photons and with the mass (as  $P_{\text{sc}}/m \propto m$ ) but inversely with the trap frequency.

##### 4.2.4.1 Experimental Estimates

Let us estimate the magnitude of  $\Gamma_{\text{rec}}$ . For a Gaussian beam, the intensity at the laser focus is  $I_0 = P_0 k^2 \text{NA}^2 / 2\pi$ , where  $k = \omega_0/c$ . The scattered power is then calculated as  $P_{\text{sc}} = \sigma_{\text{sc}} I_0$ . For the parameters used in our experiments ( $n = 1.45$ ,  $\lambda = 1064 \text{ nm}$ ,  $P_0 = 70 \text{ mW}$ ,  $R = 50 \text{ nm}$ ,  $\text{NA} = 0.9$ ) we find  $P_{\text{sc}} = 3.6 \mu\text{W}$ . The laser wavelength is  $2\pi c/\omega_0 = 1064 \text{ nm}$  and the mass of the particle amounts to  $m = 1.14 \times 10^{-18} \text{ kg}$ . Using  $\Omega_0 = 2\pi \times 150 \text{ kHz}$ , Eq. (4.27) predicts a reheating rate of  $\Gamma_{\text{rec}} = 13.1 \text{ kHz}$ .

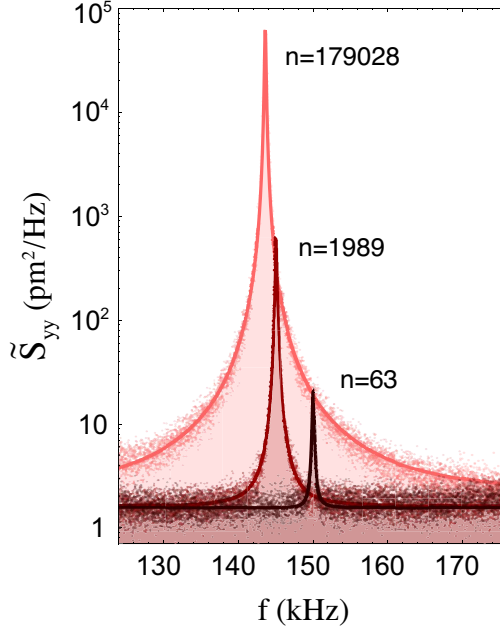


**Figure 4.3: Power spectral densities under feedback cooling.** The Lorentzian curves correspond to the motion along  $y$  for three different vacuum pressures:  $6.6 \times 10^{-4}$ ,  $1.1 \times 10^{-5}$  and  $2 \times 10^{-8}$  mbar (in order from the highest to the lowest curve).  $n$  indicates the mean occupation number. The center-of-mass temperature of the  $n = 63$  peak is  $T_{\text{cm}} = 450 \mu\text{K}$ . Note that  $\tilde{S}_{yy}$  is the single-sided PSD.

In addition to heating, the radiation field also leads to radiation damping at a rate  $\gamma_{\text{sc}}$ , which arises from the Doppler effect [109, 110] and can be evaluated by calculating the back-action of the scattered field on the motion of the particle along the  $y$  axis. We find a value of  $\gamma_{\text{sc}} \sim P_{\text{sc}}/mc^2$ . Note that in the photon dominated regime and in the absence of feedback cooling, the equilibrium temperature  $k_B T_\infty = \hbar\Omega_0 n_\infty \sim \hbar\omega_0$  is of the order of the photon energy. This energy is comparable to the depth of the trapping potential and therefore the particle is likely to escape as it heats up without feedback control.

### 4.3 Experimental Results

We first measure temperature at a few distinct pressures, as shown in Fig. 4.3. At the lowest pressure, the bottom-most PSD is the maximum compression achieved. Here, we have reduced the temperature to  $T_y = 450 \pm 33.1 \mu\text{K}$ , which corresponds to an occupation of  $n_y = 62.5 \pm 5$ .

To experimentally test the transition between the gas and the photon dominated regimes, we record the particle's average energy  $\bar{E}$  as a function of gas pressure  $P_{\text{gas}}$  under constant feedback cooling. The result is shown in Fig. 4.4 where we expressed the average energy in terms of the mean occupation number  $n_\infty = \bar{E}/\hbar\Omega_0$ . The figure demonstrates that as pressure is reduced to  $10^{-7}$  mbar, the gas damping attenuates linearly with pressure, in agreement with Eq. (3.32). At pressures lower than  $\sim 10^{-7}$  mbar, however, the particle's motion is weakly influenced by interactions with the gas. In this regime the dynamics are primarily determined by particle-photon interactions.

The center-of-mass temperature corresponds to the integral of the power spectral density (c.f. Fig. 4.3), while the width of the peak yields the damping  $\gamma \simeq \gamma_{\text{fb}}$ . For example, the Lorentzian peak labeled with  $n = 63$  in Fig. 4.3 yields damping  $\gamma_{\text{fb}} = 269.9 \pm 7.8$  Hz. Using the oscillator's phonon occupation and feedback-cooled linewidth, we find  $\Gamma = n_\infty \gamma_{\text{fb}} = 63 \times 270 \text{ Hz} = 17 \pm 1.3$  kHz, in close agreement with theoretical predictions of  $\Gamma = 21.7$  kHz.

To corroborate this result we perform a direct measurement of the recoil rate in a ring up style experiment, whereby the feedback is switched off at  $t = 0$  and the particle is allowed to heat up. However, as described in Ref. [91], individual reheating trajectories represent a stochastic process and, thus, the heating rate and temperature have to be extracted from averages over many individual reheating trajectories.

After switching-off the feedback we follow individual reheating trajectories over time periods that are considerably shorter than  $1/\gamma$ , which allows us to linearize the exponential term in Eq. (4.23). We then obtain

$$n(t) = n_0 - \gamma [n_0 - n_\infty] t + .. \approx n_0 + \Gamma_{\text{recoil}} t. \quad (4.28)$$

In the last step, we used the fact that  $n_0 \ll n_\infty$ , a condition that is fulfilled in

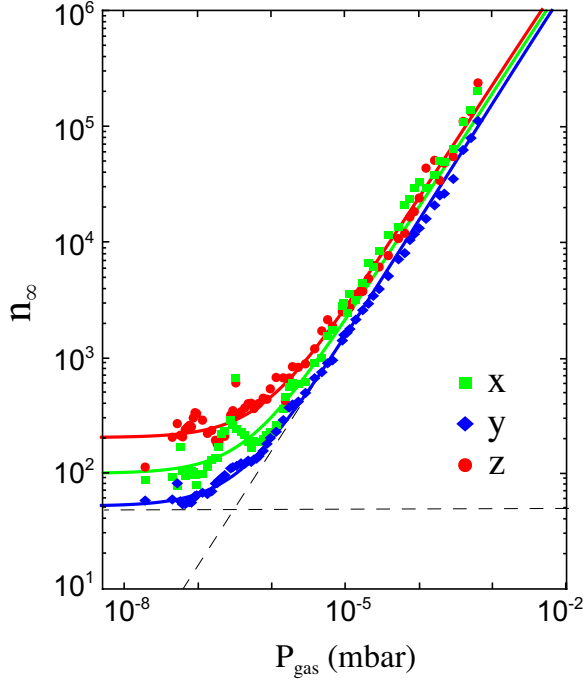


**Figure 4.4: Steady-state under feedback cooling.** Mean occupation number along the three principal axes ( $x$ ,  $y$ ,  $z$ ) as a function of gas pressure measured under constant feedback cooling for a  $R = 49.8$  nm particle with focal power  $P_0 = 70$  mW. The solid curves are fitting functions of the form  $a + bP_{\text{gas}}$ . The diagonal and horizontal lines indicate, for the  $y$  axis, the asymptotic limits of gas and photon recoil heating, respectively.

our experiments owing to feedback cooling. Thus, we find that the reheating is linear in time shortly after switching off the feedback and that the reheating rate corresponds to the photon recoil rate  $\Gamma_{\text{recoil}}$ . We extract  $\Gamma_{\text{recoil}}$  from our measurements and study it as a function of system parameters, such as laser power, particle size, and gas pressure.

Figure 4.5a shows experimentally measured reheating time-traces for two different particles with radii  $R_1 = 50.7$  nm and  $R_2 = 72.6$  nm. The initial

occupation number  $n_0$  for the two particles is slightly different and the oscillation frequencies are  $\Omega_0^{(1)} = 2\pi \times 148.8$  kHz and  $\Omega_0^{(2)} = 2\pi \times 151.2$  kHz. The slope of the time-traces directly renders the reheating rate. We obtain  $\Gamma_1 = (20.9 \pm 0.2)$  kHz and  $\Gamma_2 = (29.4 \pm 0.3)$  kHz. Theoretical estimates are  $\Gamma_1 = 15.5$  kHz and  $\Gamma_2 = 38.2$  kHz.

We also measured the reheating rate as a function of focal power  $P_0$ . Fig. 4.5b shows the reheating time-traces of a  $R = 68$  nm particle measured

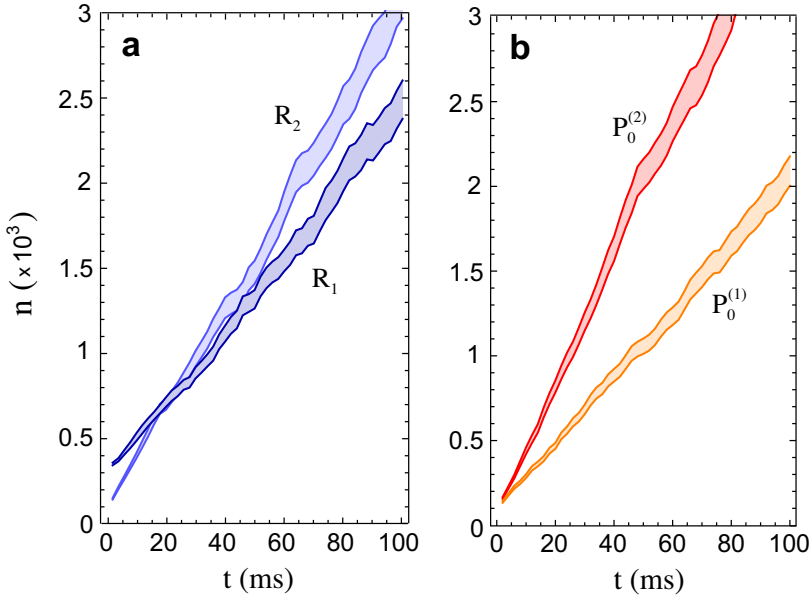


**Figure 4.5: Reheating time-traces.** Particle reheating along the  $y$  axis for different particle sizes and laser powers. Plotted is one standard deviation above and below the mean phonon value. The slope of a weighted least-squares fit to the curves renders the reheating rate  $\Gamma$ . The experimental data are obtained by averaging 500 individual reheating trajectories. (a) Reheating for  $R_1 = 52.7$  nm (dark blue) and  $R_2 = 71.6$  nm (light blue). The pressure is  $3 \times 10^{-8}$  mbar and the focal power is 70 mW. (b) Reheating for a particle with radius  $R = 68$  nm measured for two different focal powers,  $P_0^{(1)} = 30.5$  mW and  $P_0^{(2)} = 80$  mW, at a pressure  $7 \times 10^{-9}$  mbar.



with laser powers  $P_0^{(1)} = 30.5$  mW and  $P_0^{(2)} = 80$  mW. The oscillation frequencies for the two laser powers are  $\Omega_0^{(1)} = 2\pi \times 100.5$  kHz and  $\Omega_0^{(2)} = 2\pi \times 158.8$  kHz with corresponding reheating rates  $\Gamma_1 = (19.4 \pm 0.1)$  kHz and  $\Gamma_2 = (38.0 \pm 0.3)$  kHz. By comparison, we predict  $\Gamma_1 = 21.5$  kHz and  $\Gamma_2 = 35.8$  kHz for the given parameters.

Discrepancies between measured rates and the predictions exist. The focal intensity is calculated in the paraxial approximation, which overestimates its value and the resulting photon scattering rate. Future studies would benefit from numerical simulations of focal fields in the strong-focusing domain. When accounting for the diffractive effects of the light field, we would have more accurate estimates of the recoil rate.

The particle size is determined from fits to its spectral linewidth at 10 mbar. Artificial broadening of the lineshape by nonlinear components of the trapping potential and reductions in the particle density in high vacuum would estimate smaller particle sizes and lower scattering rates.

As shown in Fig. 4.5a, increasing the particle's size heats it up faster despite starting off with lower  $n$ . Raising the focal intensity from 30.5 mW to 80 mW doubles the rate. Under recoil heating, the rate scales as  $\Gamma_{\text{rec}} \propto P_0/\Omega_0 \propto \sqrt{P_0}$ , which means we expect the rate in Fig. 4.5b to increase by a factor of 1.6. Recoil heating is proportional to the inverse of  $\Omega_0$ , which is consistent with the measurements in Fig. 4.4, where the weakest reheating is observed for the  $y$  axis ( $\Omega_0 = 2\pi \times 150$  kHz), followed by the  $x$  axis ( $\Omega_0 = 2\pi \times 129$  kHz) and then the  $z$  axis ( $\Omega_0 = 2\pi \times 49$  kHz).

We estimate that the residual thermal dissipation amounts to 4% of the measured reheating rates in these experiments, given the very low vacuum pressure.

## 4.4 Additional Laser Heating Mechanisms

Next, we compare these results to other decoherence mechanisms the particle may be susceptible to. In addition to recoil heating from the random scattering of photons, classical laser intensity fluctuations and pointing fluctuations will affect the trap's stability.

#### 4.4.1 Classical intensity noise

An oscillating nanoparticle subject to intensity fluctuations will have a noisy spring constant such that the equation of motion is

$$m\ddot{y} + m\gamma\dot{y} + k(t)y = \mathcal{F}(t) \quad (4.29)$$

where  $k(t) = k_0(1 + \varepsilon(t))$ . This gives rise to a heating rate of [111, 112]

$$\Gamma_\varepsilon = \pi\Omega_0^2 S^\varepsilon[2\Omega_y] n = \gamma_\varepsilon n \propto P_0 \quad (4.30)$$

Here,  $S^\varepsilon$  is the power spectral density of the noise (in units of  $\text{Hz}^{-1}$ ),  $\varepsilon(t)$ , and is evaluated at twice the oscillation frequency  $2\Omega_y$ . This modifies the rate equation in (4.21) into

$$\dot{n} = -\gamma_{\text{rad}}n + \Gamma_{\text{recoil}} + \gamma_\varepsilon n \quad (4.31)$$

The linearized solution becomes

$$n(t) = n_0 + (\Gamma_{\text{recoil}} + \gamma_\varepsilon n_0)t \quad (4.32)$$

Thus, the more the particle is cooled and the lower  $n_0$  is, the less it suffers from parametric heating due to laser intensity noise. Though the heating rate due to laser noise scales linearly with power, it has no dependence on mass. At the occupation numbers achieved with phase-based feedback, where  $n_0 \simeq 100$ , together with the relative intensity noise (RIN) of the trapping laser of  $S^\varepsilon = -138 \text{ dB/Hz}$ , we obtain  $\gamma_\varepsilon n_0 = 56 \text{ Hz}$ , which is negligible compared to the recoil heating rate  $\Gamma_{\text{recoil}} \sim 10 \text{ kHz}$ .

#### 4.4.2 Trap Center Fluctuations

Pointing fluctuations of the laser beam translate to displacements of the trap center. This results in an equation of motion that is [112]

$$m\ddot{y} + m\gamma\dot{y} + k(y - \varepsilon'(t)) = \mathcal{F}(t) \quad (4.33)$$

where  $\varepsilon'(t)$  is the displacement. This gives rise to a mean energy rate of change [111, 112]

$$\frac{d\bar{E}}{dt} = \frac{\pi}{2} m \Omega_0^4 S^{\varepsilon'}[\Omega_0] \propto P_0^2 m \quad (4.34)$$

where  $S^{\varepsilon'}[\Omega_0]$  is the spectral density of the position fluctuations at the trap center. When rewritten in terms of phonons,  $\dot{\bar{E}} = \hbar \Omega_0 \dot{\bar{n}}$ , and the rate is then

$$\Gamma_{\varepsilon'} = \frac{\pi}{2} m \Omega_0^3 S_x(\Omega_0) / \hbar \quad (4.35)$$

This rate in Eq. (4.34) scales linearly with the mass, which we observe in the measurements of Fig. 4.5a. It scales with  $\Omega_0^3$ , which is proportional to  $P_0^{3/2}$ . When in Fig. 4.5b we raise power from 30.5 to 80 mW, we would expect a factor of 4.2 rise in the reheating rate from pointing fluctuations, which is double what we observed.

### 4.4.3 Discussion

The measurements presented indicate that heating due to the shot noise of photons is the dominant dissipation mechanism in the system. Dissipation due to photon shot noise overwhelms thermal dissipation by at least a factor of 25 in these experiments, which is a ratio that could be raised by further reducing the vacuum pressure. For nanoscale particles  $\Gamma_{\text{rec}}$  is approximately 10 kHz, which sets limits to ground-state cooling protocols, upper bounds to quality factors, and limits the maximum achievable force sensitivity.

## 4.5 Standard Quantum Limit

Given that the reheating rates scale linearly with mass and with optical power, we conclude that recoil heating is the dominant reheating mechanism. Reaching the ground state requires reducing recoil heating in the same way that gas damping was attenuated by reducing pressure. Feedback cooling, however, requires a high precision measurement of the particle's motion while reduced recoil heating requires less focal power. In this section we focus on the standard quantum limit of continuous measurement for reducing position fluctuations amid measurement imprecision and back-action.

### 4.5.1 Measurement Imprecision

The number of photons scattered by a particle is  $(P_{sc}/\hbar\omega_0)\Delta t$  and equals

$$N_{sc} = \sigma \frac{I_0}{\hbar\omega_0} \Delta t = P_0 \frac{4}{3} \left( \frac{\epsilon - 1}{\epsilon + 2} \right)^2 \frac{k^5 R^6 \text{NA}^2}{\hbar c} \Delta t \quad (4.36)$$

We detect just a fraction of the scattered photons, namely  $N_{det} = \eta_c N_{sc}$ , where the collection efficiency  $\eta_c$  is given by

$$\eta_c = \frac{1}{32} [16 - 15\sqrt{1 - \text{NA}_c^2} - \cos(3 \arcsin(\text{NA}_c))] \quad (4.37)$$

The laser power incident on the detector is

$$P_{det}(\mathbf{r}) = \eta_c P_{sc} + P_{ref} + 2\sqrt{\eta_c P_{sc}} \sqrt{P_{ref}} \sin(\phi(\mathbf{r})) \quad (4.38)$$

resulting from the interference of the laser and scattered fields. The laser field  $P_{ref}$  is much stronger than the scattered field  $P_{sc}$ . Thus, the dominant detector noise is due to the shot noise of the laser field, or  $\langle P_N^2 \rangle = \frac{1}{\pi} \hbar\omega_0 P_{ref} \Delta\omega$ , where  $\Delta\omega$  is the detector signal bandwidth.

A displacement of the particle generates a slight shift in the phase of the scattered field, or  $\langle P_S^2 \rangle = 4\eta_c P_{sc} P_{ref} \cos^2 \phi \langle d\phi^2 \rangle$ . Due to the Gouy phase shift,  $\cos^2 \phi \simeq 1$  and  $\langle d\phi^2 \rangle = k^2 \sum_i \lambda_i \langle x_i^2 \rangle$ , where  $\lambda_i$  accounts for the geometric distribution of the dipole radiation field. The imprecision of  $x_i$  due to shot noise is determined when the ratio of the signal power to noise power equals 1, or

$$\langle x_i^2 \rangle_{imp} = \frac{\hbar\omega_0}{2k^2 \eta_c \lambda_i} \frac{1}{P_{sc}} \Delta f \quad (4.39)$$

This result agrees with a calculation based on Heisenberg's Uncertainty Principle in Ref. [113].

### 4.5.2 Measurement Backaction

The displacement due to photon scattering in Eq. 4.26 can be rewritten as

$$\langle x_i^2 \rangle_{ba} = \lambda_i \frac{\hbar\omega_0}{m\Omega_0^2} \frac{P_{sc}}{2mc^2} \frac{1}{\gamma^2} \Delta f \quad (4.40)$$

Combining the two expressions, the total displacement is

$$\langle x_i^2 \rangle_{\text{tot}} = \frac{1}{2} \langle x_i^2 \rangle_{\text{zpf}} \left( \frac{\omega_0 m \Omega_0}{\lambda_i \eta_c k^2} \frac{1}{P_{\text{sc}}} + \lambda_i \frac{2\omega_0}{\Omega_0 m c^2 \gamma^2} P_{\text{sc}} \right) \Delta f \quad (4.41)$$

where here  $\langle x_i^2 \rangle_{\text{zpf}} = \hbar/2m\Omega_0$ . Counter to most opto-mechanical systems, in an optical-tweezer system the frequency  $\Omega_0 \propto \sqrt{P_{\text{sc}}}$ . Plugging in  $\Omega_0 = (f_s \text{NA}^2 3\pi\epsilon_0 P_{\text{sc}} / \alpha c m k^2)^{1/2}$ , the total displacement is

$$\begin{aligned} \langle x_i^2 \rangle_{\text{tot}} = \frac{1}{2} \langle x_i^2 \rangle_{\text{zpf}} & \left[ \frac{\omega_0}{\lambda_i \eta_c k^2} \left( f_s \frac{\text{NA}^2 3\pi\epsilon_0 m}{\alpha c k^2} \frac{1}{P_{\text{sc}}} \right)^{1/2} \right. \\ & \left. + \frac{\lambda_i \omega_0}{\gamma^2 c^2} \left( \frac{\alpha c k^2}{f_s \text{NA}^2 3\pi\epsilon_0 m} P_{\text{sc}} \right)^{1/2} \right] \Delta f \end{aligned} \quad (4.42)$$

We find the expression in Eq. 4.42 is minimized when

$$P_{\text{sc}}^{\text{min}} = \frac{3f_s m c \text{NA}^2 \pi \gamma^2 \epsilon_0}{k^4 \alpha \eta_c \lambda_i^2} \quad (4.43)$$

At this power, when  $\Delta f = \gamma$ , the total displacement is

$$\langle x_i^2 \rangle_{\text{tot}} = \langle x_i^2 \rangle_{\text{zpf}} / \sqrt{\eta_c} \quad (4.44)$$

which indicates that the zero-point fluctuations can only be resolved under unit collection efficiency. In this limit of  $\eta_c \rightarrow 1$ , the ground state can be detected and not destroyed despite back-action from the optical field.

For the configuration of our experiment, we plot in Fig. 4.6 the peak displacement as a function of the feedback damping  $\gamma$ . For the focal power and feedback gain applied, the particle lies in the domain of strong measurement backaction. Increasing feedback gain and reducing measurement imprecision by an order of magnitude shifts the balance closer toward the ground state. This is because feedback counters the influence of measurement back-action. Reducing the measurement imprecision requires improvements in the detection scheme, which we return to in Ch. 6

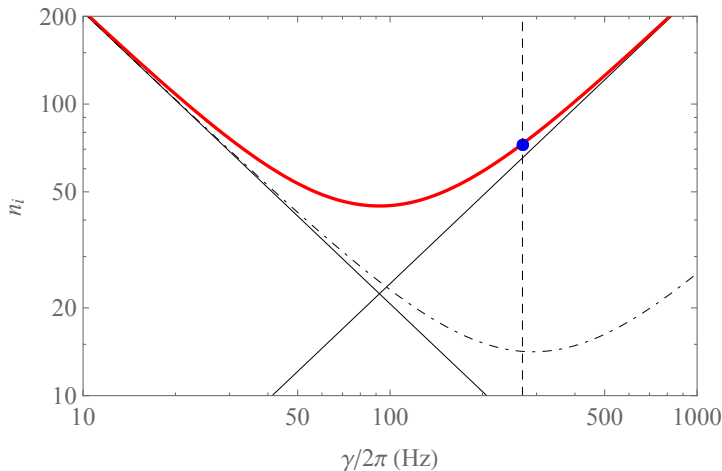


**Figure 4.6: Standard quantum limit** Total displacement imprecision expressed in terms of mean phonon occupations  $n_i = \langle x_i^2 \rangle / \langle x_i^2 \rangle_{\text{zpf}}$  as a function of the feedback damping  $\gamma$  for  $\eta_c = 0.0005$  and  $P_{\text{sc}} = 3.53 \mu\text{W}$ . The blue dot corresponds to our experimental conditions ( $\gamma/2\pi = 269.9$  Hz). The two diagonal lines indicate the contributions of measurement noise and backaction noise, respectively. The dash-dotted curve shows the response for detection efficiency increased by a factor of ten.

## 4.6 Conclusion

There are a few things one should take away from this discussion. First, and foremost, ground-state cooling is achievable with an ideal measurement in an optical tweezer trap. Second, optical tweezer traps don't respond linearly to changes in optical power as most opto-mechanical systems do. Rather, they vary with the square root. Third, the contribution to total displacement arising from backaction scales with  $1/\gamma^2$ , or essentially the damping. This is most intriguing as the backaction arises from the quantum nature of light whereas the damping results entirely from a classical feedback process. The photon fluctuations would otherwise drive the particle out of the trap if it were not for feedback cooling.

For the system presented in these measurements, imprecision noise accounts for  $8.0 \langle x^2 \rangle_{\text{zp}}$  and backaction noise for  $33.4 \langle x^2 \rangle_{\text{zp}}$ . This means the trapped

nanoparticle is in a regime dominated by measurement backaction. In fact, the motion due to backaction overwhelms that due to thermal motion by nearly 25 times. It is, in fact, in this regime that opto-mechanical systems need to operate in order to use mechanical resonators to measure the properties of quantum fields of light. Given that the recoil heating rate is on the order of 10 kHz, one would expect roughly  $\Omega_0/\Gamma_{\text{rec}} = 15$  coherent oscillations in the ground state before the system is reheated by one phonon due to backaction.





# 5

---

## Noise in the Trap

The goal of this chapter is to quantify the contribution of classical intensity fluctuations to our measurements of recoil heating. Here, we study classical noise sources, including laser intensity noise and electric field fluctuations.

### **5.1 Introduction**

Noise in harmonic traps has an extensive history that is grounded in the most basic of noise processes – Brownian motion [114]. Broadly speaking, the primary goal in the field of opto-mechanics is to counteract noise from the environment – thermal and optical fluctuations – that drive mechanical resonators into motion and limit their sensitivity in force detection [104]. Optical levitation seeks to overcome thermal and acoustic noise by operating in UHV [40].

The development of optical tweezers brought many advances in the use of lasers for stabilizing and manipulating matter [34]. Laser cooling of atoms using the radiation pressure exerted by light enabled increased accuracy of atomic clocks, improved spectroscopy of atomic and ionic species, and the

formation of new states of matter at ultracold temperatures [39, 107, 115–117]. Recognizing that neutral atoms far off of resonance in optical traps act as optical dipoles, Savard, et al., calculated the contribution of classical laser noise to a harmonic trap’s stability [112]. It was found that intensity fluctuations with a correlation time much shorter than the harmonic oscillation generate a parametric heating process whereby the dipole is driven by the noise power of fluctuations at twice the harmonic frequency, or  $2\Omega_0$ . The strength of the drive, however, is proportional to the oscillator’s motional energy. They demonstrated that beam-pointing fluctuations, which shift the center of the trap, resonantly drive the particle and act as another heat bath. Gehm, et al., demonstrated that fluctuations in trap parameters can cause atoms to heat up and determined the trap stability needed to achieve long storage times [111].

Noise in harmonic systems can be grouped into two general categories: additive and multiplicative [66, 118]. Additive noise processes, including thermal fluctuations and recoil heating, result from external forces that drive the harmonic oscillator into motion. They are the source of Brownian motion and result in a particle diffusing in free space and also include the vacuum fluctuations of the electromagnetic field that trigger spontaneous emission of atoms. Multiplicative noise processes depend on the state of the system, including the position  $x$  or velocity  $\dot{x}$ , and result from time-varying parameters, notably the frequency, damping, or mass. The presence of multiplicative noise has implications in nearly all realms of science, including stochastic resonance [119], noise induced phase transitions [120], Josephson tunneling junctions [66], nonlinear optics, and population dynamics [118].

We focus here on laser noise and how it affects the trapped nanoparticle different from recoil heating. Laser noise couples to the particle’s motion additively in the form of radiation pressure and multiplicatively by modulating the spring constant. When noisy radiation pressure acts on the particle, it drives its motion in  $z$ , or along the optical axis, but has no influence on the transverse axes. Though the particle scatters the noisy laser field, the symmetric nature of dipole radiation means that the up and down (in  $y$ ) or left and right (in  $x$ ) trajectories resulting from classical noise destructively interfere.

A jittering spring constant  $k$  from laser noise induces changes to the oscillation frequency  $\Omega_0^2 = k/m$ . Multiplicative noise is important to control

because it may limit trap stability altogether [111, 121]. Jitter in frequency limits the length of time over which one may integrate the particle's motion in the context of force detection applications [122, 123]. Furthermore, classical noise fluctuations may erode quantum noise signatures, including those of the vacuum field fluctuations, that may be exploited for metrology in absolute thermometry and quantum information processing [16, 27, 99, 124, 125].

In this chapter we present models for classical laser intensity noise and its influence on the center of mass motion, measurements of noise injection and reduction in the trap, and quantitative characterization of intensity noise. We characterize the frequency stability for our system and calculate how it may deteriorate force sensitivity.

## 5.2 Theory of Parametric Noise

The optical dipole trap is formed by a focused laser beam with power  $P_0$ . The resulting gradient force  $F_{\text{grad}} = -kq$  has a trap stiffness  $k \propto P(t) = P_0 + \delta P(t)$ , where  $P_0$  is the average power and  $\delta P(t)$  the fluctuations in power. Its frequency fluctuates as  $\Omega(t)^2 = \Omega_0^2(1 + \eta(t))$ , where  $\eta(t) = \delta P(t)/P_0$ . Under parametric feedback control, the corresponding equation of motion is

$$\ddot{q} + \Omega_0^2 q = -\gamma \dot{q} - \Omega_0^2 \zeta_0 \cos(\Omega_m t) q - \Omega_0^2 \eta(t) q + F_{\text{th}}(t)/m \quad (5.1)$$

where  $\zeta_0$  is the feedback gain; the fluctuating power is taken to be very small ( $\eta \ll 1$ ). The right-hand side of Eq. 5.1 has from left to right the damping force, parametric feedback, fluctuating frequency, and fluctuating thermal force. The fluctuating and damping forces can also be replaced by their optical analogues  $-\gamma_{\text{rad}} \dot{q}$  and  $F_{\text{ph}}(t)/m$  of Ch. 4, respectively.

$\eta(t)$  is assumed to be a Gaussian white noise process with zero mean and an autocorrelation  $\langle \eta(t)\eta(t') \rangle = 2\eta_0^2 \delta(t - t')$ . It is related to the laser's relative intensity noise by

$$S_{\text{RR}} = \frac{1}{2\pi} \int_{-\infty}^{\infty} dt' \langle \eta(t)\eta(t') \rangle e^{i\Omega t'} = \eta_0^2/\pi \quad (5.2)$$

Next, we will set the equations of motion in the standard Langevin form

and average over the fast oscillation cycle time  $\tau = 2\pi/\Omega_0$  to get the slowly-varying dynamics of the system [92, 93, 126]. We follow an approach outlined in Ref. [127]. Expressing momentum as the rate of change of position, or  $\dot{q} = p/m$ , the infinitesimal change in position  $dq$  and momentum  $dp$  are

$$dq = (p/m)dt \quad (5.3a)$$

$$dp = (-m\Omega_0^2 q - \gamma p - \zeta m\Omega_0^2 \cos(\Omega_m t)q) dt \quad (5.3b)$$

$$+ \sqrt{2m\gamma k_B T} dW_1 + m\Omega_0^2 \eta q dW_2$$

Here, we have expressed the random fluctuating forces as Wiener processes where  $F_{\text{th}}(t) = \sqrt{2m\gamma k_B T_0} w_1(t)$  and  $\eta(t) = \eta_0 w_2(t)$ ;  $w_1(t) = dW_1/dt$  and  $w_2(t) = dW_2/dt$  for the thermal force and the laser intensity fluctuations, respectively. These are zero-mean noise processes, are independent and uncorrelated with each other, and have correlation times much faster than the particle's dynamics. These conditions are best summarized as

$$\langle W_1(t) \rangle = 0 = \langle W_2(t) \rangle \quad (5.4a)$$

$$\langle W_1(t)W_1(t') \rangle = \min(t, t') = \langle W_2(t)W_2(t') \rangle \quad (5.4b)$$

$$\langle W_1(t)W_2(t') \rangle = 0 \quad (5.4c)$$

The amplitude of the particle's motion is given in terms of the position  $q$  and momentum  $p$  as

$$\epsilon = \sqrt{\frac{1}{2}m\Omega_0^2 q^2 + \frac{1}{2m}p^2} \quad (5.5)$$

The energy is  $E = \epsilon^2$ . The laser intensity fluctuations are presumed to be a weak perturbation to the oscillator's dynamics. A small change in energy will result from small changes to position  $dq$  and momentum  $dp$ . The infinitesimal change in amplitude is given by

$$d\epsilon = \frac{\partial \epsilon}{\partial q}(dq) + \frac{\partial \epsilon}{\partial p}(dp) + \frac{1}{2} \frac{\partial^2 \epsilon}{\partial q^2}(dq)^2 + \frac{1}{2} \frac{\partial^2 \epsilon}{\partial p^2}(dp)^2 \quad (5.6)$$

We saw from the conditions on  $W_i$  that  $\langle W_i(t)W_i(t') \rangle = \min(t, t')$ , which means that  $(dW_i)^2 \sim dt$ . In the following expansion, we retain terms of order

up to and including  $dt$  and neglect the orders  $(dt)^{3/2}$  and higher. Then the infinitesimal amplitude change is

$$\begin{aligned} d\epsilon &= \frac{p}{2m\epsilon} ((-\gamma p - \zeta_0 m \Omega_0^2 \cos(\Omega_m t) q) dt \\ &\quad + \sqrt{2m\gamma k_B T_0} dW_1 + m\Omega_0^2 \eta_0 q dW_2) \\ &\quad + \frac{q^2 \Omega_0^2}{8\epsilon^3} (2m\gamma k_B T_0 (dW_1)^2 + (m\Omega_0^2 \eta_0 q)^2 (dW_2)^2) \end{aligned} \quad (5.7)$$

To obtain the slowly-varying dynamics, we deterministically average the oscillating terms and stochastically average the random variations by integrating over one oscillation period ( $\tau = 2\pi/\Omega_0$ ) to obtain the weak change in energy in that time, or  $\Delta\epsilon = \int_0^\tau dt$ , given by

$$\begin{aligned} \Delta\epsilon &= -\gamma \int_0^\tau \frac{p^2}{2m\epsilon} dt - \zeta_0 m \Omega_0^2 \int_0^\tau \frac{\cos(\Omega_m t) qp}{2m\epsilon} dt \\ &\quad + \sqrt{2m\gamma k_B T_0} \int_0^\tau \frac{p}{2m\epsilon} dW_1 + m\Omega_0^2 \eta_0 \int_0^\tau \frac{pq}{2m\epsilon} dW_2 \\ &\quad + \frac{1}{4} m\gamma k_B T_0 \Omega_0^2 \int_0^\tau \frac{q^2}{\epsilon^3} (dW_1)^2 + \frac{1}{8} (\Omega_0^3 m \eta_0)^2 \int_0^\tau \frac{q^4}{\epsilon^3} (dW_2)^2 \end{aligned} \quad (5.8)$$

On the short timescale of integration, we hold that the particle maintains its harmonic motion with amplitude  $A = \sqrt{2\epsilon^2/m\Omega_0^2}$ , such that the position and momentum are given by

$$q(t) = \epsilon \sqrt{2/m\Omega_0^2} \cos(\Omega_0 t + \varphi) \quad (5.9)$$

$$p(t) = \epsilon \sqrt{2m} \sin(\Omega_0 t + \varphi) \quad (5.10)$$

Although the feedback mechanism is still the phase-locked parametric modulation, we assume for the simplicity of the discussion that there is no phase error arising from limited measurement precision. The phase  $\varphi$  is meant to be a constant phase offset from the particle's motion.

Each of the integrals in Eq. 5.8 are given by

$$-\gamma \int_0^\tau \frac{p^2}{2m\epsilon} dt = -\gamma\epsilon\tau/2 \quad (5.11a)$$

$$-\zeta_0 m \Omega_0^2 \int_0^\tau \frac{\cos(\Omega_m t) q p}{2m\epsilon} dt = -\zeta_0 \epsilon \Omega_0 \sin(2\phi) \tau / 4 \quad (5.11b)$$

$$\sqrt{2m\gamma k_B T_0} \int_0^\tau \frac{p}{2m\epsilon} dW_1 = (\gamma k_B T_0 / 2)^{1/2} W_1(\tau) \quad (5.11c)$$

$$m \Omega_0^2 \eta_0 \int_0^\tau \frac{pq}{2m\epsilon} dW_2 = (\epsilon^2 \eta^2 \Omega_0^2 / 8)^{1/2} W_2(\tau) \quad (5.11d)$$

$$\frac{1}{4} m \gamma k_B T_0 \Omega_0^2 \int_0^\tau \frac{q^2}{\epsilon^3} (dW_1)^2 = k_B T_0 \gamma \tau / 4\epsilon \quad (5.11e)$$

$$\frac{1}{8} (\Omega_0^3 m \eta_0)^2 \int_0^\tau \frac{q^4}{\epsilon^3} (dW_2)^2 = 3 \Omega_0^2 \eta_0^2 \epsilon \tau / 16 \quad (5.11f)$$

Here,  $W_i(\tau)$  are Wiener processes at  $\tau$  indicating a Gaussian random variable with variance  $\tau$ . The integrated Wiener process terms  $W_i(\tau)$  result from the fact that the correlation of  $p$  with  $dW_1$  and with  $dW_2$  causes the fluctuational terms to have non-zero averages.

Combining the distinct contributions, the infinitesimal change in amplitude is given by

$$\Delta\epsilon = \left( -\frac{1}{2}\gamma\epsilon - \frac{1}{4}\epsilon\zeta_0\Omega_0 \sin(2\phi) + \frac{1}{4} \frac{k_B T_0 \gamma}{\epsilon} + \frac{3}{16} \Omega_0^2 \eta_0^2 \epsilon \right) \tau \quad (5.12)$$

$$+ \sqrt{\gamma k_B T_0 / 2} W_1(\tau) + (\epsilon \eta_0 \Omega_0 / \sqrt{8}) W_2(\tau)$$

The timescale  $\tau$  is defined to be shorter than the relaxation time  $\tau_\gamma = 2\pi/\gamma$  yet faster than the oscillation cycle time  $\tau_{\Omega_0} = 2\pi/\Omega_0$ . As the energy change over  $\tau$  is small, the stochastic differential equation for the amplitude is

$$d\epsilon = \left( -\frac{1}{2}\gamma\epsilon - \frac{1}{4}\epsilon\zeta_0\Omega_0 \sin(2\phi) + \frac{1}{4} \frac{k_B T_0 \gamma}{\epsilon} + \frac{3}{16} \Omega_0^2 \eta_0^2 \epsilon \right) dt \quad (5.13)$$

$$+ \sqrt{\gamma k_B T_0 / 2} dW_1 + (\epsilon \eta_0 \Omega_0 / \sqrt{8}) dW_2$$

### 5.2.1 Fokker-Planck Equation for Intensity Noise

The form of Eq. 5.13 is a generalized Langevin equation. To understand the influence of laser noise on the particle's steady-state dynamics, we first compute the Fokker-Planck equation for the probability density, or  $P(\epsilon, t)$ , which equals [93]

$$\begin{aligned} \frac{\partial P(\epsilon, t)}{\partial t} = & -\frac{\partial}{\partial \epsilon} \left[ \left( -\frac{1}{2}\gamma\epsilon - \frac{1}{4}\zeta_0\Omega_0 \sin(2\varphi)\epsilon + \frac{1}{4}\frac{k_B T_0\gamma}{\epsilon} + \frac{1}{4}\Omega_0^2\eta_0^2\epsilon \right) P(\epsilon, t) \right] \\ & + \frac{\partial^2}{\partial \epsilon^2} \left[ \left( \frac{1}{4}k_B T_0\gamma + \frac{1}{16}\eta_0^2\Omega_0^2\epsilon^2 \right) P(\epsilon, t) \right] \end{aligned} \quad (5.14)$$

The form of Eq. 5.14 comprises of drift terms

$$D_1(\epsilon) = -\frac{1}{2}\gamma\epsilon - \frac{1}{4}\zeta_0\Omega_0 \sin(2\varphi)\epsilon + \frac{1}{4}\frac{k_B T_0\gamma}{\epsilon} + \frac{1}{4}\Omega_0^2\eta_0^2\epsilon \quad (5.15)$$

and diffusion terms

$$D_2(\epsilon) = \frac{1}{4}k_B T_0\gamma + \frac{1}{16}\eta_0^2\Omega_0^2\epsilon^2 \quad (5.16)$$

The drift terms include the ambient gas damping  $\gamma$  and the feedback cooling  $\zeta_0$ . The additional two terms arise from the stochastic average. The damping term  $-\gamma\epsilon/2$  and the thermal term  $k_B T_0\gamma/4\epsilon$  are a manifestation of the fluctuation and dissipation theorem [31], which tells us that the amplitude will decay with  $\gamma$  but the fluctuations will drive it up again; over time, they will reach equilibrium. The laser noise drift term ( $\eta_0^2\Omega_0^2\epsilon$ ) is linear in amplitude, which means that like the gas damping and feedback, its influence is stronger at larger amplitudes. Its sign, however, is opposite the gas damping and feedback (when  $\varphi = -\pi/4$ ), which means that it causes the amplitude to grow rather than decay.

The thermal diffusion term ( $k_B T_0\gamma/4$ ) is a constant source of energy and will always drive the particle's motion. The laser diffusion term ( $\eta_0^2\Omega_0^2\epsilon^2/16$ ) is quadratic in  $\epsilon$ , which is characteristic of multiplicative noise processes [118]. If the laser noise is too large, the oscillation amplitude may become too large and result in an instability in the trap.

### 5.2.2 Stationary Amplitude Distribution

To solve the Fokker-Planck equation, we have to identify boundary conditions. For stable trapping, we assume a steady-state exists such that  $\lim_{t \rightarrow \infty} \partial P(\epsilon, t) / \partial t = 0$ . This means that a time-independent probability distribution,  $P_s(\epsilon)$ , exists that is the solution to

$$\frac{d}{d\epsilon} \left[ D_1(\epsilon) P_s(\epsilon) - \frac{d}{d\epsilon} (D_2(\epsilon) P_s(\epsilon)) \right] = 0 \quad (5.17)$$

which is written as  $\frac{dj_s}{d\epsilon} = 0$  for probability current  $j_s(\epsilon) = [D_1(\epsilon) - \frac{d}{d\epsilon} D_2(\epsilon)] P_s(\epsilon)$ . The solution to this is  $j_s(\epsilon) = \text{const.} \equiv j^*$  for all  $\epsilon$ . If the energy lies within the interval  $[a, b]$ , then  $j_s(a) = j_s(b) = j^*$ . We restrict the energy amplitude to being positive, or  $\epsilon \geq 0$ , which means there is zero probability flux through the boundary  $\epsilon = 0$ .

As a result,  $j_s(0) = 0$ , from which we deduce  $j_s(\epsilon) = 0$ . This simplifies the differential equation to first order, or

$$0 = - \left( \frac{\gamma\epsilon}{2} - \frac{\zeta_0 \Omega_0}{4} \sin(2\varphi) \epsilon - \frac{k_B T_0 \gamma}{4\epsilon} + \frac{1}{8} \eta_0^2 \Omega_0^2 \epsilon \right) P_s(\epsilon) \quad (5.18)$$

$$- \left( \frac{1}{4} k_B T_0 \gamma + \frac{1}{16} \eta_0^2 \Omega_0^2 \epsilon^2 \right) \frac{dP_s(\epsilon)}{d\epsilon}$$

Setting  $\eta_0 = 0$  in Eq. 5.18 and then solving for  $P_s(\epsilon)$  recovers the Maxwell-Boltzmann distribution.

An analytical solution to this equation exists when  $\eta \neq 0$  in the form of a  $q$ -exponential [128], which gives the following stationary probability distribution for the amplitude

$$P_s(\epsilon) = \frac{1}{Z_\epsilon} \epsilon (4k_B T_0 \gamma + \eta_0^2 \Omega_0^2 \epsilon^2)^{\alpha_\epsilon} \quad (5.19a)$$

$$\alpha_\epsilon = \frac{1}{1 - q} \quad (5.19b)$$

$$q = \frac{8\gamma + 4\zeta_0 \Omega_0 \sin(2\varphi) + \eta_0^2 \Omega_0^2}{8\gamma + 4\zeta_0 \Omega_0 \sin(2\varphi) - \eta_0^2 \Omega_0^2} \quad (5.19c)$$

where  $Z_\epsilon$  is a normalization constant.



Recall that  $E = \epsilon^2$ . We obtain an energy distribution by substituting  $P_s(\epsilon) d\epsilon = P(E) dE/2\epsilon$ , which equals

$$P(E) = \frac{1}{Z_\epsilon} (2k_B T_0 \gamma + \frac{1}{2} \eta_0^2 \Omega_0^2 E)^{\alpha_\epsilon} \quad (5.20)$$

This energy distribution is different from the traditional Maxwell-Boltzmann form because of the multiplicative noise. When  $E$  or  $\eta_0$  are large, a steady-state may not exist and this distribution would diverge.

### 5.2.3 Trapping Stability Condition

In order for the probability distribution to not diverge, the exponent should always be negative, or

$$\eta_0^2 < (8\gamma + 4\zeta_0 \Omega_0 \sin(2\varphi)) / \Omega_0^2 \quad (5.21)$$

The spectral density of the power fluctuations  $\eta_0^2$  must remain below  $8\gamma/\Omega_0^2$  for the trap to remain stable, which is incredibly prohibitive at very low vacuum pressures. When the feedback phase is tuned to  $\varphi = \pi/4$ , we find the added feedback gain alleviates the restriction on trap stability. The condition in Eq. 5.21 is akin to the Routh-Hurwitz criterion for the assumption of linear time invariance in a control system. It conveys when the assumption of frequency noise as a first-order perturbation breaks down.

Different from thermal fluctuations or recoil heating, we find that the contribution from classical laser fluctuations scales with  $E$ . At large energies (or large phonon occupations), classical fluctuations affect the particle's dynamics. Feedback, however, counters the influence of laser fluctuations and lowers the center of mass amplitude.

In Eq. 5.13, we substitute  $2\epsilon d\epsilon = dE$ .

$$\begin{aligned} \frac{dE}{dt} = & \left( -\gamma - \frac{1}{2} \zeta_0 \Omega_0 \sin(2\varphi) + \frac{3}{8} \Omega_0^2 \eta_0^2 \right) E + \frac{1}{2} k_B T_0 \gamma \\ & + \sqrt{E} \sqrt{\gamma k_B T_0} dW_1 + E \eta_0 \Omega_0 / \sqrt{2} dW_2 \end{aligned} \quad (5.22)$$

When we take a time average of Eq. 5.22, we note  $\langle dW_i \rangle = 0$  and that the

average energy  $\langle E \rangle = \bar{n} \hbar \Omega_0$ . As a result, we arrive at an equation for the time rate of change of the average phonon number, or

$$\dot{\bar{n}} = \left( -\gamma - \frac{1}{2} \zeta_0 \Omega_0 \sin(2\varphi) + \frac{3}{8} \Omega_0^2 \eta_0^2 \right) \bar{n} + k_B T_0 \gamma / \hbar \Omega_0 \quad (5.23)$$

Solving this differential equation, we find the steady-state solution for the average occupation number. With feedback cooling turned off, this is given by

$$\bar{n}_\infty = \frac{k_B T_0}{\hbar \Omega_0} \frac{\gamma}{\gamma - 3\eta_0^2 \Omega_0^2 / 8} \quad (5.24)$$

The minus sign in the denominator of Eq. 5.24 is most telling. Intensity fluctuations heat up the trap such that as one goes lower in pressure, the steady-state center of mass temperature may automatically increase and equilibrate to a level higher than room temperature. For this reason, feedback control is needed if not to cool the particle, to stabilize its motion.

From Eq. 5.23, we find that the reheating rate due to laser intensity fluctuations is proportional to the oscillator's energy, or

$$\Gamma_{\text{RIN}} = \frac{3}{8} \Omega_0^2 \eta_0^2 \bar{n} \quad (5.25)$$

The reheating rate is not dependent on the particle's mass, unlike the recoil heating rate, and can be suppressed with parametric feedback cooling. In the following sections, we present experimental tests of classical noise injection and suppression when the particle is brought to the recoil limit in order to quantify the classical noise contribution for our system.

### 5.3 Experimental Results

In this section, we present our experimental results for the characterization of, injection, and attenuation of laser intensity noise. For the purpose of accurately diagnosing laser intensity fluctuations, a homebuilt photodetector capable of handling up to 100 mW of optical power with a bandwidth exceeding 1 MHz was built (as described in Appendix D).

### 5.3.1 Characterizing Intensity Noise

The output of the laser is guided through several optics, a Pockels' cell, and then into a single-mode polarization maintaining optical fiber (PMF) that is fixed to the vacuum chamber. As shown in Fig. 2.9, the collimated fiber output is deflected to a single-port photodetector with an in-built, low noise current source. The detected photocurrent is thus  $\delta i(t)$ , which contains the fluctuations on the laser beam with the DC level subtracted away. Because the detected power is from a PMF, the signal is a combination of classical intensity fluctuations, shot noise, pointing instability, polarization drift, and spatial mode distortion all converted into an intensity fluctuation.

The detected fluctuations are composed of classical noise and shot noise, or  $\delta i(t) = \delta i_{\text{cl}}(t) + \delta i_{\text{sn}}(t)$ . The autocorrelation of this signal is

$$\langle \delta i(t) \delta i(t') \rangle = \langle \delta i_{\text{cl}}(t) \delta i_{\text{cl}}(t') \rangle + \langle \delta i_{\text{sn}}(t) \delta i_{\text{sn}}(t') \rangle \quad (5.26)$$

where  $\langle \delta i_{\text{sn}}(t) \delta i_{\text{sn}}(t') \rangle = 2e\bar{i}_{\text{ph}}\delta(t-t')$ . The power spectral density for current fluctuations is given by

$$S_{\text{II}}(\Omega) = \frac{1}{2\pi} \int_{-\infty}^{\infty} dt' e^{i\Omega t'} \langle \delta i(t) \delta i(t') \rangle \quad (5.27)$$

We normalize  $S_{\text{II}} = S_{\text{cc}} + S_{\text{ss}}$  by the squared average DC photocurrent  $i_{\text{ph}}^2 = (\mathcal{R}P_0)^2$ , where  $P_0$  is the incident power and  $\mathcal{R}$  is the detector responsivity in [A/W]. Then, the measured relative intensity fluctuations are given by

$$S_{\text{ff}}(\Omega) = S_{\text{RR}}(\Omega) + \frac{e}{\pi\mathcal{R}P_0} \quad (5.28)$$

for  $S_{\text{cc}}(\Omega) = (\mathcal{R}P_0)^2 S_{\text{RR}}$ . This expression gives us the relative intensity fluctuations at any optical power. At very low optical powers, the relative fluctuations are dominated by the laser's shot noise. At higher optical powers, however, the relative contribution of shot noise decreases and the noise power is dominated by classical fluctuations. Their contributions are equal at  $P_0 = e/\pi\mathcal{R}S_{\text{RR}} = e/\mathcal{R}\eta_0^2$ .

Shown in Fig. 5.1 are the relative intensity fluctuations at  $P_0 = 6.7$  mW of optical power over a broad range of frequencies while a trapped particle is

under feedback. It is the averaged PSD of  $10^3$  time traces of 1 sec in length sampled at 625 kSa/sec. The intensity fluctuations have been converted to a logarithmic scale such that the units are in dB/Hz. The domain of frequencies relevant to this experiment are between 10 and 300 kHz, where the relative intensity noise is  $S_R(2f_y) = 10^{-13.8}/\text{Hz}$ .

There are a handful of distinguishing peaks in the spectrum shown in Fig. 5.1. At frequencies lower than 1 kHz, the spectrum has the signature  $1/f$  noise floor. At 1.1 kHz is the vacuum turbopump rotation frequency. Between 10 kHz and 300 kHz, the spectrum is mostly flat, save for two peaks at 100 kHz and 240 kHz which represent part of the feedback signal in  $z$  and  $x$ .

Classical intensity fluctuations act as an additional source of reheating in the system. Their contribution, however, is proportional to the oscillator's occupation number. At occupations of  $n = 100$  or lower, the reheating due to classical intensity fluctuations would be given by

$$\Gamma_{\text{RIN}} = \pi \frac{3}{8} \Omega_0^2 S_{\text{RR}} n = 0.13 \text{ Hz} \quad (5.29)$$

when  $\Omega = 2\pi 150 \text{ kHz}$ .

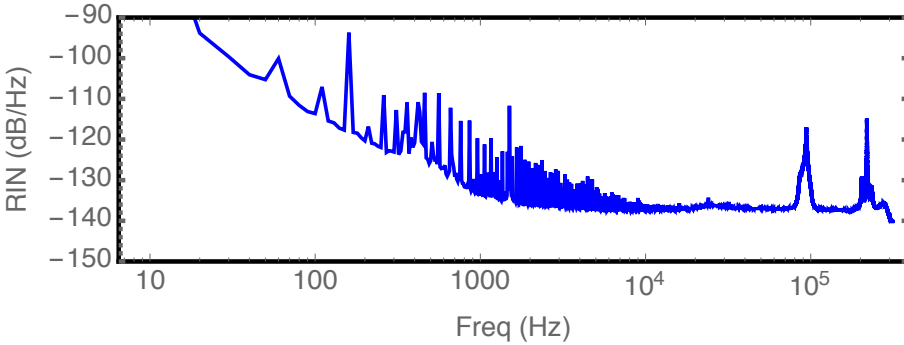


**Figure 5.1:** A plot of the laser's relative intensity noise at  $P_0 = 6.7 \text{ mW}$  as a function of frequency as a single-sided power spectral density, or  $S_R(2f)$ ; divide by  $4\pi$  to obtain  $S_{\text{RR}}(\Omega)$ . The spectrum contains several features, which are explained in the main text.

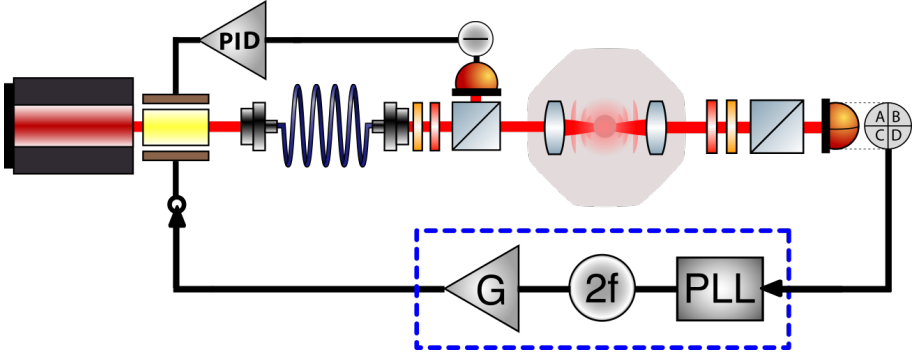


**Figure 5.2: Schematic of intensity stabilization and feedback switching.** Intensity noise is measured on a high power photodetector with a built-in PID controller to actuate the EOM. Separately, a PLL tracks the particle’s oscillation and is used to generate a feedback control signal that is also applied to the EOM. The feedback control is switched on and off during reheating experiments.

### 5.3.2 Injecting and Removing Intensity Noise from the Trap

Despite quantitative estimates suggesting little contribution of the classical intensity noise to reheating in the trap, we test their contribution to the motional dynamics under four different laser noise configurations.

A particle with measured size  $R = 68$  nm was trapped with  $P_0 = 60$  mW of focal power and brought to  $P_{\text{gas}} = 3 \times 10^{-8}$  mbar of pressure using phase-based feedback. With an initial occupation in  $y$  below  $n_y = 100$ , the particle was released from feedback in just the  $y$ -axis and its reheating was measured over 100 msec. The experiment was repeated over 1000 times, where each time the same initial occupation  $\bar{n}_0$  was established by the phase-based feedback as illustrated in Fig. 5.2. After switching off the feedback, the particle was tracked as it evolved from  $\bar{n}_0$  to  $\bar{n}_t$  within time  $t$ . Along each 100 msec trajectory the particle’s position was sampled at a rate of 625 kHz and, from integrating over 1 msec of motion, the energy was computed. The average energy increases monotonically. Owing to the particle’s small dimensionality and the stochastic nature of the reheating process, however, a single trajectory may deviate from the ensemble average considerably [91].

Plotted in Fig. 5.3 is the ensemble averaged reheating curve under the

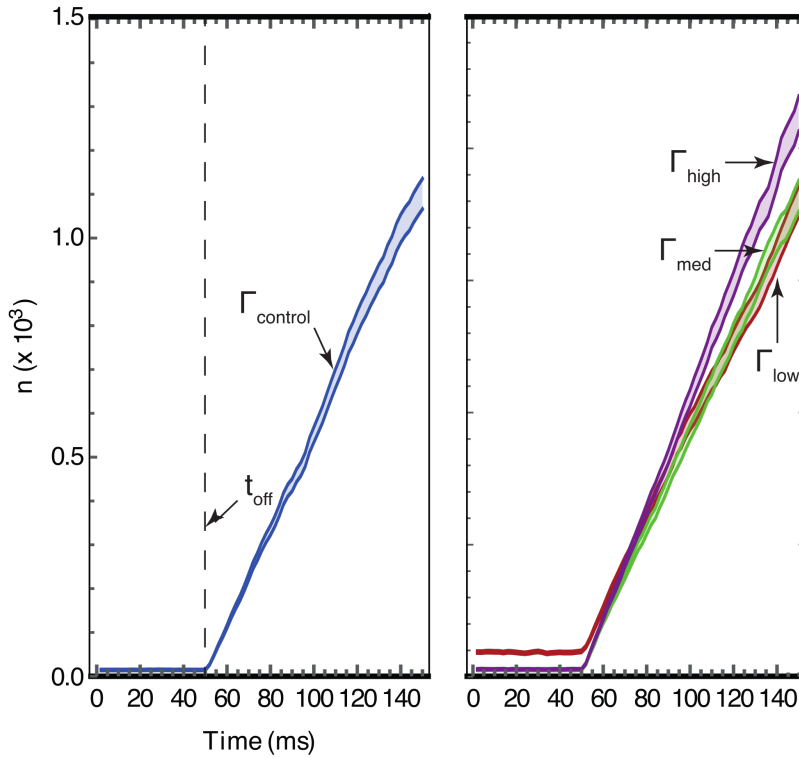


**Figure 5.3: Reheating under laser intensity control.** Reheating in the  $y$ -axis under four different configurations of the laser intensity fluctuations. Plotted is the mean phonon occupation with one standard deviation above and below the mean as computed over 1000 realizations of this experiment.  $t_{\text{off}}$  indicates the time at which the feedback is turned off. On the left are the native laser intensity fluctuations in blue and the reheating  $\Gamma_{\text{control}}$ . On the right are under reduced laser noise in crimson ( $\Gamma_{\text{low}}$ ); with weak noise injected in green ( $\Gamma_{\text{med}}$ ); and with stronger noise injected in purple ( $\Gamma_{\text{high}}$ ).

native laser fluctuations. The plot shows the average phonon number along with one standard deviation about the mean. The standard deviation grows with  $\bar{n}$  because the position fluctuations grow with energy. The initial phonon occupation is  $\bar{n}_0 = 14.2 \pm 0.2$  and the measured reheating rate as obtained from the slope is  $\Gamma_{\text{control}} = 10.9 \pm 1.7$  kHz.

Next, the laser intensity noise is reduced over a bandwidth of DC to 300 kHz using the laser noise eater from  $\mathcal{S}_{\text{R}}^{\text{control}} = 1.87 \times 10^{-14}$  /Hz to  $\mathcal{S}_{\text{R}}^{\text{low}} = 0.12 \times 10^{-14}$  /Hz. The laser noise eater is designed to stabilize the DC power and counteract laser intensity fluctuations; as it actuates the same Pockels' cell that is used for feedback control, the initial temperature is slightly larger. The initial phonon occupation is  $\bar{n}_{\text{low}} = 53.3 \pm 1.2$  and the measured reheating rate is  $\Gamma_{\text{low}} = 9.8 \pm 1.4$  kHz. Comparing to the control, the rate decreased by at most 10% despite 15.7 times reduction in the noise and a higher initial phonon occupation under laser stabilization.

Using white noise sourced from a function generator, the laser noise was increased to  $\mathcal{S}_{\text{R}}^{\text{med}} = 3.2 \times 10^{-14}$ /Hz, resulting in a reheating rate  $\Gamma_{\text{med}} = 10.6 \pm 0.7$  kHz. Further increasing the noise to  $\mathcal{S}_{\text{R}}^{\text{high}} = 6.5 \times 10^{-14}$ /Hz raised the reheating rate to  $\Gamma_{\text{high}} = 12.3 \pm 0.9$  kHz. The initial phonon occupations were  $n_{\text{med}} = 14.7 \pm 0.2$  and  $n_{\text{high}} = 15.7 \pm 0.2$ . In both cases, the feedback gain was kept constant.

Since the composite reheating is  $\Gamma_t = \Gamma_{\text{rec}} + \Gamma_{\epsilon}$ , we determine the zero-noise limit of reheating under photon recoil through linear interpolation. The estimated recoil heating rate is  $\Gamma_{\text{rec}} = 9.6$  kHz and indicates that classical noise fluctuations contribute no more than  $(\Gamma_{\text{control}} - \Gamma_{\text{rec}})/\Gamma_{\text{control}} = 11.9 \pm 6.4\%$  to the residual mechanical motion under the base fluctuations of the laser.

Plotted in Fig. 5.4 are the different laser intensity noise profiles as measured during each of the reheating measurements above. The particle is susceptible to classical noise fluctuations at the parametric frequency  $2\Omega_y$ , which is why it causes the energy amplitude to diffuse with  $\epsilon^2$ . A quantum mechanical interpretation of this behavior suggests that two mechanical phonons are injected at a time into the oscillator by classical intensity fluctuations [111].

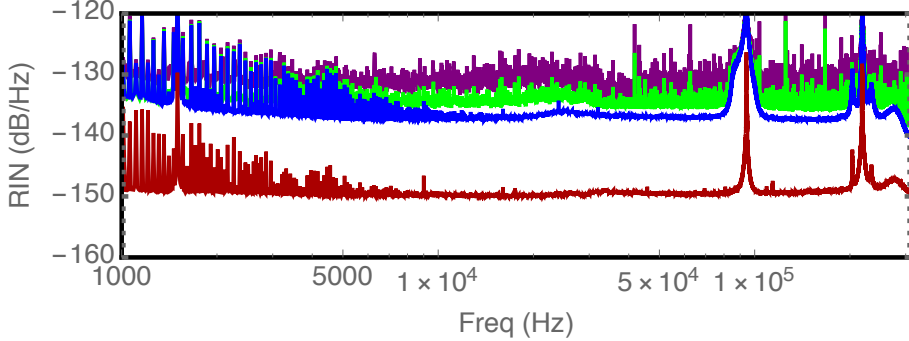


**Figure 5.4:** The relative intensity noise levels under the four experimental configurations are shown as a single-sided power spectral density, or  $S_R(f)$ ; divide by  $4\pi$  to obtain  $S_{RR}(\Omega)$ . In blue, the laser noise floor is replotted from Fig. 5.1. The colors correspond to the four reheating experiments of Figs. 5.3.

### 5.3.2.1 Strong-Focusing Corrections

The noise-free recoil heating rate is  $\Gamma_{\text{rec}} = 9.6$  kHz. Recall that the recoil heating rate is  $\Gamma_{\text{rec}} = P_{\text{sc}}\omega_0/(5mc^2\Omega_0)$ , which for the parameters of this system is  $\Gamma = 27.2$  kHz, roughly a factor 2.5 times larger. The recoil heating formula was derived under a paraxial approximation, which is for small focusing angles. The trap, however, is formed from a high numerical aperture lens with which the beam waist is actually larger, owing to diffractive effects. For an objective with  $\text{NA} = 0.90$ , the waist is 1.7 times larger than the paraxial estimate at  $\lambda = 1064$  nm. Using this difference to compute the focal intensity, we find the theoretical recoil rate is  $\Gamma_{\text{rec}} = 9.4$  kHz, which has quantitative agreement with the measured rates.

### 5.3.3 Discussion

The measurements demonstrate two important findings. First, classical intensity noise can be suppressed using laser stabilization techniques to a level of  $0.12 \times 10^{-14}/\text{Hz}$  or  $-150$  dB/Hz, which is comparable to advanced stabilization protocols developed for gravitational wave detectors [129, 130]. The stabilization was carried out using just  $P_0 = 6.7$  mW of power; the detector is designed



to handle up to 100 mW, which means we may reduce laser fluctuations further to a shot-noise limited value of  $\mathcal{S}_s = -176.8$  dB/Hz. In contrast to established stabilization methods, noise suppression was achieved over 500 kHz, which is more than two orders of magnitude larger than previously reported.

Second, feedback cooling the particle to low phonon occupations countered the laser fluctuations. If the reheating time were extended so that the particle reaches larger amplitude, the difference between  $\Gamma_{\text{control}}$  and  $\Gamma_{\text{low}}$  would be more apparent.

## 5.4 Frequency Stability

Intensity fluctuations and drifts are critical experimental challenges in a variety of opto- and electro-mechanical systems [122, 131]. On one hand, laser intensity noise may heat up the mechanical oscillator if it is too strong and not properly stabilized. On the other hand, laser intensity fluctuations may artificially broaden the oscillation linewidth if occurring on a timescale shorter than the relaxation time. They have been shown to corrupt force measurements in atomic-force microscopy by thermal expansion and radiation pressure-induced frequency jitter [132]. Drifts in the center frequency arising from power fluctuations may occur faster than the bandwidth of the PLL but slower than the particle oscillation, which would increase the phase error in the feedback loop and unintentionally heat up the particle.

Levitated opto-mechanics are premised on the fact that the lack of a clamping mechanism overcomes the usual material limits to Q-factors when the particle is brought into UHV. Though we showed that the intrinsic damping is limited by recoil heating, the estimated Q-factor is still approximately  $10^8$ , which is considerably higher than other opto-mechanical devices. The Q-factor corresponds to the free-running oscillator without feedback. At the particle's thermal amplitude, laser noise is sure to kick in and affect the motional frequency. For applications in force sensing this may be detrimental to proposed  $z\text{N}/\text{Hz}^{1/2}$  sensitivity estimates\*.

---

\* $z\text{N} = 10^{-21}$  N

### 5.4.1 Characterizing frequency fluctuations

Next, we track frequency fluctuations under weak feedback and quantify their correlation to laser intensity fluctuations. Activating the laser noise eater, we compare frequency stability at similar center of mass temperatures. Finally, we estimate the opto-mechanical limits to frequency stability and force sensitivity.

The motional frequency  $\Omega_0$  is determined from traces of the particle's motion measuring 1.0 sec in length. Each trace is broken up into moving segments of 40 msec length, which is comparable to the feedback-cooled relaxation time, or  $\gamma_{\text{fb}}^{-1}$ ; the power spectral density is computed; and the frequency is obtained from a Lorentzian fit. The measurement is repeated 50 times in each. Plotted in Fig. 5.5 are histograms of the frequency with the mean subtracted away. A more standard means of assessing frequency fluctuations uses the technique of Allan variance. Due to the limited sampling time, we were not able to resolve the Allan variance for low frequencies.

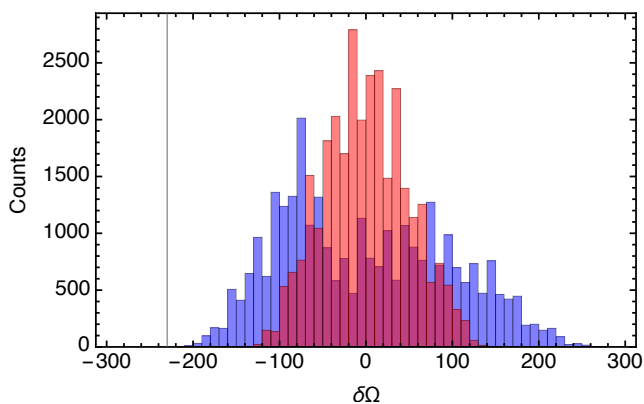


**Figure 5.5: Frequency fluctuations over 1 minute.** Plotted are the center of mass frequency fluctuations under feedback control. In blue are the fluctuations under the native laser noise and in red are those with laser stabilization activated. A histogram of frequency is calculated with the mean across each measurement set subtracted away. The total acquisition time is 50 sec of the particle's oscillation sampled at 625 kSa/sec; the center frequency is determined based on Lorentzian fits to the power spectral density of moving average segments measuring 40 msec in length and spaced 1.6 msec apart.

### 5.4.2 Correlation to Intensity Noise

The laser intensity fluctuations are tracked simultaneously with the particle's motion. The variance of total laser noise is computed in the same time interval used to determine the center frequency. Plotted in Fig. 5.6 are density plots of the variance in intensity versus the center frequency drift. The bright regions indicate frequent occurrence and dark regions are seldom. The variance in total intensity has been reduced by 14.3 dB and with it the variance in frequency by 6.0 dB. The distribution without laser stabilization leans left of zero because the feedback modulation depth is slightly less than in the stabilization case; non-linearities in the potential pull at the center frequency and shift it downward [101]. This makes the distribution slightly asymmetric.

Slow drifts in the center frequency would artificially broaden the oscillator's linewidth and limit integration times over which forces could be measured with

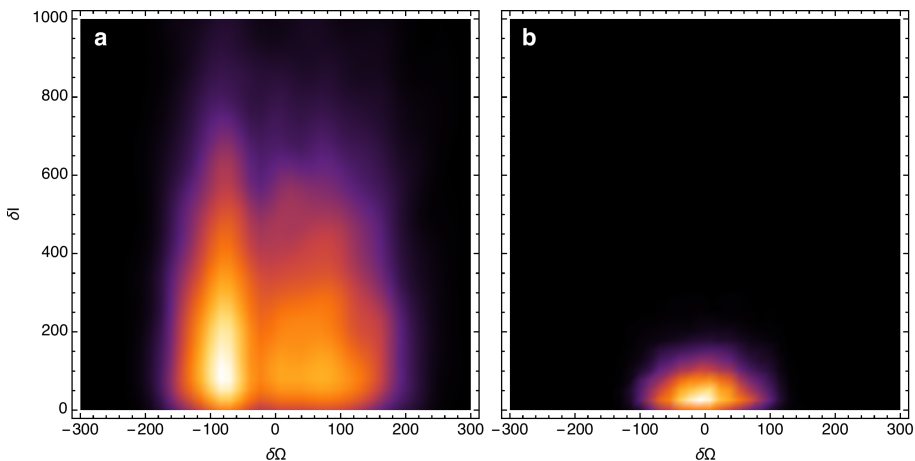


**Figure 5.6: Correlating frequency and intensity fluctuations.**

Density plots of the variance in intensity versus frequency fluctuations under the native laser fluctuations (a) and with laser stabilization (b). The total acquisition time is 50 sec. Here, the mean values across the entire measurement have been subtracted away to emphasize the drifts in intensity and frequency. Intensity fluctuations are measured with 2.5 mW of power coupled to the photodetector. Frequency fluctuations are measured exactly as in Fig. 5.5.

a levitated nanoparticle. In the next section, we calculate the limit to force sensitivity induced by laser intensity fluctuations. While the laser may introduce a frequency jitter, additional sources arise from back-reflections coupling into the optical trap, heating of the microscope objective, and slow drifts in the coupling of light into the optical trap via the polarization-maintain fiber.

### 5.4.3 Opto-mechanical Limit

Fluctuations in intensity that couple to the spring constant raise the particle's effective temperature from  $T_0 \rightarrow T_0/(1-3\eta_0^2\Omega_0^2/8\gamma)$ , where  $\eta_0^2 = \pi S_{RR}$ . Here, we show that multiplicative noise from laser intensity fluctuations corrodes the particle's force sensitivity. Following Bourret [133], we rewrite the original equation of motion as

$$m\ddot{x} + m\gamma\dot{x} + kx = G(t) \quad (5.30)$$

with an effective thermal force equal to

$$G(t) = F_{\text{th}}(t) - m\Omega_0^2\eta(t)x(t) \quad (5.31)$$

Computing the autocorrelation of this force, we maintain that the two noise sources are uncorrelated and independent from  $x(t)$ . Assuming that  $\eta_0^2$  is small enough that we haven't exceeded the domain of stability (c.f. Eq. 5.21), the autocorrelation is given by

$$\begin{aligned} \langle G(t)G(t') \rangle &= \langle F_{\text{th}}(t)F_{\text{th}}(t') \rangle + m^2\Omega_0^4 \langle \eta(t)\eta(t') \rangle \langle x^2 \rangle \\ &= (2m\gamma k_B T_0 + 2m^2\Omega_0^4\eta_0^2 \langle x^2 \rangle) \delta(t - t') \end{aligned} \quad (5.32)$$

The power spectral density of this force is given by

$$S_{GG}[\Omega] = (m\gamma k_B T_0 + m^2\Omega_0^4\eta_0^2 \langle x^2 \rangle) / \pi \quad (5.33)$$

Thermal fluctuations and frequency jitter correspond to a noise background above which a force is measured. Integrating the force noise in measurement

time  $\tau_F$ , the minimum detectable force is

$$F \geq \sqrt{S_{GG}/\tau_F} = [(m\gamma k_B T_0 + m^2 \Omega_0^4 \eta_0^2 \langle x^2 \rangle) / \pi \tau_F]^{1/2} \quad (5.34)$$

Laser intensity fluctuations attenuate force sensitivity by raising the thermal noise background. While using a levitated nanoparticle as a force sensor profits from a very small mass  $m$  and incredibly weak damping  $\gamma$  in its free-running state, applications in force sensing will require added levels of control to the laser intensity noise even though it is not a limitation for ground-state cooling.

Laser intensity fluctuations have not only a classical but also a quantum origin [134]. The random arrival time of photons in effect generates a noisy intensity, which also introduces frequency noise. The power spectral density of photon fluctuations is  $S_{PP} = \hbar\omega_0 P_0 / 2\pi$ . When it is normalized by optical power, the relative noise from photon shot noise is  $S_{RR}^P = \hbar\omega_0 / (2\pi P_0)$ . Thus, the noise strength is  $\eta_{ph}^2 = \hbar\omega_0 / (2P_0)$ . The force spectrum due to photon recoil is  $S_{rec}^F = \hbar\omega_0 P_{sc} / (5\pi c^2)$ , with which we find that the opto-mechanical limit to force sensitivity with a levitated nanoparticle is given by

$$\begin{aligned} F \geq \sqrt{S_{OM}/\tau_F} &= [(S_{rec}^F + m^2 \Omega_0^4 \eta_0^2 \langle x^2 \rangle) / \pi \tau_F]^{1/2} \\ &= \left[ \left( \frac{1}{5} + \pi \eta_{fs} \beta^2 \langle x^2 \rangle \right) \frac{\hbar\omega_0}{\pi c^2} P_{sc} / \pi \tau_F \right]^{1/2} \end{aligned} \quad (5.35)$$

where  $\beta = f_s NA^2 k / 2$  and  $\eta_{fs} = 3NA^2 / 2$  is the free-space single particle cooperativity [55]. Eq. 5.35 tells us that photon recoils limit force sensitivity and strong focusing of the laser field, which increases the cooperativity, may further affect this. These quantum fluctuations will cause the oscillator's phase to diffuse [33]; the phase fluctuations will be tracked by the PLL and fed back in order to counteract the frequency noise. Any force sensing protocol will require feedback control to hold the particle in the regime of linear stability and suppress frequency jitter [101]. For a particle with  $R = 68$  nm and  $P_{sc} = 17.5$   $\mu$ W, we estimate the recoil-limited force sensitivity to be  $S_{rec}^{FF} = 1.5 \times 10^{-21}$  N/Hz<sup>1/2</sup>.

Compared to existing force sensors [135], we achieve similar force sensitivities while operating at room temperature. This would alleviate the need for complex cryogenics typically used in advanced force sensing platforms.

## 5.5 Conclusion

The studies conducted in this chapter further support the claim that a levitated nanoparticle in UHV is in a regime of strong measurement backaction. We revisit the claim that levitated opto-mechanics will profit from boundless Q-factors by quantifying the contribution of laser intensity noise to reheating.

Limits to force sensitivity do indeed exist and are aggravated by the presence of laser noise. This is a unique challenge to the levitated opto-mechanics community that isn't present in other cavity opto-mechanical systems.

Advanced state estimation protocols, including Kalman filtering, can profit from the live, simultaneous readout of the laser noise to generate improved feedback cooling protocols. Laser filter cavities may also benefit the next generation of levitation in order to suppress intensity noise over a broader bandwidth.

# 6

---

## Resolving the Classical to Quantum Transition

The goal of this chapter is to quantify the current experimental limit of feedback cooling and develop sideband thermometry techniques to probe the transition from classical to quantum mechanical descriptions of the particle's motion.

### 6.1 Introduction

Having studied mechanisms of dissipation in the trap, we recognize that cooling the particle into the ground state is limited by the balance of feedback cooling, measurement imprecision, and recoil heating. Feedback cooling is used to suppress backaction from the trapping laser and thus contains a record of the field's quantum fluctuations. As such, the feedback is deemed 'quantum feedback' as it is being used to suppress motion resulting from measurement-induced backaction [15, 27, 136–138].

Feedback cooling, however, is limited by the measurement imprecision. Reducing measurement imprecision would enhance the feedback efficiency and cool the particle further. In this chapter, we first present experimental results from feedback cooling under improved measurement precision. Next, we

describe an alternate technique for determining the average phonon occupation under feedback cooling using heterodyne interferometry. Thereafter, we discuss sources of noise in phonon calibration and the implications of these experiments in probing the quantum behavior of motion. Finally, we conclude with an outlook.

## 6.2 The micro-Kelvin regime

The efficiency of feedback cooling depends on the information content of the measurement record. A trapped particle scatters part of the optical field as it moves around the focus. The scattered field's phase is directly correlated to the particle's position. Collecting more of the scattered field improves our detection efficiency  $\eta_c$  and consequently reduces measurement imprecision  $S_{\text{imp}}$ .

### 6.2.1 Reducing Measurement Imprecision

To improve measurement imprecision, the experimental setup was modified by replacing the collection lens with a higher NA asphere from Lightpath (with an effective NA = 0.77 at  $\lambda = 1064$  nm) and modifying the splitting ratio of the transmitted light. Instead of splitting light equally three ways, 90% of the transmitted light was sent to the  $y$ -axis detector and the remaining 10% was split between  $x$  and  $z$ . The focal power was slightly reduced to  $P_0 = 60$  mW. With the higher NA and the increased transmission for detection in  $y$ , the total detected optical power was  $P_{\text{det}} = 40$  mW, which exceeds the damage threshold for commercially available photodetectors. As a result, we designed and built our own balanced photodetectors using C30642GH InGaAs photodiodes from Excelitas, which have a damage threshold exceeding 100 mW, and a transimpedance amplifier based on the OPA656 operational amplifier. The detector bandwidth is 1 MHz.

The compromise of weak cooling in  $x$  and  $z$  yet enhanced precision in  $y$  was chosen because  $y$  has the highest oscillation frequency and thereby the highest ground state energy amongst the three axes. Because of its large oscillation frequency, it also experiences the weakest reheating due to measurement backaction (c.f. Eq. 4.27).



First the trapped particle was brought to  $P_{\text{gas}} = 3 \times 10^{-8}$  mbar. At this point the feedback gain was systematically increased to identify the temperature minimizing gain and the phase delay of the feedback signal was adjusted to compensate for electronic delay in cable lines and in the detection.

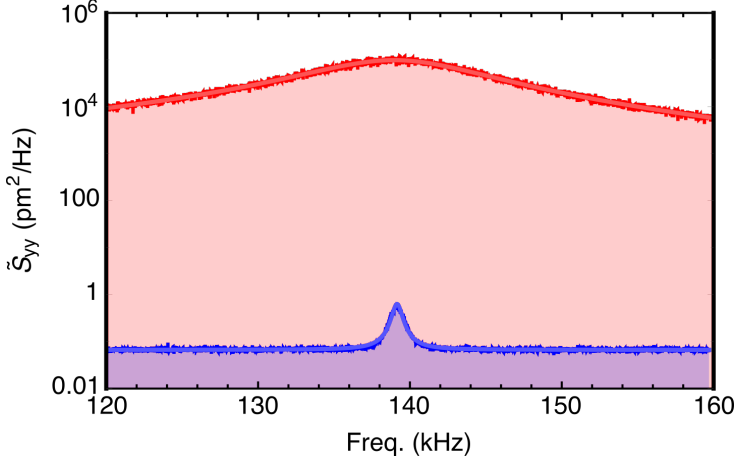


**Figure 6.1: Microkelvin Cooling.** Power spectral densities of the motion in  $y$  at two pressures,  $P_{\text{gas}} = 14.7$  mbar (in red) and  $P_{\text{gas}} = 3 \times 10^{-8}$  mbar (in blue). The spectra were computed based on 200 time traces measuring 100 msec in length and sampled at 625 kSa/sec.

Plotted in Fig. 6.1 are power spectral densities of the particle's motion at two different pressures. The blue spectrum is taken under feedback. At this point, the peak displacement is  $(\mathcal{S}_y(f_y))^{1/2} = 812.4 \text{ fm}/\sqrt{\text{Hz}}$  against an imprecision background of  $(\mathcal{S}_{\text{imp}})^{1/2} = 295.0 \text{ fm}/\sqrt{\text{Hz}}$  and linewidth of  $\gamma_{\text{fb}}/2\pi = 710 \text{ Hz}$ . The signal to noise ratio is 2.75. We calculate the contribution due to measurement backaction to be  $(\mathcal{S}_{\text{ba}}(f_y))^{1/2} = 714.1 \text{ fm}/\sqrt{\text{Hz}}$ , or 87.9% of the residual motion. The spectrum corresponds to a minimum phonon occupation of  $\bar{n}_y = 15.2 \pm 1.0$ , which equates to a center of mass motional temperature of  $T_y = 101.4 \pm 6.6 \mu\text{K}$ . We estimate the detection efficiency to be  $\eta_c = 0.006$ , which is still less than the optimal estimate of  $\eta_c = 1$ .

For the parameters of this reconfigured system, we plot the phonon occupation versus scattered power in Fig. 6.2 to estimate our proximity to the standard quantum limit. It shows the cooled particle's phonon occupation against the

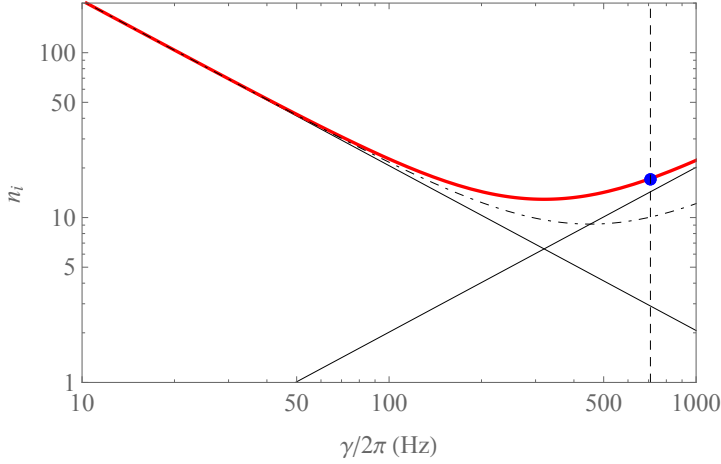


**Figure 6.2: Micro-Kelvin Standard Quantum Limit.** A plot of the model for phonon occupation versus feedback damping. Plotted in blue is for the configuration of the system at  $T_{\text{fb}} = 101 \mu\text{K}$ . When the detection efficiency is increased from  $\eta_c = 0.006$  to  $\eta_c = 0.012$ , the dot-dashed line in black indicates that the phonon occupation would be in the single-phonon regime.

contributions of measurement imprecision and backaction to the particle's motion in blue. Slightly improving the detection efficiency to  $\eta'_c = 0.012$  and raising the feedback damping to  $\gamma_{\text{fb}}/2\pi = 1 \text{ kHz}$  would bring the phonon occupation down to the single-phonon regime.

Nonetheless, the levitated nanoparticle is not only in the regime of strong measurement back-action, but also in the micro-Kelvin domain. A levitated nanoparticle at micro-Kelvin temperatures constitutes a highly out-of-equilibrium system because under feedback it is in competition with a bath of optical fluctuations at  $T_{\text{ph}} = \hbar\omega_0/8 = 1692 \text{ K}$  (c.f. Eq. 4.19), suggesting an opto-mechanical compression of more than seven orders of magnitude.

### 6.3 Sideband Thermometry

There are several assumptions that enter into measurements of temperature and calibration of the phonon occupation. First, the particle's motion is assumed

to be thermalized to a room temperature gas at  $T = 300$  K when calibrating at pressure  $P_{\text{gas}} = 10$  mbar. Recent work in photothermal heating suggests that the absorption of light by the silica may raise its internal temperature and affect the actual equilibrium temperature [139]. The optical gradient force is taken in the lowest order to be a restoring force forming an harmonic trapping potential; conditioned on this potential form, we invoke the equipartition theorem to convert detector voltage into an oscillation amplitude. Nonlinearities, however, were shown to influence the particle's natural thermal motion, distort spectra of its motion [101, 140], and would falsify the assumption of equipartition of energy [141]. Calibrations of detector voltage to displacement are taken at high pressures and assumed to stay constant over the duration of evacuation and measurement, which can often proceed for days. In this time, small changes to the particle's density or drifts in intensity can affect the center of mass frequency  $\Omega_0$  and add error to the calibration [100].

Though the measurements of micro-Kelvin temperatures have been repeated in our laboratory, alternate and precise methods of thermometry are needed. A standard within the opto-mechanical community is the calibration tone, as described in section 2.4.2, which uses a well-defined modulation to the reference arm of a homodyne interferometer to calibrate the oscillator's amplitude. Though robust, this technique requires the calibration tone and interferometric alignment to remain stable over the course of the measurement and assumes the particle's mass in order to determine temperature and consequently the phonon occupation.

In the following, we describe the technique of sideband thermometry and how it may be used for absolute measurements of the phonon occupation and temperature. It exploits the fundamentals of quantum mechanics – the quantum – which generates an asymmetry in the detected spectrum of the particle's motion because the zero-point fluctuations start to make a dominant contribution to the motion [142]. We present our experimental implementation and progress in resolving this asymmetry. We discuss classical sources of noise leading to an asymmetry and conclude with proposals for improving upon the status quo.

### 6.3.1 Heterodyne Interferometry

When the particle moves around the focus, it shifts the phase of the electric field that it scatters. It scatters light equally in the forward and backward directions because it is a Rayleigh scatterer. Particle tracking and the feedback cooling signal are derived from forward scattered light. In order to access the backscattered light, we exchange the microscope objective for an Olympus LCPLN100NIR with NA = 0.85 in air because it is optimized for transmission at  $\lambda = 1064$  nm.

The backscattered light from the particle propagates to the lens, as illustrated in Fig. 6.3. The backscattered field is given by

$$E_{\text{sc}}(t) = \bar{E}_{\text{sc}} \exp [i(\omega_0 t + kx(t))] \quad (6.1)$$

Here, we use  $x(t)$  to indicate the particle's position along one dimension for simplicity. The scattered field is interfered at the beamsplitter with a frequency-shifted local oscillator

$$E_{\text{ref}}(t) = \bar{E}_{\text{ref}} \exp [i(\omega_0 + \delta\omega)t] \quad (6.2)$$

The frequency shift is obtained using an acousto-optic modulator (AOM). Interference of the two fields gives a photocurrent equal to

$$I(t) = 2\bar{E}_{\text{sc}}\bar{E}_{\text{ref}} (\cos(\delta\omega t) - kx(t) \sin(\delta\omega t)) \quad (6.3)$$

when  $kx(t) \ll 1$ . An autocorrelation of the detected signal is given by [142]

$$\langle I(t)I(t + \tau) \rangle = 2 \left( \frac{4\pi\bar{E}_{\text{sc}}\bar{E}_{\text{ref}}}{\delta\omega} \right)^2 (1 + k^2 \langle x(t)x(t + \tau) \rangle) \cos(\delta\omega \tau) \quad (6.4)$$

For an harmonic oscillator  $x(t)$  the homogeneous solution to the classical equation of motion is

$$x(t) = x_0 \cos(\Omega_0 t) + (p_0/m\Omega_0) \sin(\Omega_0 t) \quad (6.5)$$

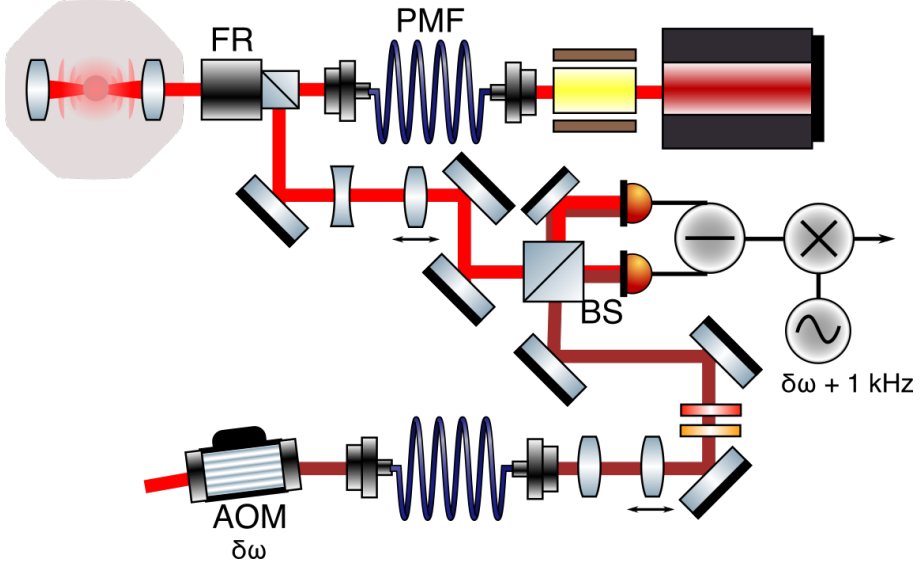


**Figure 6.3: Heterodyne Interferometry in Backscattering** The scattered field from a trapped nanoparticle is collected in backscattering by inserting a Faraday rotator (FR) in the beam path. When the illuminating field enters the trap with linear horizontal polarization, it is scattered back and converted into linear vertical polarization. A reference field is generated by frequency shifting the optical field with an acousto-optic modulator (AOM) set to frequency  $\delta\omega$ . The two fields interfere at the beam-splitter (BS) and are coupled to a balanced photodetector. The photodetector's output is mixed down with a local oscillator that differs by 1 kHz.

where  $x(0) = x_0$  and  $p(0) = p_0$ . The classical autocorrelation function is

$$\langle x(t)x(t + \tau) \rangle = \frac{1}{2} \cos(\Omega_0\tau) \left( \langle x_0^2 \rangle + \frac{\langle p_0^2 \rangle}{(m\Omega_0)^2} \right) \quad (6.6)$$

Here, we separated the motional and temporal degrees of freedom in computing an expectation value. The oscillatory terms were averaged over one cycle, or  $(\Omega_0/2\pi) \int_0^{2\pi/\Omega_0} dt \cos(\Omega_0 t) \cos(\Omega_0(t + \tau)) = \cos(\Omega_0\tau)/2$ .

Next we turn to the quantum correlation function. Using the definitions of the position and momentum operator for a quantum harmonic oscillator, which

## 6 Resolving the Classical to Quantum Transition

---

are given by  $\hat{x}_0 = \sqrt{\hbar/2m\Omega_0}(\hat{a} + \hat{a}^\dagger)$  and  $\hat{p}_0 = i\sqrt{\hbar m\Omega_0/2}(\hat{a}^\dagger - \hat{a})$ , and the commutation relationship  $[\hat{a}, \hat{a}^\dagger] = 1$ , we compute the position autocorrelation for the quantum harmonic oscillator

$$\begin{aligned} G_x(\tau) &= \langle \hat{x}(t)\hat{x}(t + \tau) \rangle & (6.7) \\ &= \frac{1}{2} \cos(\Omega_0\tau) \left( \langle \hat{x}_0\hat{x}_0 \rangle + \frac{\langle \hat{p}_0\hat{p}_0 \rangle}{(m\Omega_0)^2} \right) + \frac{1}{2m\Omega_0} \sin(\Omega_0\tau) \langle [\hat{x}_0, \hat{p}_0] \rangle \\ &= \langle x_{\text{zp}}^2 \rangle ((2\bar{n} + 1) \cos(\Omega_0\tau) + i \sin(\Omega_0\tau)) \end{aligned}$$

The autocorrelation is written in terms of the zero-point fluctuations,  $\langle x_{\text{zp}}^2 \rangle = \hbar/2m\Omega_0$ , and the Bose-Einstein occupation,  $\bar{n} = 1/(\exp[\hbar\Omega_0/k_B T_0] - 1)$ .

The normalized intensity autocorrelation function is

$$\begin{aligned} G_I(\tau) &= \frac{1}{2} \langle I(t)I(t + \tau) \rangle / (4\pi \bar{E}_{\text{sc}} \bar{E}_{\text{ref}} / \delta\omega)^2 & (6.8) \\ &= \cos(\delta\omega \tau) \\ &\quad + k^2 \langle x_{\text{zp}}^2 \rangle \left( \bar{n} + \frac{1}{2} \right) (\cos((\Omega_0 - \delta\omega)\tau) + \cos((\Omega_0 + \delta\omega)\tau)) \\ &\quad + k^2 \langle x_{\text{zp}}^2 \rangle \frac{i}{2} (\sin((\Omega_0 + \delta\omega)\tau) + \sin((\Omega_0 - \delta\omega)\tau)) \end{aligned}$$

Although position is a Hermitian observable with real eigenvalues, its autocorrelation function (c.f. Eq. 6.8) is complex [142]. Though unintuitive for a measurable signal to have a complex autocorrelation, this result directly boils out of the commutator relation  $[\hat{x}, \hat{p}] = i\hbar$ . It tells us that the two conjugate variables  $\hat{x}$  and  $\hat{p}$  are linked. Applying the Wiener-Khinchin theorem, we compute the power spectral density of the photocurrent by taking a Fourier transform of the autocorrelation function, which gives

$$\begin{aligned} S_{II}(\Omega)/\pi &= \delta[\Omega - \delta\omega] + \delta[\Omega + \delta\omega] & (6.9) \\ &\quad + k^2 \langle x_{\text{zp}}^2 \rangle (\bar{n} \delta[\Omega - (-\delta\omega + \Omega_0)] + (\bar{n} + 1) \delta[\Omega - (-\delta\omega - \Omega_0)]) \\ &\quad + k^2 \langle x_{\text{zp}}^2 \rangle (\bar{n} \delta[\Omega - (\delta\omega + \Omega_0)] + (\bar{n} + 1) \delta[\Omega - (\delta\omega - \Omega_0)]) \end{aligned}$$

From the expression in Eq. 6.9 for  $S_{II}(\Omega)$  we find that the power spectral density of the detected signal is asymmetric about the heterodyne carrier

frequency by the equivalent of one mechanical phonon.

### 6.3.2 Scattering Asymmetry

The asymmetry has two origins, the first of which is linked to the quantum nature of the harmonic oscillator. When an electric field interrogates the particle's position, it scatters away from it and has a fixed phase relationship with the particle's position. As we saw in Ch. 4, when a photon scatters away from the particle, it kicks it and causes a momentum shift in the particle's motion. The momentum exchange between the particle and the photon may either add or remove energy from the particle's motion. When energy is removed, the photon is scattered away at a higher frequency  $\omega' = \omega_0 + \Omega_0$ , and when energy is added, the photon scatters away at a lower frequency  $\omega'' = \omega_0 - \Omega_0$ . This process is illustrated in Fig. 6.4.

If the particle is in the ground state of its potential, quantum mechanics tells us that its energy can't be further reduced; the annihilation operator  $\hat{a}$  acting on the ground state  $|n = 0\rangle$  would return 0, which means that the operation cannot be done; however, the creation operator  $\hat{a}^\dagger$  acting on the ground state would raise the state to  $|n = 1\rangle$ . Thus, a photon interrogating the particle's position cannot remove energy from the motion when the particle is in the ground state, but it can add energy, which results in an asymmetric number of

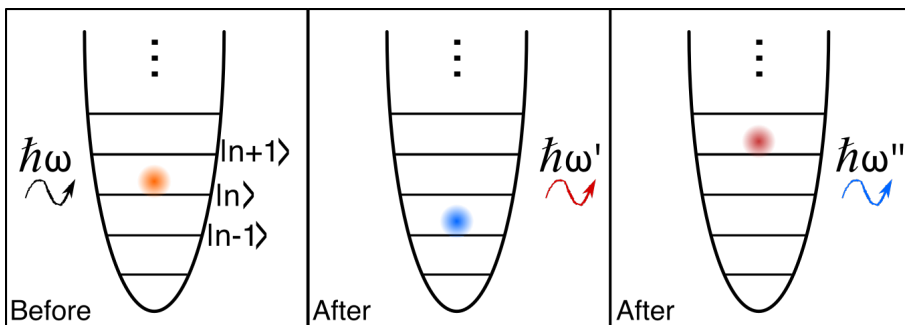


**Figure 6.4: Scattering Asymmetry Illustration.** Reheating from the photon scattering process may shift the harmonic oscillator's energy level from  $n$  to  $n - 1$ , which increases the photon's energy from  $\omega$  to  $\omega'$ ; or may shift the level from  $n$  to  $n + 1$ , decreasing  $\omega$  to  $\omega''$ .

photons scattered at  $\omega'$  and  $\omega''$ .

Although the imbalance of scattered photons occurs from a restriction due to quantum mechanics, it is important to recognize that it originates from the measurement process itself. Momentum kicks to the particle originate from fluctuations in the amplitude quadrature of the optical field. Scattering of that field by the particle changes fluctuations in the scattered field's phase proportional to the particle's position fluctuations, which themselves originate from the field's amplitude fluctuations. Recoil scattering therefore introduces a correlation between the amplitude and phase fluctuations of the optical field, which are by definition uncorrelated. We illustrate this interplay in Fig. 6.5.

### 6.3.3 Experimental Implementation

An experimental implementation of the heterodyne detection was carried out with a trapped nanoparticle ( $R = 68$  nm) in UHV. The backscattered light was guided onto a beamsplitter using two mirrors. Power scattered by the particle is  $P_{sc} = 20.4$   $\mu\text{W}$ ; half of that is scattered backward through an objective with NA = 0.85 and transmission efficiency  $\eta_t = 0.84$ , which results in  $P'_{sc} = 4.9$   $\mu\text{W}$  available for measurement; experimentally we measure  $P_{sc}^{\text{meas}} = 2.1$   $\mu\text{W}$  (using a ThorLabs powermeter), which agrees with the strong-focusing corrected intensity  $P_{sc}^c = 1.9$   $\mu\text{W}$ . The laser field enters the objective at a very small angle and the backscatter is walked 50 cm away to

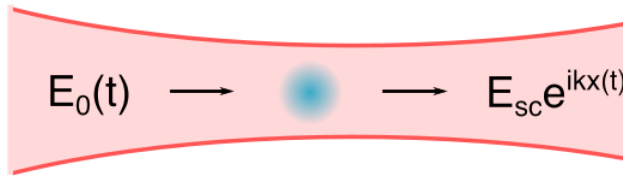


**Figure 6.5: Amplitude-Phase Correlations.** The illumination field  $E_0(t)$  is used to trap and measure the particle's position. It scatters from the particle into  $E_{sc} \exp[ikx(t)]$ , where the phase fluctuations contain a record of the particle's position. Fluctuations in the particle's position result from amplitude fluctuations of the light field that drive the particle into motion. The scattering process introduces amplitude-phase correlations of the optical field.



isolate it from stray backreflections.

A reference beam is generated with an AOM with frequency shift  $\delta\omega = 26.001$  MHz. We couple it through a polarization-maintaining fiber (PMF) and guide it to the same beamsplitter. A telescope exists along the backscatter beam path to increase the spot size and a unit gain beam expander exists on the reference path to better match the beam waist to the backscatter's. There are 20 mW of power in the reference arm. The two fields were coupled into a PMF for alignment and polarization matching; this was later removed and the beams were sent to a balanced photodetector, as illustrated in Fig. 6.3.

The heterodyne signal is measured with a homebuilt balanced photodetector. To track the two sidebands with our data acquisition system, we mix down the electronic signal using a mixer local oscillator frequency of  $\delta\omega - \omega_m$  for  $\omega_m = 1$  kHz and derived from the same source. Correspondingly, the  $\bar{n} \rightarrow (\bar{n} + 1)$  sideband, referred to as the Stokes' sideband, appears at  $(\Omega_0 - \omega_m)$  and the  $\bar{n} \rightarrow (\bar{n} - 1)$  sideband, referred to as the anti-Stokes' sideband, appears at  $(\Omega_0 + \omega_m)$ .

Plotted in Fig. 6.6a,b are the homodyne (forward scattering) and heterodyne (backscattering) spectra simultaneously obtained under weak feedback gain. The forward scattering spectra are calibrated in  $\text{pm}^2/\text{Hz}$ . The heterodyne spectrum is normalized by the peak height of the Stokes' sideband, which is why it is at 1.0. The calibrated occupation number in forward scattering is  $\bar{n}_f = 178.6$ , whereas the ratio of the two peaks in backscattering is  $R = 0.925$ . Doubling the feedback gain, we plot the response in Fig. 6.6c,d. Here, the calibrated occupation in forward scattering is  $\bar{n}_f = 108.5$  and in backscattering the ratio is  $R = 0.823$ . The ratio would suggest an occupation of  $\bar{n} = 4.7$ . Clearly, there is a significant discrepancy between the two methods.

### 6.3.4 Asymmetry-Generating Noise

At the time of the writing of this thesis, we do not make any conclusions on the measured sideband ratios but instead review systematically the contributions to the discrepancy and then propose how a researcher may continue.

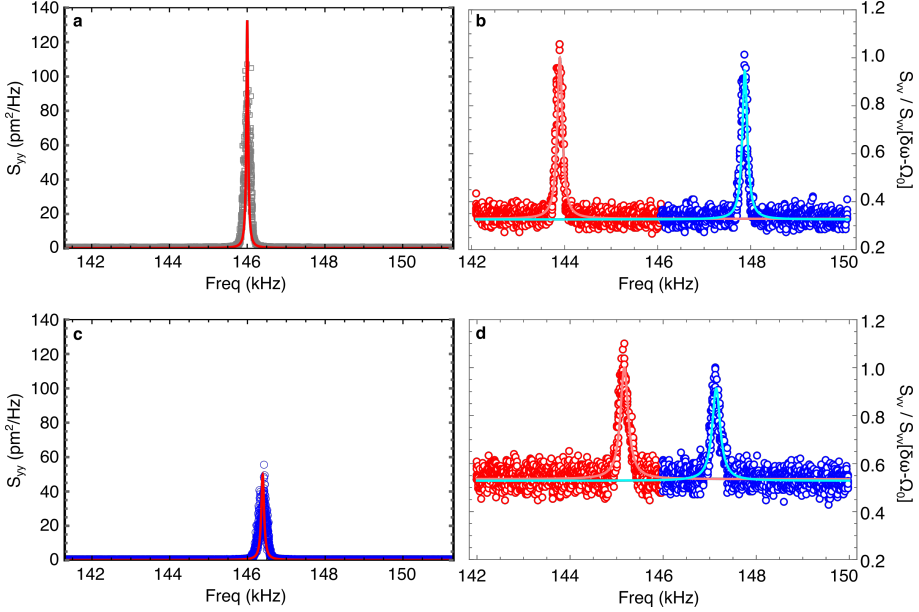


**Figure 6.6: Heterodyne Spectra in  $y$ .** Plots of the forward (a, c) and backward (b, d) scattered signal spectra in the  $y$  axis at two different feedback gain settings. The spectra in (b) and (d) are measured through a heterodyne interference in backscattering after the detector signal is mixed down at  $\delta\omega - \omega_m = 26.008$  MHz (in b) and 26.009 MHz (in d). These spectra are for a particle with nominal radius  $R = 68$  nm at a vacuum pressure of  $P_{\text{gas}} = 1.60 \times 10^{-8}$  mbar. Overlaid on each graph are fits to Lorentzians. The values reported in the text are obtained from these fits.

### 6.3.4.1 Detector Response

First and foremost, we interrogate the detector used to measure the heterodyne spectrum because the measured signal to noise ratio in back-scattering is much lower than that in forward scattering, despite simultaneous measurements. When 20 mW of power hits the detector, we measure a noise floor of  $\mathcal{S}_v(f) = 4 \times 10^{-14} \text{ V}^2/\text{Hz}$ .

The detector has responsivity  $\mathcal{R} = 0.77 \text{ A/W}$ , transimpedance gain  $R_{ti} = 2.5 \text{ k}\Omega$ , and a factor of  $G_{\text{bpf}} = 5$  gain on the output. The signal output of the detector is mixed down with a Mini-Circuits ZAY-3+ frequency mixer using a

local oscillator at  $\delta\omega - 1$  kHz. The mixer output has a  $L_c = 6$  dB conversion loss. Putting these numbers together gives

$$\mathcal{S}_{v_N}(f) = (2e\mathcal{R}P_0)R_{ti}^2G_{bpf}^2L_c = 4.3 \times 10^{-14} \text{ V}^2/\text{Hz} \quad (6.10)$$

The quantitative agreement between the calculated and measured noise floors indicates that the measurement is shot noise limited.

The detector may also filter the optical response if its transfer function isn't flat, which could artificially give rise to an asymmetry. With an input diode capacitance of 100 pF and op-amp gain-bandwidth product of  $f_{gbp} = 3.9$  GHz (Model OPA847), the diodes and TIA form a cutoff frequency of  $f_{RC} = 1/(R_{ti}C_{in})$ . Then the effective bandwidth is the geometric mean of the two parameters, or  $f_{bp} = \sqrt{f_{RC}f_{gbp}} = 59.6$  MHz, which is maintained by a 2 pF feedback capacitor. The signal is bandpass filtered and amplified on the output by a factor of 5 and includes a first-order low-pass filter with  $f_{3dB} = 72$  MHz. The optical response is well within the detector's bandwidth. A simulation in *LTSpice* indicates that the difference in response at  $(\delta\omega - \Omega_0)$  and  $(\delta\omega + \Omega_0)$  of the detector to be 67 mdB, compared to the measured peak height difference of 383 mdB. Accounting for this discrepancy raises the estimate to an occupation of  $n = 13.2$ .

### 6.3.4.2 Optical Response

The interference of the reference and scattered signals may be corrupted by classical noise sources including laser intensity and phase noise. An ongoing subject of study in the opto-mechanical community [27, 124, 125, 143, 144], laser noise contributions in interferometry were first elucidated from a quantum-optical perspective by Shapiro [145]. When the local oscillator in a balanced interferometer is much stronger than the signal field, the signal to noise ratio is given by [57]

$$\text{SNR} = \frac{\langle(\delta P(t))^2\rangle}{\langle P(t)^2\rangle} = \frac{2\sqrt{\eta P_{\text{sig}} P_{\text{ref}}}}{P_{\text{ref}} + P_{\text{sig}}} \simeq 2\sqrt{\eta P_{\text{sig}}/P_{\text{ref}}} \quad (6.11)$$

Here,  $\eta$  is the detection efficiency and  $P_{\text{ref}} \gg P_{\text{sig}}$ . When the local oscillator has amplitude fluctuations, the reference field is  $E_{\text{ref}} = E_{\text{ref}}^{(0)}(1 + \epsilon(t))$ , where  $\epsilon(t)$  is a small fluctuation. Fluctuations in the power would amount to  $P_{\text{ref}} = P_{\text{ref}}^{(0)}(1 + 2\epsilon(t))$ .

Balanced detection in interferometry is used because classical noise that is common-mode to both output ports of a beamsplitter are subtracted away in the detector. Shot noise, however, is not because a photon can either exit one port of the beamsplitter or the other. According to Shapiro [145], classical fluctuations in the local oscillator multiply with the signal field and lead to gain randomness on the signal. This would reduce the SNR to

$$\text{SNR}' = \frac{\langle (\delta P(t))^2 \rangle}{\langle P(t)^2 \rangle} = \frac{2\sqrt{\eta P_{\text{sig}}/P_{\text{ref}}}}{1 + \eta_0 \sqrt{\eta P_{\text{sig}}/P_{\text{ref}}}} \quad (6.12)$$

Here,  $\eta_0$  is the fractional rms local oscillator amplitude fluctuations, or its relative intensity noise. This means that the limit to fluctuations is governed by the detection efficiency, or  $\eta_0^2 \ll P_{\text{ref}}/\eta P_{\text{sig}}$ , in order to resolve the motion above the local oscillator's noise. In our current experimental setup, though the local oscillator is derived from the same laser source, the AOM drive electronics raise the intensity fluctuations of the local oscillator. Reducing that noise source is one avenue to pursue in improving the heterodyne spectrum.

Parametric modulation, which occurs at  $2\Omega_0$ , may also be converted to the sidebands in the interference process. This would raise the effective phonon number as the feedback gain is increased. Eq. 6.4 would become

$$I'(t) = 2\bar{E}_{\text{sc}}\bar{E}_{\text{ref}}(1 + 2\epsilon_1 \cos(2\Omega_0 t))[\cos(\delta\omega t) - kx(t) \sin(\delta\omega t)] \quad (6.13)$$

which would change the value of the sideband peak heights from  $(n + 1, n)$  to  $(n + 1 + \epsilon_1, n + \epsilon_1)$ . We imagine this may be a limitation to accurately determining phonon occupation through heterodyne ratios in the current experimental configuration, in which one single laser beam is used for trapping, feedback, and measurement.

### 6.3.4.3 Forward Scattering Interferometry

Interferometry in forward scattering is also possible; however, the added shot noise at the detector can mask our ability to detect the particle's motion. In this instance, there are three interfering fields, including the forward-scattered field, transmitted laser field, and a local oscillator, or

$$E_{\text{sc}} = E_1 \exp [i\omega_0 t + ikx_0 + ikx(t) + i\eta(z)] \quad (6.14a)$$

$$E_l = E_2 \exp [i\omega_0 t + ikx_0 + i\eta(z)] \quad (6.14b)$$

$$E_{\text{lo}} = E_3 \exp [i\omega_1 t] \quad (6.14c)$$

The scattered field  $E_{\text{sc}}$  would interfere with both the laser field  $E_l$  and the heterodyne local oscillator  $E_{\text{lo}}$ . The total intensity on the detector would be

$$I(t) = E_1^2 + E_2^2 + E_3^2 + 2E_2E_3 \sin(\omega_1 t) \quad (6.15)$$

$$+ 2E_1E_3 \cos(\omega_1 t - kx(t)) - 2E_2E_1 \sin(kx(t))$$

The component of interest is  $2E_1E_3 \cos(\omega_1 t - kx(t))$ , with autocorrelation

$$\langle \delta I_2(t) \delta I_2(t + \tau) \rangle = 2E_1^2 E_3^2 \cos(\omega_1 \tau) (1 + k^2 \langle x(t)x(t + \tau) \rangle) \quad (6.16)$$

The single-sided power spectral density of this signal is

$$S_2(\Omega) \propto \frac{P_{\text{sc}} P_{\text{lo}}}{\pi} (\delta(\Omega - \omega_1) + k^2 S_{xx}(\Omega - \omega_1)) \quad (6.17)$$

The first three terms in Eq. 6.15 contribute a shot noise background such that the signal to noise ratio is

$$\text{SNR} \propto \frac{(\eta_c P_{\text{sc}}) P_{\text{lo}} k^2}{2e\mathcal{R}(\eta_c P_1 + P_{\text{lo}})} S_{xx}(\Omega - \omega_1) \quad (6.18)$$

Here, we have included the detection efficiency  $\eta_c$ .

When  $P_{\text{lo}}$  is much stronger than  $\eta_c P_1$ , the heterodyne interference is visible

above the added shot noise. The SNR scales with the detection efficiency  $\eta_c$ , or

$$\lim_{P_{lo} \gg \eta_c P_l} \text{SNR} \propto \frac{(\eta_c P_{sc}) k^2}{2e\mathcal{R}} S_x(\Omega - \omega_1) \quad (6.19)$$

However, when  $P_{lo}$  is much weaker than  $\eta_c P_l$ , the heterodyne interference is increasingly masked by the shot noise of the laser field, or

$$\lim_{P_{lo} \ll \eta_c P_l} \text{SNR} \propto \frac{(\eta_c P_{sc}) k^2}{2e\mathcal{R}} \frac{P_{lo}}{\eta_c P_l} S_x(\Omega - \omega_1) \quad (6.20)$$

The interference visibility is attenuated by a factor  $\eta_c P_l / P_{lo}$ .

To maximize interference visibility would require  $P_l + P_{\text{ref}} \geq 100$  mW power on the detector while maintaining the bandwidth to track the 26 MHz shift. At the moment, such requirements are inaccessible owing to the large capacitances even of the high power photodiodes used in aspects of this thesis. An alternate scheme would use pseudo-heterodyne interferometry at a lower frequency, but would have a lower theoretical signal to noise ratio [146].

Recent opto-mechanical studies have shown that classical laser noise can enhance the asymmetry used in measuring phonon occupation [124]. Laser noise coupling to the mechanical resonator could drive it into motion; light used to measure the motion resulting from intensity noise driven motion would constructively interfere with the Stokes' sideband and destructively interfere with the anti-Stokes sideband to generate an enhanced asymmetry given by [27]

$$R = \frac{\bar{n}_{\text{tot}} - \bar{n}_{\text{cl}}}{\bar{n}_{\text{tot}} + \bar{n}_{\text{cl}} + 1} \quad (6.21)$$

Classical intensity fluctuations, the focus of the studies in Ch. 5, would result in a measured occupation number  $\bar{n}_m = R/(1 - R)$  to be less than it actually is. The contribution of RIN is given by

$$\bar{n}_{\text{cl}} = \frac{1}{2} \left( \frac{1}{2} \frac{P_{sc}}{\hbar\omega_0} S_{\text{RIN}}[\Omega_0] - 1 \right) = 0.043 \quad (6.22)$$

Here, we estimate the contribution based on our measured RIN under laser stabilization, or  $-148$  dB/Hz. If the value measured in forward scattering is  $\bar{n}_{\text{tot}} = 108$ , we would measure  $\bar{n}_m = 99.35$  from the ratio of the heterodyne

peaks. Though there is a discrepancy from the classical fluctuations, it still doesn't account for the large difference.

### 6.3.5 Proposed Design Changes

Several challenges have confronted the experimentalist in the process of measuring and controlling the particle's motion. Here, we offer three suggestions for improving measured signals, cooling further toward the ground state, and precision force sensing.

#### 6.3.5.1 Local Oscillator Mode Shaping

A major challenge in the interferometric technique in Ch. 6.3.1 is the limited signal to noise ratio in measuring the transverse axis motion in  $y$ . When the particle moves around the focus, it scatters a field whose phase is directly correlated with that of its position. As we saw in Ch. 2, phase changes occur in three dimensions when the particle moves. Using split detection, we map out how the phase in the scattered field changes with respect to the trapping field, which is a Gaussian mode.

Recent work harnessing the resources of different electromagnetic field modes in interferometry indicates that particle tracking in the transverse axes can be improved by an order of magnitude by tailoring the local oscillator's spatial mode [147]. We illustrate the proposed detection scheme in Fig. 6.7.

When the particle moves in the transverse axes, it scatters the input Gaussian  $\text{TEM}_{00}$  mode into either the  $\text{TEM}_{01}$  or  $\text{TEM}_{10}$  mode. These are linearly independent basis modes that construct the electromagnetic field.  $\text{TEM}_{00}$  is centro-symmetric, like the  $z$ -axis interference pattern of Fig. 2.5a.  $\text{TEM}_{10}$  has left-right symmetry and  $\text{TEM}_{01}$  has up-down symmetry.

In the current detection scheme for  $y$ -axis motion, we split the top and bottom halves of the beam. If instead we interfere the particle scatter with a  $\text{TEM}_{01}$  beam, the beamsplitter introduces a  $\pi$  phase shift between the transmitted and reflected fields, which constructively interferes with the top half in transmission and with the bottom half in reflection (illustrated in yellow in Fig. 6.7).

Theoretical estimates indicate that the conventional split detection scheme is only 80% efficient for displacement measurements whereas the shaped local

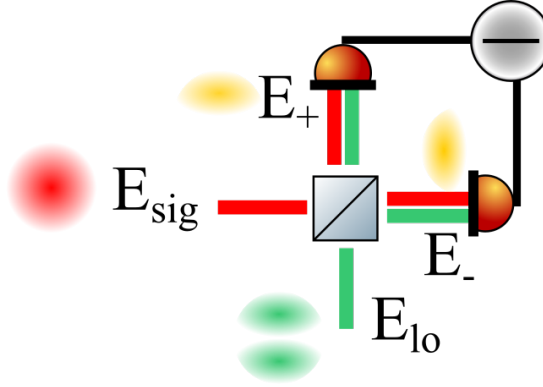


**Figure 6.7: Local Oscillator Mode Shaping** A balanced interferometry scheme that uses a tailored local oscillator mode. The signal beam  $E_{\text{sig}}$  is the scattered field from the particle. The reference field  $E_{\text{lo}}$  derives from the same laser but is introduced separately. Their interference occurs at the beam splitter and the corresponding photocurrents are subtracted to generate the balanced signal.

oscillator would bring displacement sensitivity to the Cramer-Rao bound, or 100% efficient [148]. The increase results from the sharp discontinuity at the center of the local oscillator mode, which increases the sensitivity to displacement from  $\mathcal{S}_{\text{split}}$  to  $\mathcal{S}_{\text{mode}}$ , which are given by

$$\mathcal{S}_{\text{split}} = \sqrt{\frac{2}{\pi}} \frac{2\sqrt{N_{sc}}}{w_0} \quad (6.23a)$$

$$\mathcal{S}_{\text{mode}} = \frac{2\sqrt{N_{sc}}}{w_0} \quad (6.23b)$$

Here,  $N_{sc}$  is the number of scattered photons and  $w_0$  is the beam waist.

### 6.3.5.2 Hybrid Tweezer Cavity

As we have seen, cooling a particle toward the ground state requires low dissipation  $\gamma$  and low measurement imprecision  $S_{\text{imp}}$  when using active feedback. With parametric feedback, we can compress the peak displacement to within a factor of 8 above the noise floor.

To overcome the issues of imprecision noise in measurement based feedback



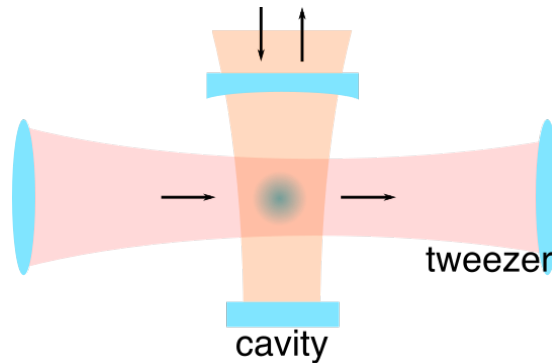


**Figure 6.8: Hybrid Optical Tweezer and Cavity** An illustration of a hybrid optical tweezer and optical cavity trap. The tweezer is used to hold the particle in place and, using feedback, pre-cool it into the micro-Kelvin regime. An optical cavity is an interface for both resolved sideband cooling and projecting non-classical states of light onto the mechanical object.

and, more importantly, for future tests in the macroscopic scaling of quantum phenomena, an optical cavity is necessary. Initial work in levitated nanoparticle cavity-optomechanics [79, 89] suggests that a levitated nanoparticle in an optical cavity alone is not sufficient. When a Gaussian optical mode is coupled into a cavity, it is designed to address just a single mechanical degree of freedom – along the cavity axis. As we have seen in Ch. 5, unstabilized intensity noise can drive a particle out of the trap. First we would use feedback cooling to pre-cool the particle and then implement existing protocols in resolved side-band cooling [21] to further reduce the center of mass motion.

Initial tests of a hybrid approach demonstrated 12.5% reduction in the center of mass motional temperature at medium vacuum pressures.

## 6.4 Outlook

The findings in this thesis represent a new frontier for levitated optomechanics, one in which backaction from the laser field overwhelms the thermal motion from the environment. We have brought optical levitation of nanoscopic matter to a new regime, one in which a nanoparticle’s center-of-mass temperature is

100  $\mu\text{K}$  despite its surroundings lying at 300 K. We have confined its motion to a length scale that is smaller than the Bohr radius and quantitatively measured the recoil momentum of photons scattering off of the nanoparticle.

At phonon occupations of  $\bar{n} = 15$ , we are slowly inching toward the holy grail that is the quantum ground state of motion. It is the author's opinion that optical levitation will result in a paradigm shift for quantum technologies by redefining the dissipation challenge. New materials and complex states of the optical field will enable this technique to access a host of previously inaccessible domains of physics. It will allow new tests of the fundamental laws of physics and herald a new avenue of quantum metrology.



## Mathematical Conventions

In this appendix, we review the mathematical conventions used in this thesis. Then we provide an illustrative example of their use in the context of the shot noise arising from a DC current.

### A.1 Fourier Transforms

The convention of Fourier transform  $\hat{x}$  used in this thesis is

$$\hat{x}(\omega) = \frac{1}{2\pi} \int_{-\infty}^{\infty} dt x(t) e^{i\omega t} \quad (\text{A.1a})$$

$$x(t) = \int_{-\infty}^{\infty} d\omega \hat{x}(\omega) e^{-i\omega t} \quad (\text{A.1b})$$

For a signal  $x(t)$  its autocorrelation function is defined as

$$\langle x(t)x(t+t') \rangle = \lim_{T \rightarrow \infty} \frac{1}{T} \int_{-T/2}^{T/2} dt x(t)x(t+t') \quad (\text{A.2})$$

Accordingly, the Wiener-Khinchin-Kolmogorov Theorem, which relates power spectral density with the autocorrelation function, is

$$S_{xx}(\Omega) = \frac{1}{2\pi} \int_{-\infty}^{\infty} dt' \langle x(t)x(t+t') \rangle e^{i\Omega t'} \quad (\text{A.3a})$$

$$\langle x(t)x(t+t') \rangle = \int_{-\infty}^{\infty} d\Omega S_{xx}(\Omega) e^{-i\Omega t'} \quad (\text{A.3b})$$

$S_{xx}(\Omega)$  is the power spectral density of the signal  $x(t)$ . Here, spectra are defined in terms of angular frequency. Spectra obtained from electronic instrumentation and apparatuses are often given in ordinary frequency ( $f = \Omega/2\pi$ ) and are single-sided. To convert between them, multiply by  $4\pi$ , or

$$\mathcal{S}_x(f) = 4\pi S_{xx}(\Omega) \quad (\text{A.4})$$

The script  $\mathcal{S}$  indicates ordinary frequency and the single  $x$  in the denominator indicates single-sided. By this convention, the spectra can be directly integrated over a fixed bandwidth ( $B = 2\pi b$ ) to get the variance of the signal, or

$$\sigma_x^2 = \int_{-b/2}^{b/2} df \mathcal{S}_x(f) \quad (\text{A.5})$$

## A.2 Shot Noise

An illustrative example is the shot noise of a current. Schottky derived the autocorrelation function arising from the discrete nature of electrons as [149]

$$\langle I(t)I(t+t') \rangle = q\bar{I}\delta(t-t') \quad (\text{A.6})$$

where  $\bar{I}$  is the average value of the current. Accordingly,

$$S_{II}(\Omega) = q\bar{I}/2\pi \quad (\text{A.7a})$$

$$\mathcal{S}_I(f) = 2q\bar{I} \quad (\text{A.7b})$$

The variance is computed within a bandwidth  $B = 2\pi b$ , or

$$\sigma_I^2 = 2 \int_{B/2}^{B/2} d\Omega S_{II}(\Omega) = q\bar{I}B/\pi = 2q\bar{I}b \quad (\text{A.8a})$$

$$\sigma_I^2 = \int_{-b/2}^{b/2} df \mathcal{S}_I(f) = 2q\bar{I}b \quad (\text{A.8b})$$

which agree with Schottky's predictions. Accordingly, the single-sided spectral density is defined as

$$\mathcal{S}_x(f) = 2 \int_{-\infty}^{\infty} dt' \langle F(t)F(t+t') \rangle e^{i2\pi ft'} \quad (\text{A.9})$$

# B

---

## Stochastic Averaging under Parametric Modulation

The goal of this document is to explain an analytical model for the PLL-based feedback and the influence of measurement imprecision in the feedback loop.

The equation of motion under feedback is

$$\ddot{x} + \gamma\dot{x} + \Omega_0^2(1 + \zeta(t))x = F_{\text{th}}(t)/m \quad (\text{B.1})$$

where  $\zeta(t) = \zeta_0 \cos(\Omega_m t)$  and  $\langle F_{\text{th}}(t)F_{\text{th}}(t') \rangle = 2m\gamma k_B T_0 \delta(t - t')$ . In this derivation, we will hold the feedback to be a weak modulation such that the particle motion can be approximated as

$$x(t) = A(t) \cos(\Omega_0 t + \varphi(t)) \quad (\text{B.2})$$

where the amplitude  $A$  and phase  $\varphi$  contain components that are large but slowly varying. The PLL modulation will have a phase given by

$$\Omega_m t = 2\Omega_0 t + 2\theta_m(t) + \theta_0 \quad (\text{B.3})$$

---

where  $\theta_m$  is the PLL's time-varying tracking phase and  $\theta_0$  is a constant phase offset. The phase error is defined as  $\nu = \varphi - \theta_m$ .

We will show that the amplitude and phase error under feedback cooling (when  $\theta_0 = \pi/2$ ) vary according to

$$\dot{A} = - \left( \frac{1}{2}\gamma + \frac{1}{4}\zeta_0\Omega_0 \cos(2\nu) \right) A + \frac{k_B T_0 \gamma}{2m\Omega_0^2} \frac{1}{A} + \xi'_F \quad (\text{B.4})$$

$$\dot{\nu} = - \left( -\frac{1}{4}\zeta_0\Omega_0 \sin(2\nu) + 4B_l \sin(\nu) \right) + \frac{1}{A}(\xi_{\text{imp}} + \xi''_F) \quad (\text{B.5})$$

where  $B_l$  is the PLL's bandwidth and  $\xi$  are random fluctuating excitation terms resulting from the thermal force ( $\xi'_F, \xi''_F$ ) and the measurement imprecision ( $\xi_{\text{imp}}$ ).

The solution is structured as follows:

1. Standard Form : Defining  $A, \varphi$
2. PLL Motion : Defining  $\nu$
3. Simplified Form : Dynamics of  $A, \nu$
4. Truncated Equations : Deterministic Averaging
5. Langevin Equations : Stochastic Averaging
6. Coupled Equations :  $\bar{A}$  and  $\bar{\nu}$

We first define the amplitude  $A$  and particle oscillation phase  $\varphi$  to get the system equations in *standard form*. Second, we define the equation of motion for the phase error  $\nu$  in a phase-locked loop. Then, we recast the dynamics in terms of the phase error  $\nu = \theta_m - \varphi$  and derive the *simplified equations* which do not contain rapid oscillations. Next, we eliminate oscillations from the nonfluctuational (or deterministic) terms to derive the *truncated equation*.

Finally, using the techniques of stochastic averaging, we recover the *Langevin equations* of Eqs. (B.4),(B.5).

### B.0.1 Standard Form

We rewrite the equation of motion in Eq. (B.1) as

$$\ddot{x} + \Omega_0^2 x = -\gamma \dot{x} - \Omega_0^2 \zeta_0 \cos(\Omega_m t) x + F_{th}(t)/m \quad (\text{B.6})$$

Here, we establish a few assumptions:

- Assumption 1 :  $\zeta_0 \ll 1$
- Assumption 2 :  $\cos(\Omega_m t)$  is in phase with the particle's oscillation
- Assumption 3 :  $\Omega_0^2 \zeta_0 \cos(\Omega_m t) x$  doesn't change the particle's motion in one oscillation cycle

Based on these assumptions, we form the ansatz for the particle's oscillation given in Eq. (B.2). We take a derivative of  $x(t)$  with respect to time  $t$  to get the velocity  $\dot{x}(t)$

$$\dot{x}(t) = \dot{A}(t) \cos(\Omega_0 t + \varphi(t)) - A(t) \sin(\Omega_0 t + \varphi(t)) (\Omega_0 + \dot{\varphi}(t)) \quad (\text{B.7})$$

Next, we make another assumption

- Assumption 4 :  $A(t)$  and  $\varphi(t)$  vary on timescales much longer than  $2\pi/\Omega_0$ . Thus,  $\dot{A} \sim 0$  in comparison to  $A$  and  $\dot{\varphi} \sim 0$  as compared to  $\Omega_0$ .

Accordingly, the velocity is given by

$$\dot{x}(t) = -A\Omega_0 \sin(\Omega_0 t + \varphi(t)) \quad (\text{B.8})$$

In terms of  $x$  and  $\dot{x}$ , the amplitude and phase are given by

$$A^2 = x^2 + (\dot{x}/\Omega_0)^2 \quad (\text{B.9})$$

$$\varphi = -\arctan(\dot{x}/\Omega_0 x) - \Omega_0 t \quad (\text{B.10})$$



---

## B.0.2 PLL Equation of Motion

Here, we recreate a derivation by Viterbi of the PLL's equation of motion.

The particle's oscillation signal is

$$x_d(t) = \sqrt{2}A(t) \sin(\Omega_0 t + \varphi(t)) + n(t) \quad (\text{B.11})$$

where  $n(t)$  is the measurement imprecision noise. It can be split into two separate quadratures, or

$$n(t) = \sqrt{2}n_1(t) \sin(\Omega_0 t) + \sqrt{2}n_2(t) \cos(\Omega_0 t) \quad (\text{B.12})$$

where  $n_1(t)$  and  $n_2(t)$  are effectively independent and uncorrelated. The PLL's voltage controlled oscillator (VCO) has output signal

$$x_{\text{vco}}(t) = \sqrt{2}K_3 \cos(\Omega_0 t + \theta_m(t)) \quad (\text{B.13})$$

The PLL control loop operates based on the phase difference between  $x_{\text{det}}$  and  $x_{\text{vco}}$ ; a simplistic model is illustrated in Fig. B.1.

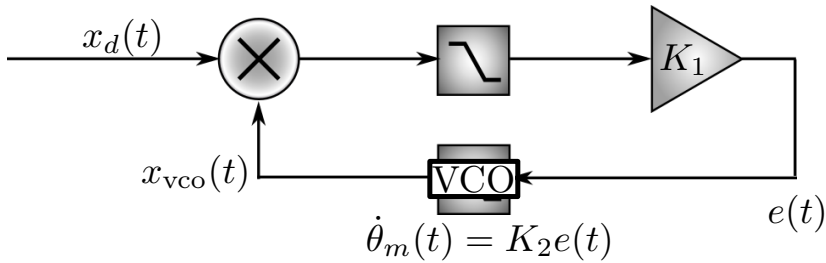


**Figure B.1: PLL Schematic** A phase-locked loop is drawn with an input signal and the loop tracking signal.  $n(t)$  is the measurement imprecision and  $A$  is the oscillation amplitude.

The mixer generates the product of the particle motion and the VCO (here

the reference), which is

$$\begin{aligned}
 x_d \cdot x_{\text{vco}} &= 2\{A \sin(\Omega_0 t + \varphi(t)) + n_1(t) \sin(\Omega_0 t) + n_2(t) \cos(\Omega_0 t)\} \\
 &\quad \times \{K_3 \cos(\Omega_0 t + \theta_m(t))\} \\
 &= K_3\{A \sin(\varphi(t) - \theta_m(t)) - n_1(t) \sin(\theta_m(t)) + n_2(t) \cos(\theta_m(t)) \\
 &\quad + A \sin(2\Omega_0 t + \varphi(t) + \theta_m(t)) \\
 &\quad + n_1(t) \sin(2\Omega_0 t + \theta_m(t)) + n_2(t) \cos(2\Omega_0 t + \theta_m(t))\} \quad (\text{B.14})
 \end{aligned}$$

The mixer output consists of terms near DC and terms at  $2\Omega_0$ . The high frequency terms are filtered away, which results in an error signal given by

$$e(t) = K_1 K_3 \{A \sin(\varphi(t) - \theta_m(t)) - n_1(t) \sin(\theta_m(t)) + n_2(t) \cos(\theta_m(t))\} \quad (\text{B.15})$$

Let  $\nu(t) = \varphi(t) - \theta_m(t)$  and  $K = K_1 K_2 K_3$ . The VCO integrates the error signal with a certain gain  $K_2$  and adjusts the phase of its output by

$$\dot{\theta}_m(t) = K_2 e(t) \quad (\text{B.16})$$

The phase error is then given by

$$\begin{aligned}
 \dot{\nu}(t) &= \dot{\varphi}(t) - K_2 e(t) \quad (\text{B.17}) \\
 &= \dot{\varphi}(t) - K(A \sin(\nu(t)) - n_1(t) \sin(\theta_m(t)) + n_2(t) \cos(\theta_m(t))) \\
 &= \dot{\varphi}(t) - K(A \sin(\nu(t)) + n'(t))
 \end{aligned}$$

where  $n'(t) = -n_1 \sin \theta_m + n_2 \cos \theta_m$ . When  $K = 4B_l/A$  the phase error varies as

$$\dot{\nu}(t) = \dot{\varphi}(t) - 4B_l \sin(\nu(t)) - \frac{4B_l}{A} n'(t)$$

Here there is an additional assumption, which is

- Assumption 5 : The phase error equation  $\dot{\nu}$  describes the PLL in a locked state.

---

### B.0.3 Simplified Form

Next, we want to compute how  $A$  and  $\varphi$  vary as a function of  $t$ . Defining  $\phi(t) = \Omega_0 t + \varphi(t)$  the derivatives are

$$\dot{A} = \frac{\dot{x}(\ddot{x} + \Omega_0^2 x)}{\Omega_0^2 (x^2 + (\dot{x}/\Omega_0)^2)^{1/2}} \quad (\text{B.18})$$

$$\begin{aligned} & \overbrace{\left[ -\frac{\sin \phi}{\Omega_0} (\gamma A \Omega_0 \sin \phi - A \Omega_0^2 \zeta_0 \cos(\Omega_m t) \cos \phi) \right]}^{h_1} \overbrace{\left[ -\frac{\sin \phi}{m \Omega_0} F_{\text{th}}(t) \right]}^{h_2} \\ \dot{\varphi} &= -\frac{x}{\Omega_0 A^2} (\ddot{x} + \Omega_0^2 x) \quad (\text{B.19}) \\ & \overbrace{\left[ -\cos \phi (\gamma \sin \phi - \Omega_0 \zeta_0 \cos(\Omega_m t) \cos \phi) \right]}^{h_3} \overbrace{\left[ -\frac{\cos \phi}{m \Omega_0 A} F_{\text{th}}(t) \right]}^{h_4} \end{aligned}$$

Here, we have defined the deterministic  $(h_1, h_3)$  and the stochastic  $(h_2, h_4)$  components of the equations.

The phase error varies as

$$\begin{aligned} \dot{\nu} &= \dot{\varphi} - 4B_l \sin(\nu) - \frac{4B_l}{A} n'(t) \quad (\text{B.20}) \\ & \overbrace{\left[ -\cos \phi (\gamma \sin \phi - \Omega_0 \zeta_0 \cos(\Omega_m t) \cos \phi) - 4B_l \sin(\nu) \right]}^{h_3^{(\nu)}} \\ & \overbrace{\left[ -\frac{\cos \phi}{m \Omega_0 A} F_{\text{th}}(t) \right]}^{h_4^{(\nu)}} \overbrace{\left[ -\frac{4B_l}{A} n'(t) \right]}^{h_5} \end{aligned}$$

where  $n'(t)$  is the noise due to measurement imprecision and  $B_l$  is the PLL tracking bandwidth. We defined new components as  $h_3^{(\nu)}$  and  $h_5$ .

### B.0.4 Truncated Equations

To analyze how  $A$  and  $\nu$  vary in time, we have to average over the rapid oscillations in  $h_1$  and  $h_3^{(\nu)}$ . Averaging is applied to only keep contributions that are relevant at the timescales associated with the dynamics of  $A$ ,  $\varphi$ , and  $\nu$  in that specific case.

#### B.0.4.1 Deterministic averaging of $h_1$

We expand  $h_1$  as

$$h_1 = -\frac{1}{2}\gamma A(1 - \cos(2\Omega_0 t + 2\varphi(t))) + \frac{1}{4}A\Omega_0\zeta_0(-\sin(2\theta_m + \theta_0 - 2\varphi) + \sin(4\Omega_0 t + 2\theta_m + \theta_0 + 2\varphi)) \quad (\text{B.21})$$

Average over one oscillation cycle as

$$\langle h_1 \rangle = \frac{\Omega_0}{2\pi} \int_0^{2\pi/\Omega_0} h_1(t) dt = \frac{1}{4}A\Omega_0 \left( -\frac{2\gamma}{\Omega_0} - \zeta_0 \sin(\theta_0 - 2\nu) \right) \quad (\text{B.22})$$

In the last step of Eq. (B.22) we substituted the phase error  $\nu = \varphi - \theta_m$ .

#### B.0.4.2 Deterministic averaging of $h_3^{(\nu)}$

We expand  $h_3^{(\nu)}$  as

$$h_3^{(\nu)} = -\frac{1}{2}\gamma \sin(2\Omega_0 t + 2\varphi) - 4B_l \sin(\nu) + \frac{1}{4}\Omega_0\zeta_0(\cos(\theta_0 - 2\nu) + 2\cos[2\Omega_0 t + 2\theta_m + \theta_0] + \cos[4\Omega_0 t + 2\theta_m + \theta_0 + 2\varphi]) \quad (\text{B.23})$$

Now, we average over one oscillation cycle, or

$$\langle h_3^{(\nu)} \rangle = \frac{1}{4}\zeta_0\Omega_0 \cos(\theta_0 - 2\nu) - 4B_l \sin(\nu) \quad (\text{B.24})$$

#### B.0.4.3 Truncated Equations

We define the *truncated equations* as having the oscillatory terms removed.

Taking  $\theta_0 = \pi/2$ , they are

$$\dot{A} = -\left( \frac{1}{2}\gamma + \frac{1}{4}\zeta_0\Omega_0 \cos(2\nu) \right) A + h_2 \quad (\text{B.25})$$

$$\dot{\nu} = -\left( -\frac{1}{4}\zeta_0\Omega_0 \sin(2\nu) + 4B_l \sin(\nu) \right) + h_4 + h_5 \quad (\text{B.26})$$

---

We can glean some insight from the truncated equations. First, the amplitude decays at a rate that is  $-(\frac{1}{2}\gamma + \frac{1}{4}\zeta_0\Omega_0 \cos(2\nu))$ , which means that the feedback increases the rate at which the particle's motion is damped. Second, when the phase error  $\nu$  is small, then it decays with  $-(-\frac{1}{2}\zeta_0\Omega_0 + 4B_l)$ , which means that without any noise, the phase error will go to zero only when the feedback gain is negligibly small. Large modulation depths  $\zeta_0$  will cause the feedback to inadvertently have an increase in phase error. The intuitive explanation for this is that under strong feedback, the linewidth increases. When the linewidth exceeds the PLL's detection bandwidth, the PLL will miss information from the particle's oscillation.

## B.0.5 Langevin Equations

The fluctuational terms  $h_2$ ,  $h_4$ , and  $h_5$  contain oscillatory terms. We are interested in the smooth changes of amplitude and phase and not in the high-frequency oscillations. Next, we get rid of the oscillatory terms by performing a stochastic average as defined by Stratonovich.

### B.0.5.1 Expectation Values of the Thermal Force

Consider the thermal force variables

$$h_2 = -\frac{1}{m\Omega_0}F_{\text{th}}(t) \sin(\Omega_0 t + \varphi(t)) \quad (\text{B.27})$$

$$h_4 = -\frac{1}{m\Omega_0 A}F_{\text{th}}(t) \cos(\Omega_0 t + \varphi(t)) \quad (\text{B.28})$$

We try to get their respective statistical properties. First, we will compute their expected values. Then, we will estimate their correlation functions. Here the phase  $\varphi(t)$  is correlated with the values of the random function  $F_{\text{th}}(t)$ . However, we will assume that the correlation time of the process  $F_{\text{th}}(t)$  is so small that a time shift  $\alpha$  can be found which simultaneously satisfies

$$\begin{aligned} \alpha &\gg \tau_F & (\text{B.29}) \\ |A(t) - A(t - \alpha)| &\equiv |A - A_{-\alpha}| \ll A_0 \\ |\varphi(t) - \varphi(t - \alpha)| &\equiv |\varphi - \varphi_\alpha| \ll 1 \end{aligned}$$

This means that although  $\alpha$  greatly exceeds the thermal force correlation time, the amplitude and phase don't manage to change appreciably during the time  $\alpha$ . Since the values  $A(t - \alpha) \equiv A_{-\alpha}$  and  $\varphi(t - \alpha) \equiv \varphi_{-\alpha}$  are close to  $A(t)$  and  $\varphi(t)$ , it is a good approximation to write  $h_2$  as follows using  $\Delta\varphi = \varphi - \varphi_{-\alpha}$ ,

$$\begin{aligned} h_2 &= -\frac{1}{m\Omega_0} F_{\text{th}}(t) \sin[\Omega_0 t + (\varphi_{-\alpha} - \Delta\varphi)] \\ &= -\frac{1}{m\Omega_0} F_{\text{th}}(t) (\sin(\Omega_0 t + \varphi_{-\alpha}) \cos(\Delta\varphi) + \cos(\Omega_0 t + \varphi_{-\alpha}) \sin(\Delta\varphi)) \\ &\simeq -\frac{1}{m\Omega_0} F_{\text{th}}(t) [\sin(\Omega_0 t + \varphi_{-\alpha}) + \cos(\Omega_0 t + \varphi_{-\alpha}) \Delta\varphi] \end{aligned} \quad (\text{B.30})$$

and  $h_4$  as

$$\begin{aligned} h_4 &= -\frac{F_{\text{th}}(t)}{m\Omega_0 A} \cos(\Omega_0 t + \varphi(t)) \\ &\simeq -\frac{F_{\text{th}}(t)}{m\Omega_0 A} \cos(\Omega_0 t + \varphi_{-\alpha}) + \frac{F_{\text{th}}(t)}{m\Omega_0 A} \sin(\Omega_0 t + \varphi_{-\alpha}) \Delta\varphi \end{aligned} \quad (\text{B.31})$$

However,  $A_{-\alpha}$  and  $\varphi_{-\alpha}$ , unlike  $A(t)$  and  $\varphi(t)$ , are effectively statistically independent of  $F_{\text{th}}(t)$  and hence we can average over  $F_{\text{th}}(t)$  and  $\varphi_{-\alpha}$  separately. This gives for the mean value of  $h_2$

$$\begin{aligned} \langle h_2 \rangle &= -\frac{1}{m\Omega_0} (\langle F_{\text{th}} \rangle \sin(\Omega_0 t + \varphi_{-\alpha}) + \langle F_{\text{th}} \Delta\varphi \rangle \cos(\Omega_0 t + \varphi_{-\alpha})) \\ &= -\frac{1}{m\Omega_0} \langle F_{\text{th}} \Delta\varphi \rangle \cos(\Omega_0 t + \varphi_{-\alpha}) \end{aligned}$$

where in the second step we recall that the thermal force is a zero mean process. Next, we integrate the equation for the phase. The phase variables  $\varphi$ ,  $\theta_m$ , and  $\nu$  are all effectively statistically independent of  $F_{\text{th}}(t)$ ; in this short time interval  $\alpha$ , the infinitesimal phase change  $\Delta\varphi \sim \Delta\nu$ . Integrating the phase error equation

yields

$$\begin{aligned}
\Delta\nu &= \int_{t-\alpha}^t \dot{\nu} dt = \int_{-\alpha}^0 \dot{\nu} d\tau & (\text{B.32}) \\
&= \int_{-\alpha}^0 \left( \frac{1}{4}\Omega_0\zeta_0 \cos[\theta_0 - 2\nu(\tau + t)] + 4B_l \sin[\nu(\tau + t)] \right. \\
&\quad - \frac{F_{\text{th}}(\tau + t)}{m\Omega_0 A(\tau + t)} \cos[\Omega_0(\tau + t) + \varphi(\tau + t)] \\
&\quad \left. - \frac{4B_l}{A} n_1(\tau + t) \sin(\theta_m(\tau + t)) + \frac{4B_l}{A} n_2(\tau + t) \cos(\theta_m(\tau + t)) \right) d\tau
\end{aligned}$$

Considering that  $F_{\text{th}}$  is stationary, that it is uncorrelated with and independent of the measurement noise, and that  $\alpha \ll (\tau_A, \tau_\varphi, \tau_\nu)$ , one gets

$$\begin{aligned}
\langle F_{\text{th}}\Delta\nu \rangle &= \int_{-\alpha}^0 \left\langle \frac{1}{4}\Omega_0\zeta_0 F_{\text{th}} \cos(\theta_0 - 2\nu) - 4B_l F_{\text{th}} \sin(\nu) \right. & (\text{B.33}) \\
&\quad - \frac{F_{\text{th}}F_{\text{th}\tau}}{m\Omega_0 A_\tau} \cos(\Omega_0\tau + \Omega_0t + \varphi) \\
&\quad \left. - \frac{4B_l}{A_\tau} F_{\text{th}} n_{1\tau} \sin(\theta_m) + \frac{4B_l}{A_\tau} F_{\text{th}} n_{2\tau} \cos(\theta_m) \right\rangle d\tau \\
&= \int_{-\alpha}^0 \left( -\frac{\langle F_{\text{th}}F_{\text{th}\tau} \rangle}{m\Omega_0 A_\tau} \cos(\Omega_0\tau + \Omega_0t + \varphi) \right) d\tau \\
&= -\frac{1}{m\Omega_0 A} \frac{1}{2} \int_{-\infty}^{\infty} 2m\gamma k_B T_0 \delta(\tau) \cos(\Omega_0\tau + \Omega_0t + \varphi) d\tau \\
&= -\frac{\gamma k_B T_0}{\Omega_0 A} \cos(\Omega_0t + \varphi)
\end{aligned}$$

We extend the lower limit of integration to  $-\infty$  since the correlation function in the integrand is essentially zero for  $|\tau| > \alpha \gg \tau_{F_{\text{th}}}$ . The autocorrelation of the thermal force is even in frequency space, which is why we extend to  $\infty$  and multiply by  $\frac{1}{2}$ . Substituting in, we find

$$\langle h_2(t) \rangle = \frac{\gamma k_B T_0}{m\Omega_0^2 A} \cos(\Omega_0t + \varphi) \cos(\Omega_0t + \varphi) \quad (\text{B.34})$$

To get a stationary representation of  $\langle h_2 \rangle$ , we average this over one oscillation cycle, which gives

$$\begin{aligned}\langle h_2 \rangle &= \frac{\Omega_0}{2\pi} \int_0^{2\pi/\Omega_0} \langle h_2(t) \rangle dt \\ &= \frac{\gamma k_B T_0}{2m\Omega_0^2 A}\end{aligned}\quad (\text{B.35})$$

The fact that  $\langle h_2 \rangle \neq 0$  is due to the correlation between  $F_{\text{th}}$  and  $\varphi$ .

Similarly, we calculate the average of  $h_4$ , which is

$$\begin{aligned}\langle h_4 \rangle &= \frac{1}{m\Omega_0 A} \frac{\Omega_0}{2\pi} \int_0^{2\pi/\Omega_0} \langle F_{\text{th}} \Delta \nu \rangle \sin(\Omega_0 t + \varphi) dt \\ &= 0\end{aligned}\quad (\text{B.36})$$

### B.0.5.2 Correlation Functions of the Thermal Force

Next we proceed with estimating the correlation function of the zero mean processes  $h'_2 = h_2 - \langle h_2 \rangle$  and  $h'_4 = h_4$ . In Eqs. (B.30),(B.31) where we approximated  $h_2$  and  $h_4$ , the mean values are given by the second terms on the right-hand side and the fluctuating components result from the first terms, or

$$h'_2 \simeq -\frac{F_{\text{th}}}{m\Omega_0} \sin(\Omega_0 t + \varphi_{-\alpha}) \quad (\text{B.37})$$

$$h'_4 \simeq -\frac{F_{\text{th}}}{m\Omega_0 A} \cos(\Omega_0 t + \varphi_{-\alpha}) \quad (\text{B.38})$$

Since the force correlation time is much smaller than the relaxation time, the random excitations act as if they were uncorrelated, and the actual correlation function can be replaced by one shaped like a delta function, or

$$\langle h'_2 h'_{2\tau} \rangle = \int_{-\infty}^{\infty} \langle h'_2 h'_{2\tau} \rangle \delta(\tau) d\tau = \delta(\tau) \int_{-\infty}^{\infty} \langle h'_2 h'_{2\tau} \rangle d\tau \quad (\text{B.39})$$



Here, we choose the intensity coefficient of the delta-correlated noise source to be  $\int_{-\infty}^{\infty} \langle h'_2 h'_{2\tau} \rangle d\tau$ . Considering first  $h'_2$ , one can write

$$\begin{aligned} \langle h'_2 h'_{2\tau} \rangle &= \delta(\tau) \int_{-\infty}^{\infty} \left\langle \frac{F_{\text{th}}}{m\Omega_0} \sin(\Omega_0 t + \varphi_{-\alpha}) \frac{F_{\text{th}\tau}}{m\Omega_0} \sin(\Omega_0(t + \Theta) + \varphi_{-\alpha}) \right\rangle d\Theta \\ &= \frac{\delta(\tau)}{2m^2\Omega_0^2} \int_{-\infty}^{\infty} \langle F_{\text{th}} F_{\text{th}\tau} \rangle (\cos(\Omega_0\Theta) - \cos(2\Omega_0 t + \Omega_0\Theta + 2\varphi_{-\alpha})) d\Theta \\ &= \frac{\gamma k_B T_0}{m\Omega_0^2} \delta(\tau) \end{aligned} \quad (\text{B.40})$$

Considering now  $h'_4$  one can write

$$\langle h'_4 h'_{4\tau} \rangle = \delta(\tau) \int_{-\infty}^{\infty} \left\langle \frac{F_{\text{th}}}{m\Omega_0 A} \cos(\Omega_0 t + \varphi_{-\alpha}) \frac{F_{\text{th}\tau}}{m\Omega_0 A} \cos(\Omega_0(t + \Theta) + \varphi_{-\alpha}) \right\rangle d\Theta \quad (\text{B.41})$$

$$\begin{aligned} &= \frac{\delta(\tau)}{2(m\Omega_0 A)^2} \int_{-\infty}^{\infty} \langle F_{\text{th}} F_{\text{th}\tau} (\cos(\Omega_0\Theta) + \cos(2\Omega_0 t + \Omega_0\Theta + 2\varphi_{-\alpha})) \rangle d\Theta \\ &= \frac{\gamma k_B T_0}{m\Omega_0^2 A^2} \delta(\tau) \end{aligned} \quad (\text{B.42})$$

### B.0.5.3 Expectation Values of the Measurement Noise

Next we study the contribution of measurement imprecision noise. The imprecision noise term is

$$h_5 = \frac{4B_l}{A} n'(t) \quad (\text{B.43})$$

First, we calculate the expectation value and then the correlation. We define

$$h_5^{(1)} = -\frac{4B_l}{A} n_1(t) \sin(\Omega_0 t + \theta_m(t)) \quad (\text{B.44})$$

$$h_5^{(2)} = \frac{4B_l}{A} n_2(t) \cos(\Omega_0 t + \theta_m(t)) \quad (\text{B.45})$$

We approximate these as

$$h_5^{(1)} \simeq -\frac{4B_l}{A}n_1 \sin(\Omega_0 t + \theta_{m\alpha}) - \frac{4B_l}{A}n_1 \cos(\Omega_0 t + \theta_{m\alpha})\Delta\theta_m \quad (\text{B.46})$$

$$h_5^{(2)} \simeq \frac{4B_l}{A}n_2 \cos(\Omega_0 t + \theta_{m\alpha}) - \frac{4B_l}{A}n_2 \sin(\Omega_0 t + \theta_{m\alpha})\Delta\theta_m \quad (\text{B.47})$$

The time interval  $\alpha$  is longer than the correlation time of the noise source but shorter than that of the amplitude and of the phase ( $\tau_n \ll \alpha \ll (\tau_A, \tau_\nu)$ ). Here,  $\theta_{m\alpha} = \theta_m(t - \alpha)$  and  $\Delta\theta_m = \theta_m - \theta_{m\alpha}$ . Considering that  $\theta_{m\alpha}$  is not correlated with  $n'$  since  $\tau_n \ll \alpha$  and  $\alpha \ll \tau_{\theta_m}$ , one can write

$$\langle h_5^{(1)} \rangle = -\cos(\Omega_0 t + \theta_{m\alpha}) \left\langle \frac{4B_l}{A}n_1 \Delta\nu \right\rangle \quad (\text{B.48})$$

$$\langle h_5^{(2)} \rangle = -\sin(\Omega_0 t + \theta_{m\alpha}) \left\langle \frac{4B_l}{A}n_2 \Delta\nu \right\rangle \quad (\text{B.49})$$

The averaging, as before, is straightforward. Here, we expand out all the terms and then compute the total average. First for  $h_5^{(1)}$

$$\begin{aligned} \langle n_1 \Delta\nu \rangle = \int_{-\alpha}^0 & \left\langle \frac{1}{4}\zeta_0 \Omega_0 n_1 \cos(\theta_0 - 2\nu) - 4B_l n_1 \sin(\nu) \right. \\ & - \frac{n_1 \mathbf{F}_{\text{th}\tau}}{m\Omega_0 A} \cos(\Omega_0(\tau + t) + \varphi) \\ & \left. - \frac{4B_l}{A}n_1 n_{1\tau} \sin(\theta_m) + \frac{4B_l}{A}n_1 n_2 \cos(\theta_m) \right\rangle d\tau \end{aligned} \quad (\text{B.50})$$

Then, the average of  $h_1^{(1)}$  is

$$\begin{aligned} \langle h_5^{(1)} \rangle &= \frac{4B_l}{A} \int_{-\infty}^0 d\tau \langle n_1 n_{1\tau} \rangle \cos(\Omega_0 t + \theta_{m\alpha}) \sin \theta_m \\ &= \frac{4B_l}{2A} S_{\text{imp}} \sin(2\theta_m) \end{aligned} \quad (\text{B.51})$$

Next for  $h_5^{(2)}$ ,

$$\begin{aligned}
\langle n_2 \Delta \nu \rangle &= \int_{-\alpha}^0 \left\langle \frac{1}{4} \Omega_0 \zeta_0 n_2 \cos(\theta_0 - 2\nu) - 4B_l n_2 \sin(\nu) \right. \\
&\quad - \frac{n_2 F_{th\tau}}{m \Omega_0 A} \cos(\Omega_0(\tau + t) + \varphi) \\
&\quad \left. - \frac{4B_l}{A} n_2 n_{1\tau} \sin(\theta_m) + \frac{4B_l}{A} n_2 n_{2\tau} \cos(\theta_m) \right\rangle d\tau \\
&= \frac{4B_l}{A} \int_{-\alpha}^0 d\tau \langle n_2 n_{2\tau} \rangle \cos \theta_m
\end{aligned} \tag{B.52}$$

Then, the average of  $h_5^{(2)}$  is

$$\begin{aligned}
\langle h_5^{(2)} \rangle &= -\frac{4B_l}{A} \int_{-\infty}^0 d\tau \langle n_2 n_{2\tau} \rangle \sin(\Omega_0 t + \theta_{m\alpha}) \cos \theta_m \\
&= -\frac{4B_l}{2A} S_{\text{imp}} \sin(2\theta_m)
\end{aligned} \tag{B.53}$$

The sum is then

$$\langle h_5^{(1)} \rangle + \langle h_5^{(2)} \rangle = 0. \tag{B.54}$$

This means that  $h_5$  is a zero-mean process.

The average value of the noise going to zero means that there is no constant phase error from measurement imprecision. This is by definition a PLL that tracks a fixed oscillation frequency that does not drift. We already noted that the PLL is in a locked state (or  $\nu = 0$ ). This is also consistent with Viterbi.

#### B.0.5.4 Correlation Function of the Measurement Noise

The correlation function of the zero-mean process is just the inverse Fourier transform of the spectral density, or

$$\langle h'_5 h'_{5\tau} \rangle = \frac{1}{2} \left( \frac{4B_l}{A} \right)^2 S_{\text{imp}} \tag{B.55}$$

### B.0.5.5 The Coupled Langevin Equations

Let's collect all the terms that we derived, namely

$$\langle h_2 \rangle = \frac{1}{A} \frac{\gamma k_B T_0}{2m\Omega_0^2} \quad (\text{B.56})$$

$$\langle h'_2 h'_{2\tau} \rangle = \frac{\gamma k_B T_0}{m\Omega_0^2} \delta(\tau) \quad (\text{B.57})$$

$$\langle h'_4 h'_{4\tau} \rangle = \frac{1}{A^2} \frac{\gamma k_B T_0}{m\Omega_0^2} \delta(\tau) \quad (\text{B.58})$$

$$\langle h'_5 h'_{5\tau} \rangle = \frac{1}{A^2} 8B_l^2 S_{\text{imp}} \delta(\tau) \quad (\text{B.59})$$

The coupled amplitude and phase error equations are then

$$\dot{\bar{A}} = - \left( \frac{1}{2} \gamma + \frac{1}{4} \zeta_0 \Omega_0 \cos(2\nu) \right) \bar{A} + \frac{k_B T_0 \gamma}{2m\Omega_0^2} \frac{1}{\bar{A}} + \xi'_F \quad (\text{B.60})$$

$$\dot{\bar{\nu}} = - \left( -\frac{1}{4} \zeta_0 \Omega_0 \sin(2\bar{\nu}) + 4B_l \sin(\bar{\nu}) \right) + \frac{1}{\bar{A}} (\xi_{\text{imp}} + \xi''_F) \quad (\text{B.61})$$

where we use a bar to indicate that the variable is cycle-averaged. Here,  $\xi'_F$  and  $\xi''_F$  are the thermal noise terms with correlation functions  $\langle h'_2 h'_{2\tau} \rangle$  and  $\langle h'_4 h'_{4\tau} \rangle$ , respectively, and  $\xi_{\text{imp}}$  is the measurement imprecision noise with correlation function  $\langle h'_5 h'_{5\tau} \rangle$ .

# C

---

## Calculation of the Kramers-Moyal Coefficients

We derive the terms in the Fokker-Planck equation, known as the Kramers-Moyal coefficients, for the probability density function of the amplitude and phase as it evolves over time, or  $P(A, \nu, t)$ .

The Langevin equation is in its most general form written as

$$\frac{dy_i}{dt} = A_i(\mathbf{y}, t) + \sum_k B_{ik}(\mathbf{y}, t)\xi_k(t) \quad (\text{C.1})$$

where  $\xi_k(t)$  are the  $N_L$  noise terms and their moments are given by  $\langle \xi_k(t) \rangle = 0$  and  $\langle \xi_k(t_1)\xi_l(t_2) \rangle = 2D_{kl}\delta_{kl}\delta(t_1 - t_2)$ . The drift vector is given by

$$a_i^{(1)}(\mathbf{y}, t) = A_i(\mathbf{y}, t) + \sum_{jk} D_{ij}^{jk} B_{jk}(\mathbf{y}, t) \frac{\partial B_{ik}(\mathbf{y}, t)}{\partial y_j} \quad (\text{C.2})$$

and the diffusion tensor is given by

$$a_{ij}^{(2)}(\mathbf{y}, t) = 2 \sum_k D_{ij}^{jk} B_{ik}(\mathbf{y}, t) B_{jk}(\mathbf{y}, t) \quad (\text{C.3})$$

The probability distribution function obeys

$$\begin{aligned} \frac{\partial P}{\partial t} = & - \sum_i \frac{\partial}{\partial y_i} \left\{ \left[ A_i(\mathbf{y}, t) + \sum_{jk} D_{ij}^{jk} B_{jk}(\mathbf{y}, t) \frac{\partial B_{ik}(\mathbf{y}, t)}{\partial y_j} \right] P \right\} \quad (\text{C.4}) \\ & + \sum_{ij} D_{ij}^{jk} \frac{\partial}{\partial y_i \partial y_j} \left\{ \left[ \sum_k B_{ik}(\mathbf{y}, t) B_{jk}(\mathbf{y}, t) \right] P \right\} \end{aligned}$$

# D

---

## Laser Intensity Stabilization Detector

Laser intensity fluctuations in Ch. 5 were tracked with a homebuilt detector using a C30642 photodiode from Excelitas, a transimpedance amplifier based on an OPA847 operational amplifier, and a current source based on a bipolar junction transistor and a high power resistor, as shown in Fig. D.1. The designs are based off of a high power photodetector developed in conjunction with F. Tebbenjohanns \*.

The output of the transimpedance amplifier was measured from a DC-coupled output port (top section of Fig. D.2). The TIA output was also fed into a PI controller (bottom section of Fig. D.2) and used to drive a high-voltage amplifier for a ConOptics Electro-Optic Modulator.

---

\*F. Tebbenjohanns, *Semester Project: Shot noise limited high power photodetector* (2016)

# D Laser Intensity Stabilization Detector

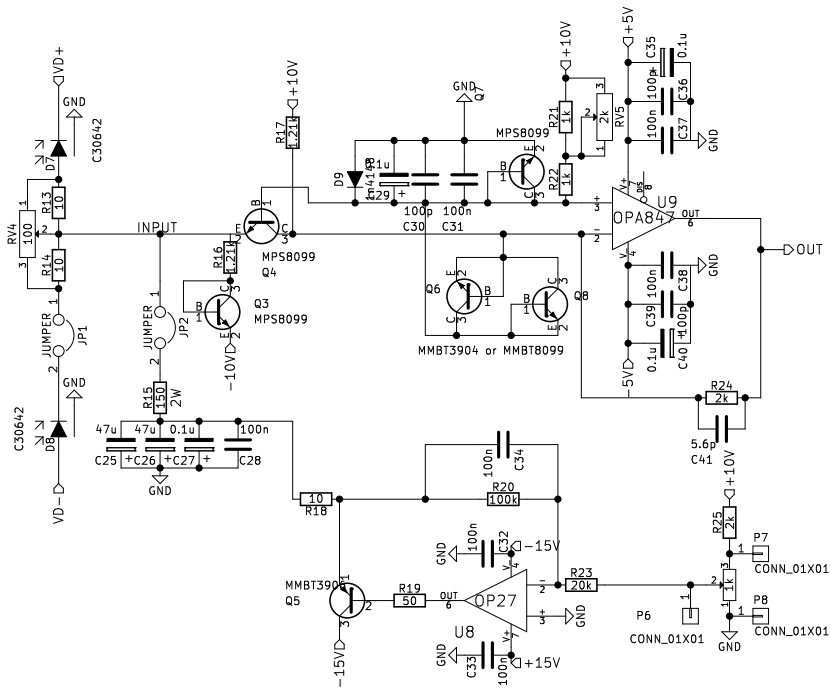


**Figure D.1: Laser Intensity Detector**

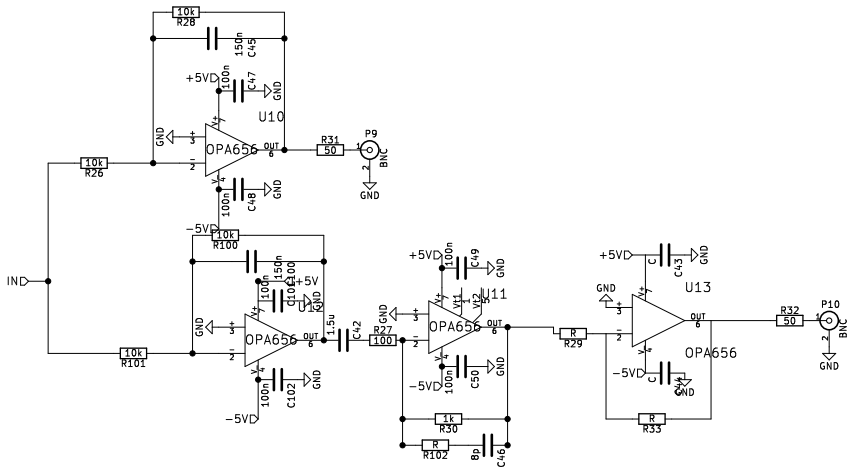


**Figure D.2: Laser Fluctuations Measurement; PI Control**



---

## References

- [1] D. J. E. A. Yevick and D. G. Grier, *Photokinetic analysis of the forces and torques exerted by optical tweezers carrying angular momentum*, Phil. Trans. R. Soc. Lond. A **374**, 20150432 (2017).
- [2] L. Grossman, *The Quantum Quest for a Revolutionary Computer*, Time (2014).
- [3] C. L. Degen, F. Reinhard, and P. Cappellaro, *Quantum Sensing*, Rev. of Mod. Phys. (2017).
- [4] *Technology Quarterly: Quantum Devices*, The Economist , 3 (2017).
- [5] K. L. Ekinici and M. L. Roukes, *Review Article: Nanoelectromechanical systems*, Rev. Sci. Instr. **76**, 061101 (2005).
- [6] M. Aspelmeyer, P. Meystre, and K. Schwab, *Quantum optomechanics*, Physics Today **65**, 29 (2012).
- [7] A. L. Schawlow and C. H. Townes, *Infrared and Optical Masers*, Phys. Rev. **112**, 1940 (1958).
- [8] T. H. Maiman, *Stimulated optical radiation in Ruby*, Nature **187**, 493 (1960).
- [9] A. Abramovici, W. E. Althouse, R. W. P. Drever, Y. Gürsel, S. Kawamura, F. J. Raab, D. Shoemaker, L. Sievers, R. E. Spero, K. S. Thorne, R. E. Vogt, R. Weiss, S. E. Whitcomb, and M. E. Zucker, *LIGO: The Laser Interferometer Gravitational-Wave Observatory*, Science **256**, 325 (1992).
- [10] G. M. Harry and the LIGO Scientific Collaboration, *Advanced LIGO: the next generation of gravitational wave detectors*, Class. Quantum Grav. **27**, 084006 (2010).
- [11] V. B. Braginsky and F. Y. Khalili, *Quantum Measurement*, Cambridge University Press, New York, NY, USA, 1992.
- [12] R. Shankar, *Principles of Quantum Mechanics*, Plenum Press, New York, second edition, 1994.

## REFERENCES

---

- [13] P. Meystre, *A short walk through quantum optomechanics*, Ann. der Physik (2012).
- [14] *Sensitivity of LIGO and Virgo Gravitational Wave Detectors to Compact Binary Inspirals*.
- [15] C. M. Caves, *Quantum-mechanical noise in an interferometer*, Phys. Rev. D **23**, 1693 (1981).
- [16] T. P. Purdy, R. W. Peterson, and C. A. Regal, *Observation of Radiation Pressure Shot Noise on a Macroscopic Object*, Science **339**, 801 (2013).
- [17] D. K. Armani, T. J. Kippenberg, S. M. Spillane, and K. J. Vahala, *Ultra-high-Q toroid microcavity on a chip*, Nature **421**, 925 (2003).
- [18] M. Eichenfeld, J. Chan, R. M. Camacho, K. J. Vahala, and O. Painter, *Optomechanical crystals*, Nature **462**, 78 (2009).
- [19] T. P. Purdy, R. W. Peterson, P.-L. Yu, and C. A. Regal, *Cavity optomechanics with Si<sub>3</sub>N<sub>4</sub> membranes at cryogenic temperatures*, New J. Phys. **14**, 115021 (2012).
- [20] M. J. Burek, J. D. Cohen, S. M. Meenehan, N. El-Sawah, C. Chia, T. Ruelle, S. Meesala, J. Rochman, H. A. Atikian, M. Markham, D. J. Twitchen, M. D. Lukin, O. Painter, and M. Lončar, *Diamond optomechanical crystals*, Optica **3**, 1404 (2016).
- [21] M. Aspelmeyer, T. J. Kippenberg, and F. Marquardt, *Cavity optomechanics*, Rev. of Mod. Phys. **86**, 1391 (2014).
- [22] T. Aoki, B. Dayan, E. Wilcut, W. P. Bowen, A. S. Parkins, T. J. Kippenberg, K. J. Vahala, and H. J. Kimble, *Observation of strong coupling between one atom and a monolithic microresonator*, Nature **443**, 671 (2006).
- [23] J. D. Teufel, T. Donner, D. Li, J. W. Harlow, M. S. Allman, K. Cicak, A. J. Sirois, J. D. Whittaker, K. W. Lehnert, and R. W. Simmonds, *Sideband cooling of micromechanical motion to the quantum ground state*, Nature **475**, 359 (2011).
- [24] J. Chan, T. P. M. Alegre, A. H. Safavi-Naeini, J. T. Hill, A. Krause, S. Gröblacher, M. Aspelmeyer, and O. Painter, *Laser cooling of a nanomechanical oscillator into its quantum ground state*, Nature **478**, 89 (2011).
- [25] E. Verhagen, S. Deléglise, S. Weis, A. Schliesser, and T. J. Kippenberg, *Quantum-coherent coupling of a mechanical oscillator to an optical cavity mode*, Nature **482**, 63 (2012).
- [26] D. Leibfried, R. Blatt, C. Monroe, and D. Wineland, *Quantum dynamics of single trapped ions*, Rev. of Mod. Phys. **75**, 281 (2003).
- [27] V. Sudhir, D. J. Wilson, R. Schilling, H. Schütz, S. A. Fedorov, A. H. Ghadimi, A. Nunnenkamp, and T. J. Kippenberg, *Appearance and Disappearance*

- of Quantum Correlations in Measurement-Based Feedback Control of a Mechanical Oscillator*, Phys. Rev. X **7**, 011001 (2017).
- [28] R. Riedinger, S. Hong, R. A. Norte, J. A. Slater, J. Shang, A. G. Krause, V. Anant, M. Aspelmeyer, and S. Gröblacher, *Non-classical correlations between single photons and phonons from a mechanical oscillator*, Nature **530**, 313 (2016).
- [29] J. T. Hill, A. H. Safavi-Naeini, J. Chan, and O. Painter, *Coherent optical wavelength conversion via cavity optomechanics*, Nature Commun. **3**, 1196 (2012).
- [30] A. H. Safavi-Naeini, S. Groblacher, J. T. Hill, J. Chan, M. Aspelmeyer, and O. Painter, *Squeezed light from a silicon micromechanical resonator*, Nature **500**, 185 (2013).
- [31] R. Kubo, *The fluctuation-dissipation theorem*, Rep. Prog. Phys. **29**, 255 (1966).
- [32] F. Marquardt and A. Püttmann, *Introduction to dissipation and decoherence in quantum systems*, arXiv: 0809.4403v1 , 1 (2008).
- [33] J. Atalaya, A. Isaacsson, and M. I. Dykman, *Diffusion-induced dephasing in nanomechanical resonators*, Phys. Rev. B **83**, 045419 (2011).
- [34] A. Ashkin, *Optical trapping and manipulation of neutral particles using lasers*, Proc. Natl. Acad. Sci. USA **94**, 4853 (1997).
- [35] Z.-Q. Yin, A. A. Geraci, and T. Li, *Optomechanics of levitated dielectric nanoparticles*, Int. J. Mod. Phys. B **27**, 1330018 (2013).
- [36] A. Ashkin, *Acceleration and trapping of particles by radiation pressure*, Phys. Rev. Lett. **24**, 156 (1970).
- [37] A. Ashkin, *Optical trapping and manipulation of neutral particles using lasers: a reprint volume with commentaries*, World Scientific, Hackensack, N.J.
- [38] T. W. Hänsch and A. L. Schawlow, *Cooling of gases by laser radiation*, Optics Comm. **13**, 68 (1975).
- [39] D. J. Wineland and W. M. Itano, *Laser cooling of atoms*, Phys. Rev. A **20**, 1521 (1979).
- [40] D. E. Chang, C. A. Regal, S. B. Papp, D. J. Wilson, J. Ye, O. Painter, H. J. Kimble, and P. Zoller, *Cavity opto-mechanics using an optically levitated nanosphere*, Proceedings of the National Academy of Sciences **107**, 1005 (2010).
- [41] O. Romero-Isart, M. L. Juan, R. Quidant, and J. I. Cirac, *Toward quantum superposition of living organisms*, New Journal Of Physics **12**, 033015 (2010).
- [42] A. Ashkin, J. M. Dziedzic, J. E. Bjorkholm, and S. Chu, *Observation of a single-beam gradient force optical trap for dielectric particles*, Opt. Lett. **11**, 288 (1986).
- [43] A. Ashkin and J. M. Dziedzic, *Optical Levitation in High-Vacuum*, Appl. Phys. Lett. **28**, 333 (1976).

## REFERENCES

---

- [44] A. Ashkin and J. M. Dziedzic, *Optical trapping and manipulation of viruses and bacteria*, Science **235**, 1517 (1987).
- [45] S. Chu, *Laser Manipulation of Atoms and Particles*, Science **253**, 861 (1991).
- [46] M. H. Anderson, J. R. Ensher, M. R. Matthews, C. E. Wieman, and E. A. Cornell, *Observation of Bose-Einstein Condensation in a Dilute Atomic Vapor*, Science **269**, 198 (1995).
- [47] S. M. Block, L. S. B. Goldstein, and B. J. Schnapp, *Bead movement by single kinesin molecules studied with optical tweezers*, Nature **348**, 348 (1990).
- [48] O. M. Marago, P. H. Jones, P. G. Gucciardi, G. Volpe, and A. C. Ferrari, *Optical trapping and manipulation of nanostructures*, Nature Nanotechnology **8**, 807 (2013).
- [49] H. C. van de Hulst, *Light Scattering by Small Particles*, Dover Publications, Inc., Mineola, NY, 1981.
- [50] J. D. Jackson, *Classical Electrodynamics*, Wiley, New York, third edition, 1999.
- [51] L. Novotny and B. Hecht, *Principles of Nano-Optics*, Cambridge University Press, Cambridge, second edition, 2012.
- [52] B. T. Draine, *The discrete-dipole approximation and its application to interstellar graphite grains*, Astrophys. J. **333**, 848 (1988).
- [53] M. Born and E. Wolf, *Principles of Optics*, Pergamon, Oxford, seventh edition, 1999.
- [54] S. Chandrasekhar, *Stochastic problems in physics and astronomy*, Rev. Mod. Phys. **15**, 1 (1943).
- [55] H. Tanji-Suzuki, I. D. Leroux, M. H. Schleier-Smith, M. Cetina, A. T. Grier, J. Simon, and V. Vuletić, *Chapter 4 - Interaction between Atomic Ensembles and Optical Resonators: Classical Description*, in *Advances in Atomic, Molecular, and Optical Physics*, edited by P. B. E. Arimondo and C. Lin, volume 60 of *Advances In Atomic, Molecular, and Optical Physics*, pages 201 – 237, Academic Press, 2011.
- [56] F. Gittes and C. F. Schmidt, *Interference model for back-focal-plane displacement detection in optical tweezers*, Opt. Lett. **23**, 7 (1998).
- [57] H. P. Yuen and V. W. S. Chan, *Noise in homodyne and heterodyne detection*, Opt. Lett. **8**, 177 (1983).
- [58] H.-A. Bachor and T. C. Ralph, *A guide to experiments in quantum optics*, Wiley-VCH, 2 edition, 2009.
- [59] P. Asenbaum, *Cavity cooling of silica nanoparticles in high-vacuum*, PhD thesis, 2014.
- [60] L. G. Villanueva, R. B. Karabalin, M. H. Matheny, E. Kenig, M. C. Cross, and M. L. Roukes, *A nanoscale parametric feedback oscillator*, Nano Lett. **11**, 5054

- (2011).
- [61] J. Gieseler, B. Deutsch, R. Quidant, and L. Novotny, *Subkelvin Parametric Feedback Cooling of a Laser-Trapped Nanoparticle*, Phys. Rev. Lett. **109**, 103603 (2012).
- [62] F. M. Gardner, *Phaselock techniques*, John Wiley, 2005.
- [63] A. Hajimiri and T. H. Lee, *The design of low noise oscillators*, Kluwer Academic, 2003.
- [64] A. Patapoutian, *On phase-locked loops and Kalman filters*, IEEE Transactions on Communications **47**, 670?672 (1999).
- [65] A. J. Viterbi, *Phase-locked loop dynamics in the presence of noise by Fokker-Planck techniques*, Proceedings of the IEEE **51**, 1737?1753 (1963).
- [66] M. Gitterman, *The noisy pendulum*, World scientific, 2008.
- [67] J. F. O'Hanlon, *A User's Guide to Vacuum Technology*, Wiley, 3 edition, 2003.
- [68] M. Li and H. F. Dylla, *Model for the outgassing of water from metal surfaces*, J. Vac. Sci. Technol. A **11**, 1702 (1993).
- [69] S. R. Koebley and R. A. Outlaw, *Degassing a vacuum system with in-situ UV radiation*, J. Vac. Sci. Technol. A **30**, 060601 (2012).
- [70] P. Mestres, J. Berthelot, M. Spasenovic, J. Gieseler, L. Novotny, and R. Quidant, *Cooling and manipulation of a levitated nanoparticle with an optical fiber trap*, Appl. Phys. Lett. **107**, 151102 (2015).
- [71] D. Grass, J. Fesel, S. G. Hofer, N. Kiesel, and M. Aspelmeyer, *Optical trapping and control of nanoparticles inside evacuated hollow core photonic crystal fibers*, Appl. Phys. Lett. **108**, 221103 (2013).
- [72] C. Robens, S. Brakhane, W. Alt, F. Kleissler, D. Meschede, G. Moon, G. Ramola, and A. Alberti, *High numerical aperture ( $NA = 0.92$ ) objective lens for imaging and addressing of cold atoms*, Opt. Lett. **42**, 1043 (2017).
- [73] W. Wiczorek, S. G. Hofer, J. Hoelscher-Obermaier, R. Riedinger, K. Hammerer, and M. Aspelmeyer, *Optimal State Estimation for Cavity Optomechanical Systems*, Phys. Rev. Lett. **114**, 223601 (2015).
- [74] A. D. O'Connell, M. Hofheinz, M. Ansmann, R. C. Bialczak, M. Lenander, E. Lucero, M. Neeley, D. Sank, H. Wang, M. Weides, J. Wenner, J. M. Martinis, and A. N. Cleland, *Quantum ground state and single-phonon control of a mechanical resonator*, Nature **464**, 697 (2010).
- [75] D. Vitali, S. Mancini, L. Ribichini, and P. Tombesi, *Macroscopic mechanical oscillators at the quantum limit through optomechanical cooling*, J. Opt. Soc. Am. B **20**, 1054 (2003).
- [76] J.-M. Courty, A. Heidmann, and M. Pinar, *Quantum limits of cold damping with optomechanical coupling*, The European Physical Journal D - Atomic,

## REFERENCES

---

- Molecular, Optical and Plasma Physics **17**, 399 (2001).
- [77] C. Genes, D. Vitali, P. Tombesi, S. Gigan, and M. Aspelmeyer, *Ground-state cooling of a micromechanical oscillator: Comparing cold damping and cavity-assisted cooling schemes*, Physical Review A **77**, 033804 (2008).
- [78] C. H. Metzger and K. Karrai, *Cavity cooling of a microlever*, Nature **432**, 1002 (2004).
- [79] N. Kiesel, F. Blaser, U. Delic, D. Grass, R. Kaltenbaek, and M. Aspelmeyer, *Cavity cooling of an optically levitated submicron particle*, Proceedings of the National Academy of Sciences **110**, 14180 (2013).
- [80] P. F. Cohadon, A. Heidmann, and M. Pinard, *Cooling of a mirror by radiation pressure*, Phys. Rev. Lett. **83**, 3174 (1999).
- [81] O. Arcizet, P.-F. Cohadon, T. Briant, M. Pinard, A. Heidmann, J.-M. Mackowski, C. Michel, L. Pinard, O. Français, and L. Rousseau, *High-Sensitivity Optical Monitoring of a Micromechanical Resonator with a Quantum-Limited Optomechanical Sensor*, Phys. Rev. Lett. **97**, 133601 (2006).
- [82] D. Kleckner and D. Bouwmeester, *Sub-kelvin optical cooling of a micromechanical resonator*, Nature **444**, 75 (2006).
- [83] M. Poggio, C. L. Degen, H. J. Mamin, and D. Rugar, *Feedback cooling of a cantilever's fundamental mode below 5 mK*, Physical Review Letters **99**, 017201 (2007).
- [84] S. Mancini, D. Vitali, and P. Tombesi, *Optomechanical cooling of a macroscopic oscillator by homodyne feedback*, Physical Review Letters **80**, 688 (1998).
- [85] J. Milatz and J. V. Zolingen, *The brownian motion of electrometers*, Physica **19**, 181 (1953).
- [86] D. J. Wilson, V. Sudhir, N. Piro, R. Schilling, A. Ghadimi, and T. J. Kippenberg, *Measurement-based control of a mechanical oscillator at its thermal decoherence rate*, Nature **524**, 325 (2015).
- [87] D. Vitali, S. Mancini, L. Ribichini, and P. Tombesi, *Mirror quiescence and high-sensitivity position measurements with feedback*, Phys. Rev. A **65**, 063803 (2002).
- [88] T. Li, S. Kheifets, and M. G. Raizen, *Millikelvin cooling of an optically trapped microsphere in vacuum*, Nature Physics **7**, 527 (2011).
- [89] J. Millen, P. Z. G. Fonseca, T. Mavrogordatos, T. S. Monteiro, and P. F. Barker, *Cavity Cooling a Single Charged Levitated Nanosphere*, Phys. Rev. Lett. **114**, 123602 (2015).
- [90] M. Frimmer, J. Gieseler, and L. Novotny, *Cooling Mechanical Oscillators by Coherent Control*, Phys. Rev. Lett. **117**, 163601 (2016).
- [91] J. Gieseler, R. Quidant, C. Dellago, and L. Novotny, *Dynamic relaxation*

- of a levitated nanoparticle from a non-equilibrium steady state*, Nature Nanotechnology **9**, 358 (2014).
- [92] R. L. Stratonovich, *Topics in the theory of random noise*, Gordon and Breach, 1967.
- [93] H. Risken, *The Fokker-Planck Equation. Methods of Solution and Applications*, Springer-Verlag, 1984.
- [94] G. A. Beresnev, S. A. Chernyak, and V. G. Fomyagin, *Motion of a spherical particle in a rarefied gas. Part 2. Drag and thermal polarization*, J. Fluid Mech. **219**, 405 (1990).
- [95] V. Jain, J. Gieseler, C. Moritz, C. Dellago, R. Quidant, and L. Novotny, *Direct Measurement of Photon Recoil from a Levitated Nanoparticle*, Phys. Rev. Lett. **116**, 243601 (2016).
- [96] V. Braginsky and S. Vyatchanin, *Gravitational waves and the limiting stability of self-excited oscillators*, Sov. Phys. JETP **47**, 433 (1978).
- [97] S. Schreppler, N. Spethmann, N. Brahms, T. Botter, M. Barrios, and D. M. Stamper-Kurn, *Optically measuring force near the standard quantum limit*, Science **344**, 1486 (2014).
- [98] J. D. Teufel, F. Lecocq, and R. W. Simmonds, *Overwhelming Thermomechanical Motion with Microwave Radiation Pressure Shot Noise*, Phys. Rev. Lett. **116**, 013602 (2016).
- [99] R. W. Peterson, T. P. Purdy, N. S. Kampel, R. W. Andrews, P.-L. Yu, K. W. Lehnert, and C. A. Regal, *Laser Cooling of a Micromechanical Membrane to the Quantum Backaction Limit*, Phys. Rev. Lett. **116**, 063601 (2016).
- [100] G. Ranjit, D. P. Atherton, J. H. Stutz, M. Cunningham, and A. A. Geraci, *Attonewton force detection using microspheres in a dual-beam optical trap in high vacuum*, Phys. Rev. A **91**, 051805 (2015).
- [101] J. Gieseler, L. Novotny, and R. Quidant, *Thermal nonlinearities in a nanomechanical oscillator*, Nature Physics **9**, 806 (2013).
- [102] O. Romero-Isart, A. C. Pflanzer, M. L. Juan, R. Quidant, N. Kiesel, M. Aspelmeyer, and J. I. Cirac, *Optically levitating dielectrics in the quantum regime: Theory and protocols*, Physical Review A **83**, 013803 (2011).
- [103] R. Kaltenbaek, G. Hechenblaikner, N. Kiesel, O. Romero-Isart, K. Schwab, U. Johann, and M. Aspelmeyer, *Macroscopic quantum resonators (MAQRO)*, Exp. Astron. **34**, 123 (2012).
- [104] A. Arvanitaki and A. A. Geraci, *Detecting High-Frequency Gravitational Waves with Optically Levitated Sensors*, Phys. Rev. Lett. **110**, 071105 (2013).
- [105] A. Aspect, E. Arimondo, R. Kaiser, N. Vansteenkiste, and C. Cohen-Tannoudji, *Laser Cooling below the One-Photon Recoil Energy by Velocity-Selective*

## REFERENCES

---

- Coherent Population Trapping*, Phys. Rev. Lett. **61**, 826 (1988).
- [106] M. Kasevich and S. Chu, *Laser Cooling below a Photon Recoil with Three-Level Atoms*, Phys. Rev. Lett. **69**, 1741 (1992).
- [107] W. M. Itano and D. J. Wineland, *Laser cooling of ions stored in harmonic and Penning traps*, Physical Review A **25**, 35 (1982).
- [108] B. Rodenburg, L. P. Neukirch, A. N. Vamivakas, and M. Bhattacharya, *Quantum model of cooling and force sensing with an optically trapped nanoparticle*, Optica **3**, 318 (2016).
- [109] K. Karrai, I. Favero, and C. Metzger, *Doppler Optomechanics of a Photonic Crystal*, Phys. Rev. Lett. **100**, 240801 (2008).
- [110] E. A. Power and T. Thirunamachandran, *Electromagnetic fields of a moving electric dipole*, Proceedings of the Royal Society of London A: Mathematical, Physical and Engineering Sciences **457**, 2757 (2001).
- [111] M. E. Gehm, K. M. O'Hara, T. A. Savard, and J. E. Thomas, *Dynamics of noise-induced heating in atom traps*, Physical Review A **58**, 3914 (1998).
- [112] T. A. Savard, K. M. O'Hara, and J. E. Thomas, *Laser-noise-induced heating in far-off resonance optical traps*, Phys. Rev. A **56**, R1095 (1997).
- [113] W. P. B. M. A. Taylor, J. Knittel, *Fundamental constraints on particle tracking with optical tweezers*, New J. Phys. **15**, 023018 (2013).
- [114] R. Brown, *A brief account of microscopical observations made in the months of June, July and August, 1827, on the particles contained in the pollen of plants; and on the general existence of active molecules in organic and inorganic bodies*, Phil. Mag. **4**, 161 (1828).
- [115] S. Chu, *Laser trapping of neutral particles*, Scientific American **2**, 71 (1992).
- [116] J. I. Cirac, R. Blatt, P. Zoller, and W. D. Phillips, *Laser cooling of trapped ions in a standing wave*, Phys. Rev. A **46**, 2668 (1992).
- [117] C. N. Cohen-Tannoudji and W. D. Phillips, *New mechanisms for laser cooling*, Physics Today **10**, 33 (1990).
- [118] A. Schenzle and H. Brand, *Multiplicative stochastic processes in statistical physics*, Phys. Rev. A **20**, 1628 (1979).
- [119] C. J. Tessone and H. S. Wio, *Stochastic resonance in bistable systems: the effect of simultaneous additive and multiplicative correlated noises*, Mod. Phys. Lett. B **12**, 1195 (1998).
- [120] S. E. Mangioni, R. R. Deza, R. Toral, and H. S. Wio, *Nonequilibrium phase transitions induced by multiplicative noise: Effects of self-correlation*, Phys. Rev. E **61**, 223 (2000).
- [121] R. C. Bourret, U. Frisch, and A. Pouquet, *Brownian motion of harmonic oscillator with stochastic frequency*, Physica **65**, 201 (1973).



- 
- [122] M. Sansa, E. Sage, E. C. Bullard, M. Gély, T. Alava, E. Colinet, A. K. Naik, L. G. Villanueva, L. Duraffourg, M. L. Roukes, G. Jourdan, and S. Hentz, *Frequency fluctuations in silicon nanoresonators*, Nat Nano **11**, 552 (2016).
- [123] A. A. Geraci, S. B. Papp, and J. Kitching, *Short-range force detection using optically cooled levitated microspheres*, Phys. Rev. Lett. **105**, 101101 (2010).
- [124] A. M. Jayich, J. C. Sankey, K. Borkje, D. Lee, C. Yang, M. Underwood, L. Childress, A. Petrenko, S. M. Girvin, and J. G. E. Harris, *Cryogenic optomechanics with a Si<sub>3</sub>N<sub>4</sub> membrane and classical laser noise*, New J. Phys. **14**, 115018 (2012).
- [125] A. H. Safavi-Naeini, J. Chan, J. T. Hill, S. Groblacher, H. Miao, Y. Chen, M. Aspelmeyer, and O. Painter, *Laser noise in cavity-optomechanical cooling and thermometry*, New J. Phys. **15**, 035007 (2013).
- [126] N. G. van Kampen, *Stochastic differential equations*, Physics Reports **24**, 171 (1976).
- [127] J. Gieseler, L. Novotny, C. Moritz, and C. Dellago, *Non-equilibrium steady state of a driven levitated particle with feedback cooling*, New J. Phys. **17**, 045011 (2015).
- [128] C. Anteneodo and C. Tsallis, *Multiplicative noise: A mechanism leading to nonextensive statistical mechanics*, J. Math. Phys. **44**, 5194 (2003).
- [129] J. Rollins, D. Ottaway, M. Zucker, R. Weiss, and R. Abbott, *Solid-state laser intensity stabilization at the  $10^{-8}$  level*, Opt. Lett. **29**, 1876 (2004).
- [130] P. Kwee, B. Willke, and K. Danzmann, *New concepts and results in laser power stabilization*, Applied Physics B-Lasers and Optics **102**, 515 (2011).
- [131] E. Gavartin, P. Verlot, and T. J. Kippenberg, *Stabilization of a linear nanomechanical oscillator to its thermodynamic limit*, Nature Commun. **4**, 2860 (2013).
- [132] A. Labuda, J. R. Bates, and P. H. Gruetter, *The noise of coated cantilevers*, Nanotechnology **23**, 025503 (2011).
- [133] R. Bourret, *Energetic stability of the harmonic oscillator with random parametric driving*, Physica **54**, 623 (1971).
- [134] R. Loudon, *The Quantum Theory of Light*, Oxford Science Publications, Clarendon Press, Oxford, second edition, 1983.
- [135] J. Moser, J. Guttinger, A. Eichler, M. J. Esplandiu, D. E. Liu, M. I. Dykman, and A. Bachtold, *Ultrasensitive force detection with a nanotube mechanical resonator*, Nature Nanotechnology **8**, 493 (2013).
- [136] H. M. Wiseman and G. J. Milburn, *Quantum theory of optical feedback via homodyne detection*, Phys. Rev. Lett. **70**, 548 (1993).
- [137] A. C. Doherty, S. Habib, K. Jacobs, H. Mabuchi, and S. M. Tan, *Quantum*

## REFERENCES

---

- feedback control and classical control theory*, Phys. Rev. A **62**, 012105 (2000).
- [138] M. Hatridge, S. Shankar, M. Mirrahimi, F. Schackert, K. Geerlings, T. Brecht, K. M. Sliwa, B. Abdo, L. Frunzio, S. M. Girvin, R. J. Schoelkopf, and M. H. Devoret, *Quantum Back-Action of an Individual Variable-Strength Measurement*, Science **339**, 178 (2013).
- [139] MillenJ., DeesuwatT., BarkerP., and AndersJ., *Nanoscale temperature measurements using non-equilibrium Brownian dynamics of a levitated nanosphere*, Nat Nano **9**, 425 (2014).
- [140] K. Berg-Sørensen and H. Flyvbjerg, *Power spectrum analysis for optical tweezers*, Rev. Sci. Instr. **75**, 594 (2004).
- [141] R. C. Tolman, *Statistical mechanics with applications to physics and chemistry*, Chemical Catalog Co., 1927.
- [142] A. Clerk, M. Devoret, S. Girvin, F. Marquardt, and R. Schoelkopf, *Introduction to quantum noise, measurement, and amplification*, Reviews Of Modern Physics **82**, 1155 (2010).
- [143] M. Underwood, D. Mason, D. Lee, H. Xu, L. Jiang, A. B. Shkarin, K. Borkje, S. M. Girvin, and J. G. E. Harris, *Measurement of the motional sidebands of a nanogram-scale oscillator in the quantum regime*, Phys. Rev. A **92**, 061801(R) (2015).
- [144] T. P. Purdy, P.-L. Yu, R. W. Peterson, N. S. Kampel, and C. A. Regal, *Strong Optomechanical Squeezing of Light*, Phys. Rev. X **3**, 031012 (2013).
- [145] J. H. Shapiro, *Quantum Noise and Excess Noise in Optical Homodyne and Heterodyne Receivers*, IEEE J. Quantum Elec. **QE-21**, 237 (1985).
- [146] N. Ocelic, A. Huber, and R. Hillenbrand, *Pseudoheterodyne detection for background-free near-field spectroscopy*, Appl. Phys. Lett. **89**, 101124 (2006).
- [147] J. W. Tay, M. T. L. Hsu, and W. P. Bowen, *Quantum limited particle sensing in optical tweezers*, Phys. Rev. A **80**, 063806 (2009).
- [148] M. T. L. Hsu, V. Delaubert, P. K. Lam, and W. P. Bowen, *Optimal optical measurement of small displacements*, J. Opt. B **6**, 495 (2004).
- [149] W. Schottky, *Über spontane Stromschwankungen in verschiedenen Elektrizitätsleitern*, Annalen der Physik **362**, 541 (1918).

---

## List of Publications

### **This thesis is based in part on the following publications:**

M. Frimmer, K. Luszcz, S. Ferrero, **V. Jain**, E. Hebestreit, and L. Novotny, *Controlling the net charge on a nanoparticle optically levitated in vacuum*, Physical Review A **00**, 001800(R) (2017).

**V. Jain**, F. Tebbenjohanns, and L. Novotny, *Microkelvin Control of an Optically Levitated Nanoparticle*, Optical Society of America - Frontiers in Optics **FF5B.2** (2016).

**V. Jain**, J. Gieseler, C. Moritz, C. Dellago, R. Quidant, and L. Novotny, *Direct Measurement of Photon Recoil from a Levitated Nanoparticle*, Physical Review Letters **116**, 243601 (2016).

### **Other publications by the author:**

Z. Walsh, P.A. Levkin, **V. Jain**, and F. Svec, *Visible light initiated polymerization of styrenic monolithic stationary phases using 470nm light emitting diode arrays*, Journal of Separation Science **33**, 61 (2010).

Y. Wang, Z. Zhuang, **V. Jain**, others and M.H. Rafailovich, *Potentiometric*

## REFERENCES

---

*sensors based on surface molecular imprinting: detection of cancer biomarkers and viruses*, *Sensors & Actuators B* **146**, 381 (2010).

---

## Curriculum Vitae

Vijay Jain was born in Manhasset, New York in the United States of America in 1989. He graduated from Herricks High School in 2007 and then studied at Harvard University in Cambridge, Massachusetts. There, his research focused on the physical chemistry of magnetically sensitive fluorescent molecules and, separately, on the onset of color in disordered colloidal materials, and he obtained his A.B. in Chemistry & Physics in 2011. In the Fall of 2011 he began the Physics and Astronomy Ph.D. program at the University of Rochester, where he received a National Science Foundation Graduate Research Fellowship. After receiving his M.A. in Physics, he moved to the Swiss Federal Institute of Technology (ETH) Zürich in the summer of 2012. His research is in the area of levitated optomechanics, under the supervision of Lukas Novotny.